Report No. CDOT-DTD-R-2004-2
Final Report

EVALUATION OF GFRP DECK PANEL FOR THE O'FALLON PARK BRIDGE

Guido Camata
P. Benson Shing

July 2004

COLORADO DEPARTMENT OF TRANSPORTATION
RESEARCH BRANCH

The contents of this report reflect the views of the authors, who are responsible for the facts and accuracy of the data presented herein. The contents do not necessarily reflect the official views of the Colorado Department of Transportation or the Federal Highway Administration. This report does not constitute a standard, specification, or regulation.

Technical Report Documentation Page

1. Report No.	2. Government Accession No.	3. Recipient's Catalog No.
CDOT-DTD-R-2004-2		

4. Title and Subtitle	5. Report Date
EVALUATION OF GFRP DECK PANEL FOR THE O'FALLON PARK BRIDGE	July 2004
	6. Performing Organization Code

7. Author(s)	8. Performing Organization Report No.
Guido Camata and P. Benson Shing	CDOT-DTD-R-2004-2

9. Performing Organization Name and Address	10. Work Unit No. (TRAIS)
University of Colorado Department of Civil, Environmental & Architectural Engineering Boulder, CO 80309-0428	11. Contract or Grant No. 00HAA 00069

12. Sponsoring Agency Name and Address	13. Type of Report and Period Covered
Colorado Department of Transportation - Research 4201 E. Arkansas Ave. Denver, CO 80222	Final Report
	14. Sponsoring Agency Code File: 81.30

15. Supplementary Notes

Prepared in cooperation with the US Department of Transportation, Federal Highway Administration

16. Abstract

Under the Innovative Bridge Research and Construction (IBRC) program of the Federal Highway Administration (FHWA), the City and County of Denver in cooperation with the Colorado Department of Transportation (CDOT) and FHWA built a bridge with a glass fiber reinforced polymer deck (GFRP) in O'Fallon Park, which is located west of the City of Denver. One of the main objectives of this project was to investigate the feasibility of using FRP decks for highway bridges. Hence, the FRP deck in the O'Fallon Park bridge was designed to have a configuration similar to a highway bridge deck. The GFRP deck has a sandwich construction with top and bottom faces and a honeycomb core. Because of the lack of standard design provisions and manufacturing techniques for GFRP deck C panels, studies have been conducted at the University of Colorado at Boulder to evaluate the design proposed by the manufacturer, and the load-carrying capacity and long-term performance of the selected panels as part of the IBRC program.

This study has shown that the design of the GFRP deck is adequate according to the provisions of the City and County of Denver. The deck has a factor of safety of five against failure. The deck also satisfies the deflection limits stipulated in the design provisions. However, the tests and the analyses have indicated that the material orthotropy of the panel and the localized bending effect caused by the soft core can reduce the effective bending width by 25% compared to a homogenous isotropic panel. Furthermore, this and past studies have shown that the governing failure mode of this type of sandwich panel is the delamination of the upper face from the core and that there is a large scatter of the interface shear strength among the test specimens. Hence, this should be a major consideration in design.

Implementation

This project has demonstrated the feasibility of using GFRP decks for highway bridges. However, several issues require special attention. First, the interface shear between a face and the core should be a major consideration in design. It is recommended that the interface shear be less than 20% of the shear strength under service loads. To increase the level of confidence in design, a good quality control is called for to ensure a consistent interface shear strength. The effective bending width of a GFRP panel can be 25% smaller than that of an isotropic panel. However, this is also dependent on the geometry of a panel and the support conditions. A finite element analysis taking into account the material orthotropy and soft core can be conducted to determine the effective bending width. The anchoring of a panel to the supports requires further investigation.

17. Keywords	18. Distribution Statement
glass fiber reinforced polymers, GFRP panels, honeycomb sandwich panels, bridge decks, ultimate strength, fatigue endurance	No restrictions. This document is available to the public through: National Technical Information Service 5825 Port Royal Road Springfield, VA 22161

19. Security Classif. (of this report)	20. Security Classif. (of this page)	21. No. of Pages	22. Price
None	None	178	

Form DOT F 1700.7 (8-72) Reproduction of completed page authorized

EVALUATION OF GFRP DECK PANEL FOR THE O'FALLON PARK BRIDGE

by

Guido Camata
P. Benson Shing

Department of Civil, Environmental
& Architectural Engineering
University of Colorado
Boulder, CO 80309-0428

Sponsored by the
U.S. Department of Transportation
Federal Highway Administration

July 2004

Report No. CDOT-DTD-R-2004-2
Colorado Department of Transportation
Research Branch
4201 E. Arkansas Ave.
Denver, CO 80222

AKNOWLEDGMENTS

This study was sponsored by the Federal Highway Administration (FHWA) and conducted in conjunction with the Colorado Department of Transportation (CDOT) and the City and County of Denver under FHWA's Innovative Bridge Research and Construction Program. The project was monitored by Matthew Greer of the Colorado Division of FHWA, and administered by Ahmad Ardani of the Research Branch of CDOT.

John Guenther of Parsons, Brinckerhoff, Quade, and Douglas was the structural engineer for the O'Fallon Park bridge, which is the subject of this study. His continuous assistance and coordination of the design, construction, and research work is greatly appreciated. Dr. Jerry Plunkett of Kansas Structural Composites, Inc. (KSCI), which manufactured and installed the fiber reinforced polymer deck in the bridge, was most supportive of the research work. The four beam specimens and the specimens for the crushing tests were contributed by KSCI, for which the writers are very grateful.

The writers appreciate the helpful assistance of Thomas L. Bowen, manager of the Structures and Materials Testing Laboratory of the University of Colorado, and the laboratory assistants, Chris Baksa, Chris Cloutier, Steve Cole, and David Shaw, in the experimental work. The writers would also like to thank Professor Victor Saouma for letting them use the finite element program Merlin.

Finally, the writers would like to thank Joan Pinamont of CDOT for her editorial assistance.

Opinions expressed in this report are those of the writers and do not necessarily represent those of CDOT or FHWA.

EXECUTIVE SUMMARY

A large number of highway bridges are in need of repair, replacement, or significant upgrade because of deterioration induced by environmental conditions, increasing traffic volume, and higher load requirements. For bridge replacement, there are not only the associated material costs to consider, but also the labor costs, delays, and detours. Hence, a cost-effective solution must consider the minimization of traffic disruption as well as future maintenance needs.

Fiber reinforced polymer (FRP) materials offer high stiffness and strength-to-weight ratios, excellent corrosion and fatigue resistance, reduced maintenance costs, simplicity of handling, and faster installation time compared to conventional materials. Under the Innovative Bridge Research and Construction (IBRC) program of the Federal Highway Administration (FHWA), the City and County of Denver in cooperation with the Colorado Department of Transportation (CDOT) and FHWA built a bridge with a glass fiber reinforced polymer deck (GFRP) in O'Fallon Park, which is located west of the City of Denver. One of the main objectives of this project is to investigate the feasibility of using FRP decks for highway bridges. Hence, the FRP deck in the O'Fallon Park bridge was designed to have a configuration similar to a highway bridge deck.

The GFRP deck has a sandwich construction with top and bottom faces and a honeycomb core. They were manufactured in a factory, shipped to the site, and assembled by the supplier, which is Kansas Structural Composites, Inc. The deck is covered by a ½-inch-thick polymer concrete wear surface. Even though the bridge is mainly for pedestrians and occasionally small vehicles, the deck was designed to carry a standard HS 25-44 truck to allow the passage of fire trucks and garbage trucks. Because of the lack of standard design provisions and manufacturing techniques for GFRP deck panels, studies have been conducted at the University of Colorado at Boulder to evaluate the design proposed by the manufacturer, and the load-carrying capacity and long-term performance of the selected panels as part of the IBRC program.

The studies reported here were divided into two phases. Phase I was intended to evaluate and confirm the candidate deck sections proposed by the manufacturer. To this end, four GFRP beams were tested to evaluate their stiffness and load-carrying capacities and compression tests were conducted to evaluate the crushing capacities of the panels. In Phase II, the load-carrying capacity and fatigue endurance of a full-size two-span GFRP panel that had the same design as the actual bridge deck was studied. The aim was to investigate the influence of load cycles on the load-carrying capacity of a panel and on the performance of the anchor bolts.

Furthermore, finite element models and analytical models based on the Timoshenko beam theory and the Kirchhoff-Love plate theory have been developed to obtain a better understanding of the experimental results and to evaluate the design of the actual deck. In particular, the load distribution capability of the GFRP deck has been evaluated and the effective width for shear and bending has been identified.

This study has shown that the design of the GFRP deck is adequate according to the provisions of the City and County of Denver. The deck has a factor of safety of five against failure. The deck also satisfies the deflection limits stipulated in the design provisions. However, the tests and the analyses have indicated that the material orthotropy of the panel and the localized bending effect caused by the soft core can reduce the effective bending width by 25% compared to a homogenous isotropic panel. Furthermore, this and past studies have shown that the governing failure mode of this type of sandwich panel is the delamination of the upper face from the core and that there is a large scatter of the interface shear strength among the test specimens. Hence, this should be a major consideration in design. From the fatigue endurance standpoint, it is recommended that the maximum interface shear be no more than 20% of the shear strength under service loads. In the absence of test data, this recommendation is based on the general recommendation to prevent the creep rupture or fatigue failure of GFRP materials. Furthermore, the anchoring of the panels to the supports requires further studies. This study has shown that mechanical anchor bolts could fail prematurely under the static wheel loads of an HS 25 truck.

Implementation

A GFRP deck has already been constructed and installed in the O'Fallon Park bridge. This project has demonstrated the feasibility of using GFRP decks for highway bridges. However, several issues require special attention. First, the interface shear between a face and the core should be a major consideration in design. It is recommended that the interface shear be less than 20% of the shear strength under service loads. To increase the level of confidence in design, a good quality control is called for to ensure a consistent interface shear strength. The effective bending width of a GFRP panel can be 25% smaller than that of an isotropic panel. However, this is also dependent on the geometry of a panel and the support conditions. A finite element analysis taking into account the material orthotropy and soft core can be conducted to determine the effective bending width. The anchoring of a panel to the supports requires further investigation.

TABLE OF CONTENTS

LIST OF FIGURES

LIST OF TABLES

1 INTRODUCTION

1.1 Background

A large number of highway bridges are in need of repair, replacement, or significant upgrade because of deterioration induced by environmental conditions, increasing traffic volume, and higher load requirements. In the United States, 50% of all bridges were built before the 1940's and approximately 42% of these structures are structurally deficient (Stallings et al. 2000). Many bridges require upgrades because of a steady increase in the legal truck weights and traffic volume. Changes in social needs, upgrading of design standards, and increase in safety requirements lead to the need of major maintenance, rehabilitation, or reconstruction. In some cases, repair and retrofit will not suffice and replacement is the only possible solution. In such a case, there are not only the associated material costs to consider, but also the labor costs, delays, and detours. Hence, a cost-effective solution must consider the minimization of traffic disruption as well as future maintenance needs.

Fiber reinforced polymer (FRP) materials offer high stiffness and strength-to-weight ratios, excellent corrosion and fatigue resistance, reduced maintenance costs, simplicity of handling, and faster installation time compared to conventional materials. However, there is still a great need for further research on durability, performance, and testing and manufacturing standards to develop design guidelines and codes for FRPs, which will lead to a wider use of the materials and, thereby, reduced costs.

Recently, many state transportation departments in collaboration with the Federal Highway Administration (FHWA) are working toward the use of FRP materials for bridge construction. The Innovative Bridge Research and Construction (IBRC) Program of FHWA was initiated with the aim of promoting the use of innovative materials and construction technologies in bridges. Under the IRBC program, the City and County of Denver in cooperation with the Colorado Department of Transportation (CDOT) and FHWA built a bridge with a glass fiber reinforced polymer deck (GFRP) in O'Fallon

Park, which is located west of the City of Denver.

The GFRP deck in the O'Fallon Park bridge is supported on five reinforced concrete risers built over an arch as shown in Figure 1-1. The total length of the deck is 43.75 ft. and the width is 16.25 ft. One of the main objectives of this project is to investigate the feasibility of using FRP decks for highway bridges. Hence, the FRP deck in the O'Fallon Park bridge was designed to have a configuration similar to a highway bridge deck. However, the spans between the concrete risers are a bit shorter than those in a typical highway deck.

The GFRP deck has a sandwich construction with top and bottom faces and a honeycomb core. The deck comprises six 7.29-ft.-wide and 7.5-in.-thick panels as shown in Figure 1-1. They were manufactured in a factory, shipped to the site, and assembled by the supplier, which is Kansas Structural Composites, Inc. (KSCI). The deck is anchored to the concrete risers with bolts secured by epoxy. There are two anchor bolts on each riser for each 7.29-ft.-wide panel. The plan view of the deck is shown in Figure 1-2. The panels are attached to each other with a special type of connection specially designed for this application. The details of the connection will be shown in Chapter 7. The deck is covered by a ½-inch-thick polymer concrete wear surface.

Even though the bridge is mainly for pedestrians and occasionally small vehicles, the deck was designed to carry a standard HS 25-44 truck to allow the passage of fire trucks and garbage trucks. KSCI provided the deck design. Because of the lack of standard design provisions and manufacturing techniques for GFRP deck panels, studies must be conducted to evaluate the design proposed by the manufacturer, and the load-carrying capacity and long-term performance of the selected panels. These studies have been conducted at the University of Colorado at Boulder as part of the IBRC project.

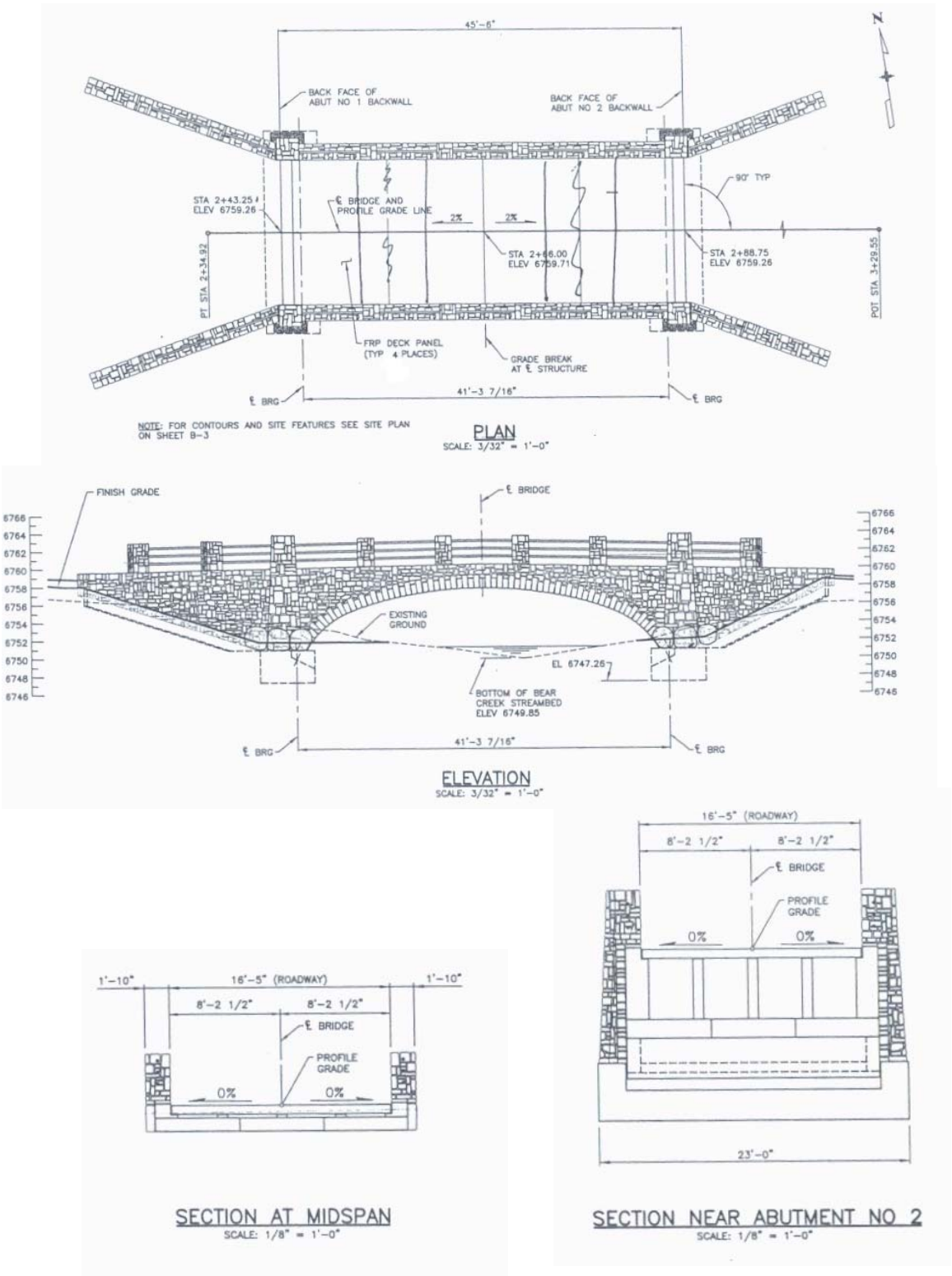

Figure 1-1 Plan, elevation, and section views of the O'Fallon Park bridge

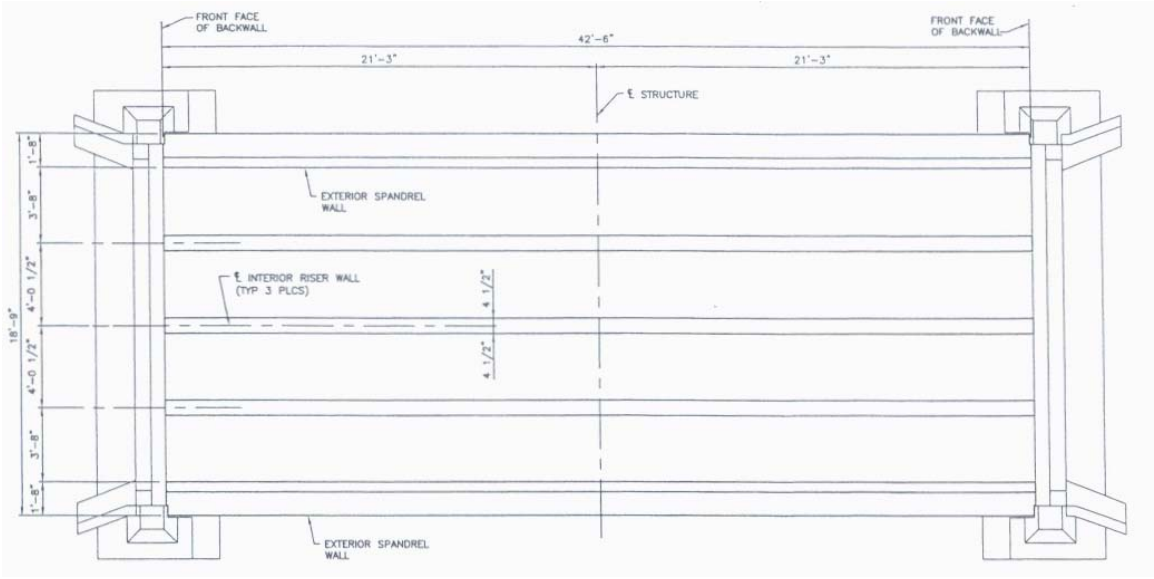

Figure 1-2 Plan view of the O'Fallon Park bridge deck

1.2 Scope of the Study

The studies reported here were divided into two phases. Phase I was intended to evaluate and confirm the candidate deck sections proposed by the manufacturer. To this end, four GFRP beams were tested to evaluate their stiffness and load-carrying capacities and compression tests were conducted to evaluate the crushing capacities of the panels. The stiffness, load-carrying capacity, and failure modes of the beams were identified. The deflections of the beams were compared to the requirement stipulated in the design provisions of the City and County of Denver. In Phase II, the load-carrying capacity and fatigue endurance of a full-size two-span GFRP panel that had the same design as the actual bridge deck was studied. The panel was supported on three reinforced concrete risers and anchored to the supports using the same details as the actual bridge. The aim was to investigate the influence of load cycles on the load-carrying capacity of a panel and on the performance of the anchor bolts. Once the fatigue test was completed, the panel was loaded to failure to determine the ultimate load-carrying capacity and the governing failure mode.

Furthermore, finite element models and analytical models based on the Timoshenko beam theory and the Kirchhoff-Love plate theory have been developed to obtain a better understanding of the experimental results and to evaluate the design of the actual deck. In particular, the load distribution capability of the GFRP deck has been evaluated and the effective width for shear and bending has been identified.

1.3 Organization of the Report

In Chapter 2, the design, section properties, and manufacturing process of the GFRP panels used in the O'Fallon Park bridge are briefly summarized. The mechanical properties of the GFRP materials used in the panels are presented in Chapter 3. In Chapter 4, the design evaluation conducted on the bridge deck is presented. Chapter 5 presents the experimental studies conducted in Phase I on four simply supported GFRP beams and the crushing tests performed on four GFRP specimens. In Chapter 6, the numerical and analytical studies conducted on the test beams with the Timoshenko beam theory and finite element models are presented. Chapter 7 describes the static load tests and fatigue test conducted in Phase II on a full-size two-span deck panel that had the same design as the actual deck. Chapter 8 presents the analytical study conducted on the test panel with the Kirchhoff-Love plate theory to investigate the load-resisting behavior of a GFRP deck, including the effective bending width and the influence of material orthotropy. In Chapter 9, the finite element analyses performed on the test panel are presented. The analyses are to evaluate the analytical model based on the plate theory, the influence of the shear deformation of the honeycomb core and support conditions on the effective bending width, and the design of the actual deck based on the experimental results. Summary and conclusions are provided in Chapter 10.

2 DECK MANUFACTURING PROCESS

This study focuses on the load-carrying behavior of glass fiber reinforced polymer (GFRP) bridge deck panels manufactured by Kansas Structural Composites, Inc. (KSCI) using a hand lay-up technique. The deck panels are constructed using a sandwich panel configuration, which consists of two stiff faces separated by a lightweight core. The core has a sinusoidal wave configuration in the x_1-x_2 plane, as shown in Figure 2-1.

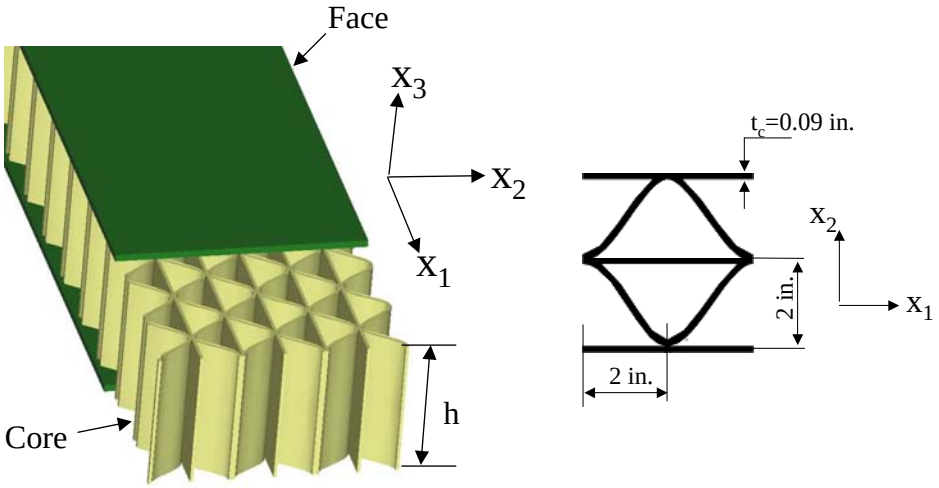

(a) Panel (b) RVE

Figure 2-1 Configuration of the core and the faces

The sinusoidal wave has an amplitude of 2 in. and the core material has a thickness of 0.09 in., as shown in Figure 2-1(b). Figure 2-1(b) shows a Representative Volume Element (RVE), which is a single basic cell that is repeated periodically to form the core structure. The panel was designed for one-way bending about the x_2 axis. Therefore, the bending stiffness about the x_2 axis is much higher than that about x_1.

Plunkett (1997) described in detail the panel manufacturing process. The honeycomb core is composed of a flat GFRP sheet bonded to a corrugated GFRP sheet as shown in Figure 2-1. The core flat parts are laid up on a flat surface with vinylester resin manually applied to chopped strand mat reinforcement. The corrugated parts are

fabricated in the same fashion as the flat parts but on corrugated molds. The flat parts are then placed on top of the wet corrugated parts to produce a bond as the corrugated parts cure. The face is composed of fiberglass fabric layers, which are wet in resin and laid up upon each other until desired face thickness is obtained.

To increase the interface shear strength between the core and the faces, a new detail is introduced in the manufacturing process for the O'Fallon Park bridge panels. In the panels, GFRP mats are inserted between the core and the faces at about 13 in. distance as shown in Figure 2-2(b).

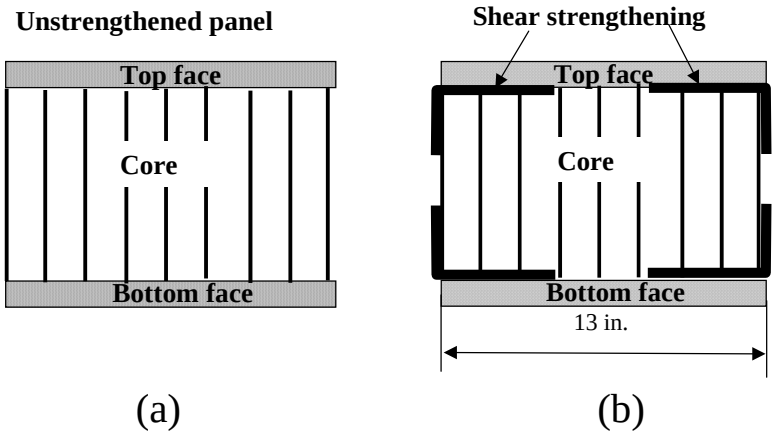

Figure 2-2 Shear strengthening details

Figure 2-2 shows that the shear strengthening also increases the thickness of the faces and thereby the bending resistance of the structural members. This must be considered in analysis.

3 MATERIAL PROPERTIES

The honeycomb panels manufactured by Kansas Structural Composites, Inc. (KSCI) are normally designed for one-way bending about the x_2 axis as shown in Figure 2-1. For this reason, most of the past research has been focused on the tensile properties of the materials in the x_1 direction. Table 3-1 shows the properties of material samples from the core flat parts and faces of a panel in the direction x_1 which were obtained by Lopez (2001).

Table 3-1 Tensile properties of face and core samples

Property	Core flat parts	Face
Ultimate Tensile Strain	0.014	0.016
Modulus of Elasticity E_{11} (ksi)	1158	2840

In reality, a panel bends in both directions, and to model such behavior accurately, the orthotropic bending properties of a panel must be considered. However, it would be computationally too involved to consider the complicated geometry of the core in such analysis. For this reason, homogenization theories have been used to find equivalent material properties for modeling and design purposes.

Davalos et al. (2001) have developed a method to calculate the equivalent stiffness properties of the core and the faces using micromechanical and macromechanical models. The equivalent core properties are obtained by using a homogenization theory. The homogenization theory exploits the in-plane periodicity of the structure. The objective is to substitute the heterogeneous structure with an equivalent homogeneous structure. The equivalent face properties are calculated by applying a micromechanical approach combined with the classical laminate theory. They have shown that the theoretical results compare well with finite element (FE) analyses and experimental data. The orthotropic material properties of the faces and the core calculated by Davalos et al. (2001) are presented in Table 3-2.

Table 3-2 Homogenized face and core material stiffness properties

	Elastic Moduli (ksi)						Poisson Ratios		
	E_{11}	E_{22}	E_{33}	G_{12}	G_{13}	G_{23}	ν_{12}	ν_{13}	ν_{23}
Core	76.8	0.102	183	0.102	47.7	20.2	0.431	0.169	0.0000273
Face	2846	1850		546			0.302		

It should be noted that E_{11} of the face material obtained by Davalos et al. (2001) is very close to the test result shown in Table 3-1. Furthermore, Davalos et al. (2001) have modeled the honeycomb sandwich panel as a three layer laminated system and using classical lamination theory they have computed the effective stiffness properties for a sandwich panel as a whole. The panel considered by Davalos et al. (2002) had a total thickness of 5 in. and a face laminate thickness of 0.425 in. The results are shown in Table 3-3.

Table 3-3 Equivalent stiffness properties of GFRP honeycomb sandwich panel

Elastic Moduli (ksi)			Poisson Ratio
E_{11}	E_{22}	G_{12}	ν_{12}
1273	803	236	0.301

The equivalent properties provided in Table 3-3 can be used with plate theory to analyze the load-displacement behavior of a panel.

4 EVALUATION OF DECK DESIGN FOR THE O'FALLON PARK BRIDGE DECK

4.1 General

For FRP deck panels, there are no standard guidelines for design, and design methods differ from manufacturer to manufacturer (Busel and Lindsay 1997). The panels in O'Fallon Park bridge were designed and manufactured by Kansas Structural Composites, Inc. (KSCI). A schematic of the deck is shown in Figure 4-1.

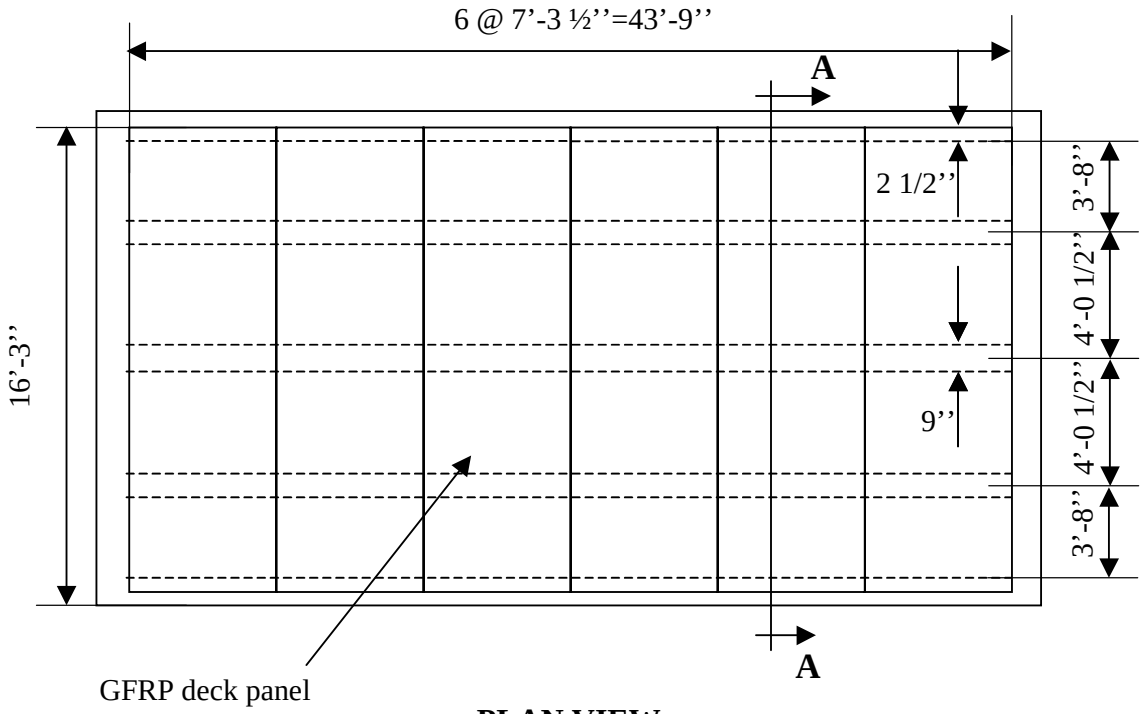

PLAN VIEW

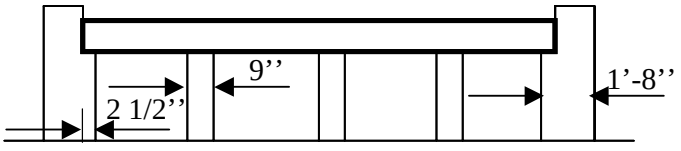

SECTION A-A

Figure 4-1 Schematic of the bridge deck

Six 16'-3'' by 7'-3 1/2'' GFRP panels are used for the bridge deck. The bridge is owned by the City and County of Denver, which has special design provisions (City and County of Denver 2002) for the deck. In Section 600 of the provisions, there are specifications on materials, design requirements, and manufacturing quality control. The manufacturer designed the deck following these specifications. They initially proposed several candidate sections for the deck. These sections were evaluated analytically at the University of Colorado. Two of these sections were later evaluated by beam tests. The final design was selected based on results of these tests. The following sections describe the design specifications and the calculations used to examine the different panel sections proposed by the manufacturer.

4.2 Design Requirements

4.2.1 Structural Loads

For this bridge, the design live load specified is an HS 25 truck. This leads to a design wheel load of 20 kips. With an impact factor of 30%, the design load becomes 26 kips per wheel.

4.2.2 Tire Contact Area

In the AASHTO LFRD Specifications (1998), the tire contact area is considered a rectangle with a width of 20 in. and a length l given by:

$$l = 2.28\gamma\left(1+\frac{IM}{100}\right)P \tag{4.1}$$

where γ is the load factor, IM is the impact factor, and P is the wheel load.

For this case, γ = 1.75, IM = 30, and P=20 kips. Hence, l=19 in., which leads to a contact area of 380 square inches.

4.2.3 Load Transfer

The load transfer capability of a honeycomb panel is not well understood. Therefore, to determine the effective width for design, some assumptions are necessary. For this evaluation, assumptions were made based on the AASHTO Standard Specifications (1996) for concrete slabs. AASHTO distinguishes between two cases for slabs supported along two edges: (1) main reinforcement perpendicular to the traffic, and (2) main reinforcement parallel to the traffic.

In the first case, the live load moment for a simple span shall be determined by the following formula (impact not included):

$$M' = \left(\frac{S+2}{32}\right)P \quad \textit{Moment in foot-pounds per foot-width of slab} \tag{4.2}$$

where S is the effective span length in feet and P is the wheel load in pounds. For slabs continuous over more than two supports, the effective span is defined as the clear span. To estimate the effective bending width for a one-way slab, the load per foot-width of a slab is given as:

$$P' = \frac{4M'}{S} \quad \textit{Load in pounds per foot-width of slab} \tag{4.3}$$

The effective bending width in feet is then calculated as follows:

$$w_b = \frac{P}{P'} \tag{4.4}$$

Equation (4.2) is a semi-empirical formula based on plate theory, and *M'* represents the maximum moment per unit width. Equation (4.4) gives a conservative estimate of the effective bending width for brittle materials like FRP, where failure is dominated by the maximum stress.

4.2.4 Deflection Criterion

According to the City and County of Denver provisions, the panel should be designed so that the deflection due to service load plus impact shall not exceed 1/1000 of

the span length.

4.2.5 Flexure Criteria

Section 600 of the City and County of Denver provisions suggests using both Allowable Stress Design and Load Factor Design approaches as follows.

The maximum strain shall be limited to 20% of the ultimate strain under service loads and the maximum dead load strain shall be limited to 10% of the ultimate strain.

The maximum Factored Load shall be given by:

$$P = 1.3x(1.67x(LLxIM)+DL)) \quad (4.5)$$

and it shall not exceed 50% of ultimate load capacity. In equation (4.5), *LL* is the Live Load, *IM* is the Impact Factor, and *DL* is the Live Load.

In the City and County of Denver provisions, there is no specification on the effective width of a panel. According to equation (4.4), the effective bending width for the bridge deck is 5.3 ft. Therefore, in this evaluation, the effective width for bending, w_b, was conservatively assumed to be four feet.

4.2.6 Shear Criteria

The shear failure mode for the honeycomb sandwich panel used for the O'Fallon bridge deck is expected to be different from that for reinforced concrete (RC) decks. GFRP sandwich deck fails in shear when a face delaminates from the core, and previous experimental studies (Stone et al. 2001 and Lopez 2001) have shown that this mode is most often the governing failure mode for this type of panel.

Section 600 of the City and County of Denver provisions indicates that the maximum Factored Load shall be given by equation (4.5) and it shall not exceed 45% of the ultimate shear load capacity of the deck.

In this evaluation, the effective width for shear, w_s, was assumed to be equal to the panel width, which is seven feet. This is because delamination in one spot will not necessarily lead to a complete delamination in a panel. However, results of the study presented later in this report indicate that this assumption needs to be revisited.

4.2.7 Crushing Criteria

The crushing failure load can be calculated by assuming a contact area of 380 in.^{2} (AASHTO 1998). According to the provisions of the City and County of Denver (2002), the maximum Factored Load shall be given by equation (4.5) and it shall not exceed 45% of the crushing failure load.

4.2.8 Thermal Expansion

Section 600 of the City and County of Denver provisions states that the supplier has to demonstrate through analysis or testing that the FRP bridge deck structure is thermally compatible with both steel and concrete girder systems.

4.3 Deck Analysis

4.3.1 General

This section provides a description of the analysis conducted to evaluate the load-carrying capacities of five candidate panel sections proposed by KSCI. A three-point bending configuration was considered in the analysis. The panel span, L, was assumed to be 48.5 in., which is the center-to-center distance of an interior span of the actual deck, and the panel was assumed to be loaded at midspan. Five panel cross sections proposed by the manufacturer were analyzed to compare costs and performances. The analysis results are summarized in Table 4-1.

Table 4-1 Summary of analysis results

				(1)	*(2)*	*(3)*	*(4)*	*(5)*	*(6)*
Panel Section	**h**	**s**	**Total Weight**	**$\varepsilon_s/\varepsilon_{ult}$**	**50 % P_F**	**45 % P_S**	**45% P_C**	**δ**	**P_U/P**
	in	*in*	*lbs/ft^2*		*kips*	*Kips*	*kips*	*in.*	
1	6.5	0.375	12.5	11% (20%)	133 (56.5)	65 (56.5)	137 (56.5)	0.053 (0.05)	5.55
2	6.5	0.5	14.5	9% (20%)	155 (56.5)	65 (56.5)	137 (56.5)	0.041 (0.05)	5.55
3	6.5	0.625	16.5	7% (20%)	192 (56.5)	65 (56.5)	137 (56.5)	0.033 (0.05)	5.55
4	8.0	0.375	14.0	9% (20%)	147 (56.5)	80 (56.5)	137 (56.5)	0.035 (0.05)	6.83
5	8.0	0.5	16.0	7% (20%)	193 (56.5)	80 (56.5)	137 (56.5)	0.028 (0.05)	6.83

In Table 4-1, ε_s is the strain under the service truck load of 26 kips, ε_{ult} is the ultimate strain, P_F is the Ultimate Bending Capacity, P_S is the Ultimate Shear Capacity, P_C is the Ultimate Crushing Capacity, δ is the maximum displacement under the service load, P_U is the ultimate load capacity which is the smallest of P_F, P_S and P_C, and P is the service load. The numbers in the braces represent the design requirements. The parameters *h* and *s* are defined in Figure 4-2.

In column (1), the maximum strain under the service load shall be limited to 20% of the ultimate strain according to the design requirements in section 4.2. In columns (2), (3) and (4), the calculated Maximum Factored Load is 56.5 kips and shall be less than 50% of the Ultimate Bending Capacity, and 45% of the Ultimate Shear and Crushing Capacities. In column (5), the maximum displacement at midspan shall be smaller than $L/1000 = 0.05$ in. In column (6), the ratio P_U/P represents the factor of safety against failure.

The panel was designed assuming one-way bending. The nonhomogeneous panel section was converted to an equivalent homogeneous section using the transformed section method.

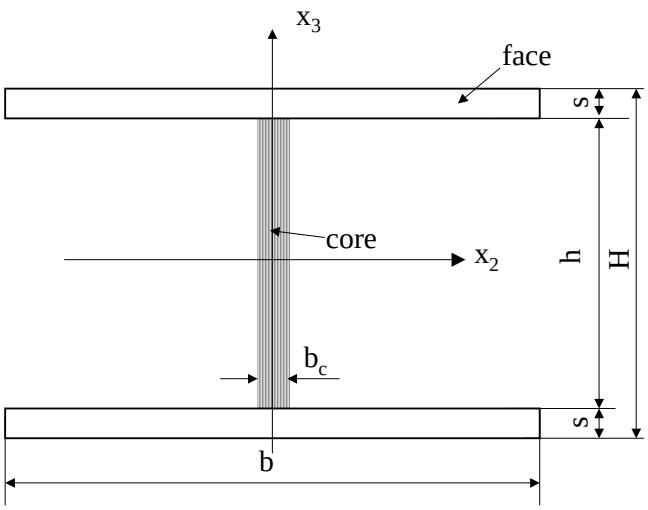

Figure 4-2 Schematic of a beam section

The material properties used in the calculations were based on the homogenized properties given in Table 3-2 , and the ultimate tensile properties given in Table 3-1. In the direction x_1, the homogenized elastic modulus of the face was E_{f11} = 2840 ksi, and the elastic modulus of the core was E_{c11} = 76 ksi. Thus, the modulus ratio $n = E_{c11} / E_{f11} = 0.0268$. The equivalent core width of a transformed section was calculated as follows.

$$b_c = nb \tag{4.6}$$

where b is the width of a panel strip. The moment of inertia with respect to bending about x_2, I_2, was calculated considering a transformed section.

$$I_2 = \frac{bs^3}{6} + 2bs\left(\frac{h}{s} + \frac{s}{2}\right)^2 + n\frac{bh^3}{12} \tag{4.7}$$

4.3.2 Flexural Strength

The maximum flexural strain under the service load has to be less than 20% of the ultimate strain. To take into account of the possible strength reduction of the composite material in compression, the ultimate strain was conservatively assumed to be 50% of the ultimate strain in tension shown in Table 3-1. This resulted in an ε_{ult} of 0.008. The strain at the top of the panel, ε_{top}, under the service load was calculated by using the flexure formula.

$$\varepsilon_{top} = \frac{M}{E_{f11} I_2} \frac{H}{2} \tag{4.8}$$

where I_2 is the moment of inertia with respect to bending about x_2, and was calculated with equation (4.7) with b = 4 ft., which is the assumed effective bending width, w_b, E_{f11} is the Young's modulus of the face, H is the height of the beam, and M is the bending moment. For a simply supported beam, the moment, M, is related to the applied load as follows.

$$M = \frac{PL}{4} \tag{4.9}$$

where L is the span of the panel and P=26 kips. The strain at the service load ε_s was calculated for each panel section. The $\varepsilon_s/\varepsilon_{ult}$ values are shown in column (1) of Table 4-1.

The maximum Factored Load has to be less than the 50% of ultimate bending load capacity. The ultimate moment capacity was calculated by assuming $\varepsilon_{top}=\varepsilon_{ult}=0.008$ and solving equation (4.8) for the moment, M; the ultimate load capacity, P_F was calculated by solving equation (4.9) for P. The results are shown in column (2) of Table 4-1.

Columns (1) and (2) of Table 4-1 show that the strain limitation requirement and the ultimate bending capacity are satisfied for all the five panel sections considered.

The displacement at midspan was obtained using the Timoshenko beam theory:

$$\delta = \frac{PL^3}{48 E_{f11} I_2} + \frac{PL}{4 \kappa G_{c13} A} \tag{4.10}$$

where E_{f11} is the elastic modulus of the faces in the x_1 direction, G_{c13} is the homogenized shear modulus of the core as given in Table 3-2, κ is the shape factor, and A is the cross sectional area that resists shear. The deflection was calculated assuming an effective bending width of 4 ft. In this study, the cross section was considered a flanged section, and, therefore, κ was conservatively assumed to be 1.0. A was calculated considering only the cross-sectional area of the core, i.e., $A=bh$. Column (5) of Table 4-1 shows that the deflection requirement is satisfied for four of the panel sections considered. Even

though the first panel section slightly violates this requirement, it is considered acceptable as the analysis is based on a conservative assumption of a panel simply supported along two edges. In the actual bridge, the panel is continuous over five supports.

4.3.3 Crushing Failure

A panel is assumed to fail in crushing when the maximum crushing stress calculated exceeds the ultimate crushing stress.

The ultimate crushing stress, σ_c, was estimated with previous experimental results (Lopez 2001). A beam tested by Lopez failed because of the crushing of the core. The ultimate load recorded was 115 kips. The area of the loading plate was 12 in. by 12 in. However, the actual contact area, A_c, consists of only the flat and the corrugated parts of the core. By considering one RVE (Representative Volume Element) as shown in Figure 2-1(b), the cross-sectional area of the flat parts is given by:

$$A_{flat} = 2t_c \times 4 \quad \left[\text{in}^2\right] \tag{4.11}$$

and the area for the corrugated parts is given by:

$$A_{corrugated} = 2.93 \times \text{t}_\text{c} \times 4 \left[\text{in}^2\right] \tag{4.12}$$

where 2.93 in. is the arc length of a quarter sine wave. In a 12x12 in.^{2} area, there are 9 RVE. Therefore, the actual contact area is:

$$A_c = 9 \times A_{flat} + 9 \times A_{corrugated} \tag{4.13}$$

Hence, the ultimate crushing stress is:

$$\sigma_c = \frac{P_c}{A_c} = 7.2ksi \tag{4.14}$$

where P_c is the crushing load.

For design purposes, it is useful to adopt the nominal crushing stress calculated with the area of the loading plate instead of the actual core area. The loading area in this case is A=12in.x12in. = 144 in^2. Thus, the nominal crushing stress was calculated to be:

$$\sigma_{c,nom} = \frac{P_c}{A} = 0.8 \text{ ksi} \tag{4.15}$$

The beam tested by Lopez (2001) was 2.5-ft. deep and had 0.5-in.-thick top and bottom faces. Since core crushing is very much governed by the geometric stability, a deeper core is expected to have a lower crushing load. Hence, the nominal crushing stress shown in equation (4.16) was deemed conservative for the panels considered here and was, therefore, adopted. The ultimate crushing capacity for the panels was calculated by assuming a tire contact area of 380 in.^{2} (AASHTO 1998). The results are shown in column (4) of Table 4-1. The maximum Factored Load has to be less than the 45% of the ultimate load capacity, and column (4) of Table 4-1 indicates that this requirement is satisfied for the panel sections considered.

4.3.4 Shear Failure

The shear failure of a GFRP sandwich panel is quite different from the shear failure observed for reinforced concrete structures. Based on the published literature, the failure of GFRP panels manufactured by KSCI is normally triggered by the delamination of the top face from the core. In this report, such a failure mode is considered shear failure. Hence, a GFRP panel is considered to fail in shear when the shear stress at the interface between the face and the core reaches the interface shear strength.

For the O'Fallon bridge deck, it is important to consider the dimensions of the support and loading area in the calculation of the nominal interface shear stress because their dimensions are not negligible compared to the panel span. To evaluate the nominal interface shear stress in a beam, a segment between the edge of the loading area and the free end was considered as shown in Figure 4-3. In Figure 4-3, *d* is the distance between the edge of the loading area and the center of the closest support. By using the simple beam theory and assuming a perfect bond between the face and the core, the following formula can be derived:

$$F = \frac{1}{4} b \sigma_{11}^{top} \left(H - \frac{h^2}{H} \right) \tag{4.17}$$

where F is the force acting on the face at a distance d due to bending as indicated in Figure 4-3, σ_{11}^{top} is the nominal stress in direction x_1 at the top of the face, and b, H and h are dimensions defined in Figure 4-3.

The bending stress at the top of the beam is given by:

$$\sigma_{11}^{top} = \frac{PH}{4I_2} d \tag{4.18}$$

To calculate the nominal shear stress, τ_{13}^{int}, at the interface between the face and the core, the following equation is used:

$$\tau_{13}^{\text{int}} = \frac{F}{A_s} = \frac{F}{xb} \tag{4.19}$$

where b is the nominal width and x is the distance between the end of the panel and the edge of the loading area as indicated in Figure 4-3. By substituting equation (4.18) in (4.17), and then substituting equation (4.17) in (4.19), the nominal shear stress, τ_{13}^{int} can be expressed as:

$$\tau_{13}^{\text{int}} = \frac{PdH}{16I_2 x}\left(H - \frac{h^2}{H}\right) \tag{4.20}$$

The shear stress calculated with equation (4.20) is considered as the nominal shear stress. The nominal width, b, was chosen because the actual contact width was difficult to determine with the new shear strengthening detail shown in Figure 2-2.

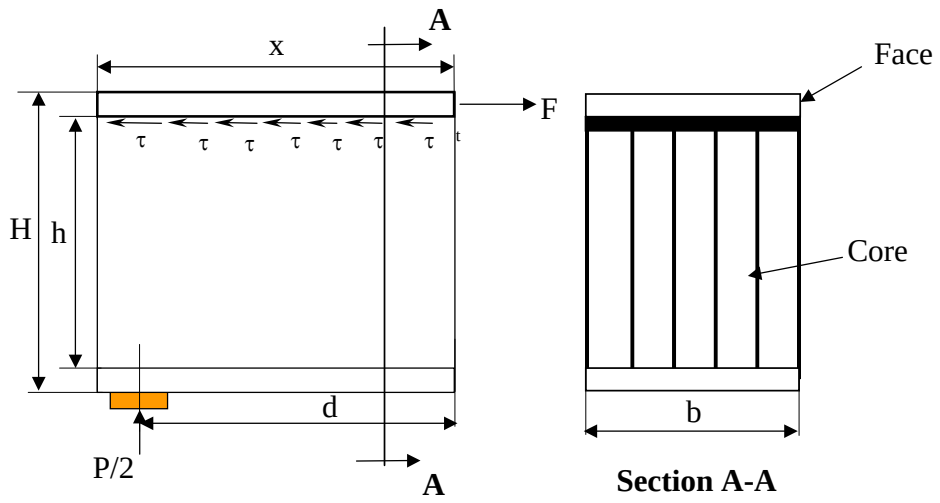

Figure 4-3 Schematic for the shear stress calculation

The Ultimate Shear Capacity, P_S, is defined as the load at which the nominal interface shear stress is equal to the ultimate shear strength, τ_{ult}. Thus, by rearranging equation (4.20) and letting $\tau_{13}^{\text{int}} = \tau_{ult}$, we have:

$$P_S = \frac{16 I_2 x}{d(H^2 - h^2)} \tau_{ult} \tag{4.21}$$

For the O'Fallon Park deck, the *b* value used to calculate I_2 was assumed to be 7 ft., which was the assumed effective width for shear, the tire contact width perpendicular to the direction of the traffic is 20 in. (AASHTO 1998), and the support for the deck is 9 in. wide. Hence, with the conservative assumption that the deck has a simply supported span of 48.5 in. and that the wheel load is at midspan, *x* is 18.75 in. and *d* is 14.25 in.

The ultimate interface shear strength, τ_{ult}, was estimated from the results of the four beam tests conducted by Lopez (2001) and Stone et al. (2001). By using equation (4.20), the nominal shear stress at failure was calculated to be 0.08 and 0.085 ksi for the two beams tested by Lopez, and 0.14 and 0.21 ksi for the beams tested by Stone et al. Because of the small number of data available, the lowest shear stress of 0.08 ksi was used as the ultimate shear strength for the analysis here.

The maximum Factored Load has to be less than the 45% of the Ultimate Shear

Capacity, and Column (3) of Table 4-1 indicates that this requirement is satisfied for all the panel sections considered.

Moreover, it must be mentioned that the manufacturer of the O'Fallon Park bridge deck had improved the interface shear strength by providing a shear strengthening detail as shown in Figure 2-2. The beam tests presented later in this report show that the new shear strengthening method can indeed substantially increase the face-core interface shear strength.

4.3.5 Thermal Effect

For FRP structures, the thermal effect could be a critical factor. For the continuous panels in the O'Fallon Park bridge, thermal stresses introduced by the differential temperature across a panel section could be significant. For this reason, a thermal analysis was conducted by assuming a severe temperature differential of ΔT = = 50 ºF, between the top and bottom faces of a panel. Figure 4-4 shows a two-span continuum deck considered in this analysis. The thermal stresses can be calculated with the principle of superposition by first removing the center support and reapplying the support reaction *P* as shown in Figure 4-4.

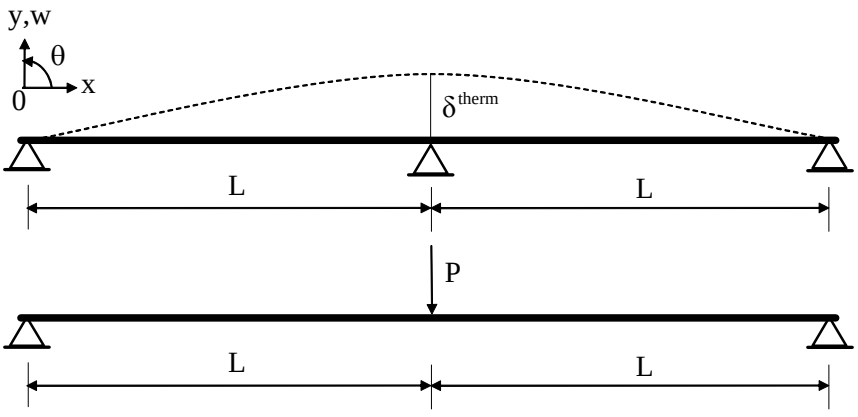

Figure 4-4 Schematic for thermal load calculation

The coefficient of thermal expansion given by the manufacturer is α = 28x10^{-6} / ºC. The curvature induced by a thermal gradient is given by the following equation:

$$\phi = \frac{\alpha \Delta T}{H} \tag{4.22}$$

The rotation of an infinitesimal segment is thus obtained as:

$$d\theta = \frac{\alpha \Delta T}{H} dx \tag{4.23}$$

and the deflection at midspan can be found by applying the principle of Virtual Work:

$$\delta^{therm} = 2\int_0^L M_v d\theta = 2\int_0^L \frac{1}{2} x \frac{\alpha \Delta T}{H} dx \tag{4.24}$$

where M_v is the virtual moment due to a unit point load applied at midspan in the same direction as the displacement δ.

Therefore, the deflection at midspan is:

$$\delta^{therm} = \frac{\alpha \Delta T L^2}{2H} \tag{4.25}$$

The deflection due to the force *P* applied at midspan as shown in Figure 4-4 is:

$$\delta = \frac{8PL^3}{48E_{f11}I_2} \tag{4.26}$$

By having $\delta^{therm} = \delta$, the force *P* is found as follows:

$$P = \frac{3\alpha \Delta T E_{f11} I_2}{HL} \tag{4.27}$$

The shear stress due to the force *P* obtained with equation (4.27) can be calculated with equation (4.20). For a differential temperature of 50 ºF, the shear stress, τ_{13}^{int}, is 0.01 ksi for panel section 1, 0.01 ksi for panel section 2, 0.02 ksi for panel section 3, 0.01 ksi for panel section 4, and 0.02 ksi for panel section 5. These are lower than the assumed ultimate shear strength of 0.08 ksi.

4.4 Summary

In summary, all five panel sections considered here satisfy the design requirements of Section 4.2. Panel sections 1 and 2 were chosen for further evaluation with beam tests because they provide the required structural performance, light weight, and desired panel depths.

5 BEAM TESTS

5.1 Introduction

Section 600 of the City and County of Denver provisions requires performance testing of samples of deck panels selected for the O'Fallon Park bridge. To this end, beam specimens were tested at the University of Colorado at Boulder to evaluate the stiffness and ultimate load capacity of different panel sections.

The tests followed the procedures specified in Section 600 of the City and County of Denver provisions. The beams were tested under third-point loading with a span of 48.5 in., which is the span length of the actual bridge deck. However, the actual deck spans continuously over five reinforced concrete risers as shown in Figure 1-1.

Section 600 of the City and County of Denver provisions requires that the midspan deflection of a one-foot-wide beam shall not exceed 1/500 of the clear span when subjected to a point load of 10,000 lbs. In addition, the provisions require that the sections shall be loaded until failure to evaluate the ultimate load capacity of the specimens. The following sections describe the test specimens, test setup, and results.

5.2 Test Specimens

A total of four beams, which represented candidate sections for the deck panels of the O'Fallon Park bridge, were tested in bending using third-point loading. Based on the evaluation presented in Chapter 4, two types of beam sections were selected with two for each type. All the beams had a core height of 6.5 in. Two of the beams had 0.375-in. faces and the remaining two 0.5-in. faces as shown in Table 5-1. The section with 0.375-in. faces is the lightest section that satisfies the design requirements. The beams were wrapped with external layers of GFRP to increase the shear resistance at the core-face interface as shown in Figure 5-1.

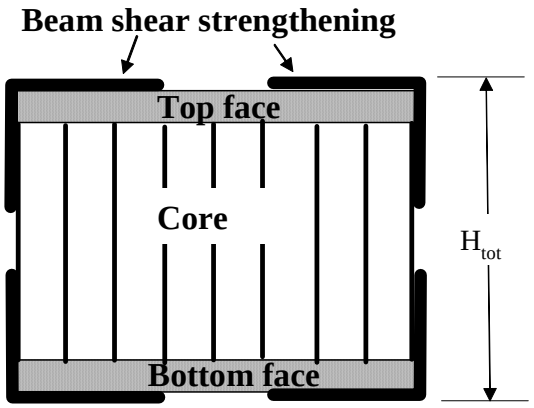

Figure 5-1 Beam shear strengthening detail

The shear strengthening increased the thickness of the faces and, hence, the bending resistance of the beams. To take into account this strengthening, the moment of inertia of the beams, *I* in Table 5-1, was calculated with a thickness increase of 0.09 in. for each face. H_{tot} in Table 5-1 is the total height of the beams including the thickness of the shear strengthening material.

Table 5-1 Beam dimensions

	b *in*	**h** *in*	**s** *in*	**H** *in*	**H_{tot}** *in*	**I** *in^4*
Test 1	13	6.5	0.375	7.25	7.43	155
Test 2	12	6.5	0.375	7.25	7.43	143
Test 3	13	6.5	0.5	7.5	7.68	201
Test 4	13	6.5	0.5	7.5	7.68	201

In Table 5-1, *b*, *h*, *s*, and *H* are defined in Figure 4-2, and *I* is the moment of inertia calculated using equation (4.7). The panel sections shown in Table 5-1 were selected because they satisfy the required structural performances and were also cost-effective. Two different face thicknesses were tested to evaluate the effect of the face thickness on the beam performance. Two beams of each section type were tested to assess the repeatability of the results. However, it must be pointed out that the beam in Test 2 had a different width, which was introduced unintentionally in the manufacturing process.

5.3 Instrumentation

Electrical high precision strain gages produced by Micro Measurements Group, Inc., with a resistance of 350 ohms, were used along with M-Bond Type AE 10 adhesive system to measure strains in the axial direction of the beams. Deflection at midspan was monitored using a Linear Variable Differential Transformer (LVDT). Mechanical dial-gauges were mounted to check the LVDT readings. Displacement, strain and load readings were recorded during the tests using a data acquisition system. Figures 5-2 to Figure 5-5 show a schematic of the strain gauge locations for the four beam tests. Test 1 and Test 3 had gages glued on the front and back of the beams, whereas Test 2 and Test 4 had gages only on the front. The gages on the top and bottom faces were located right at the center of the face.

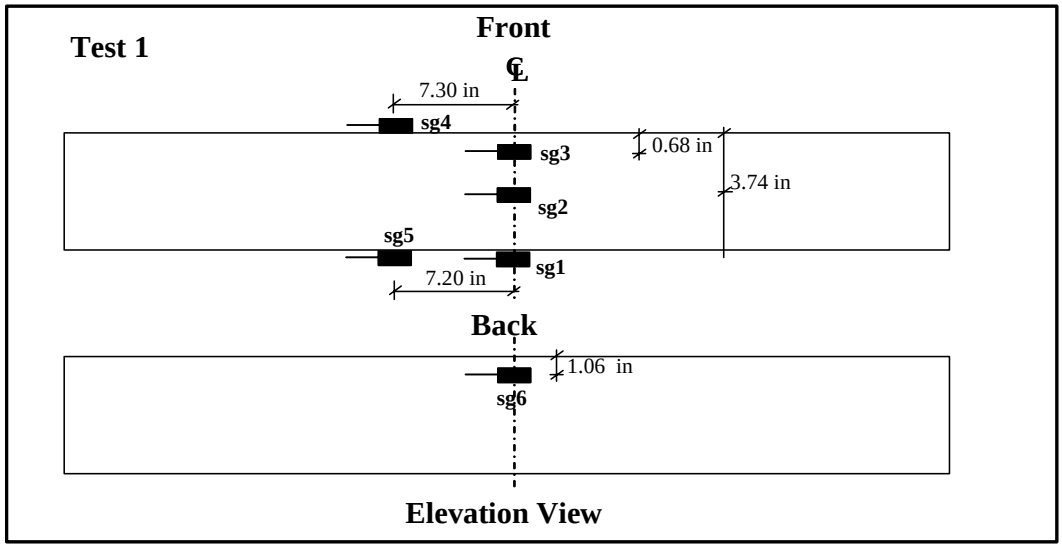

Figure 5-2 Strain gages for Test 1 (face thickness = 0.375 in)

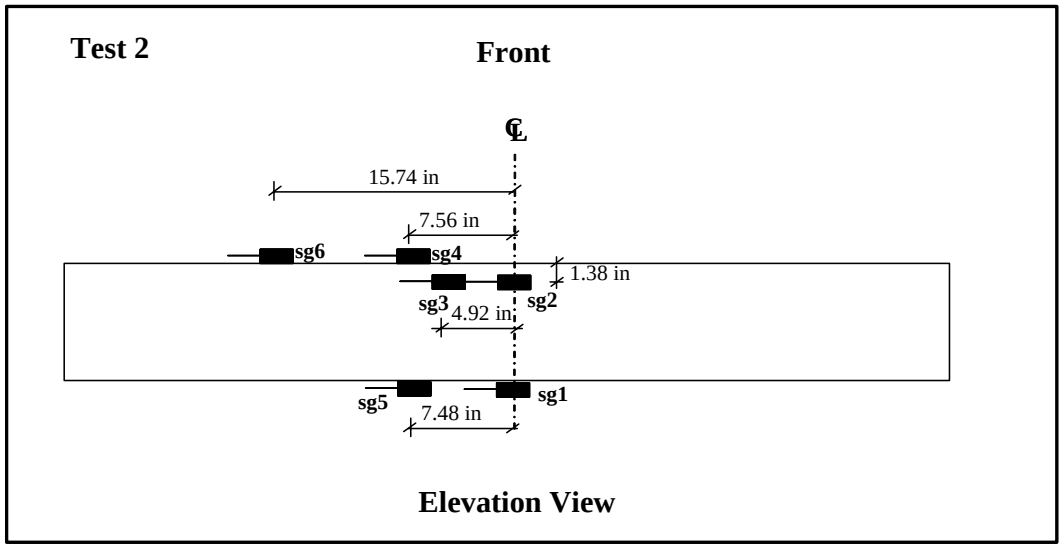

Figure 5-3 Strain gages for Test 2 (face thickness = 0.375 in.)

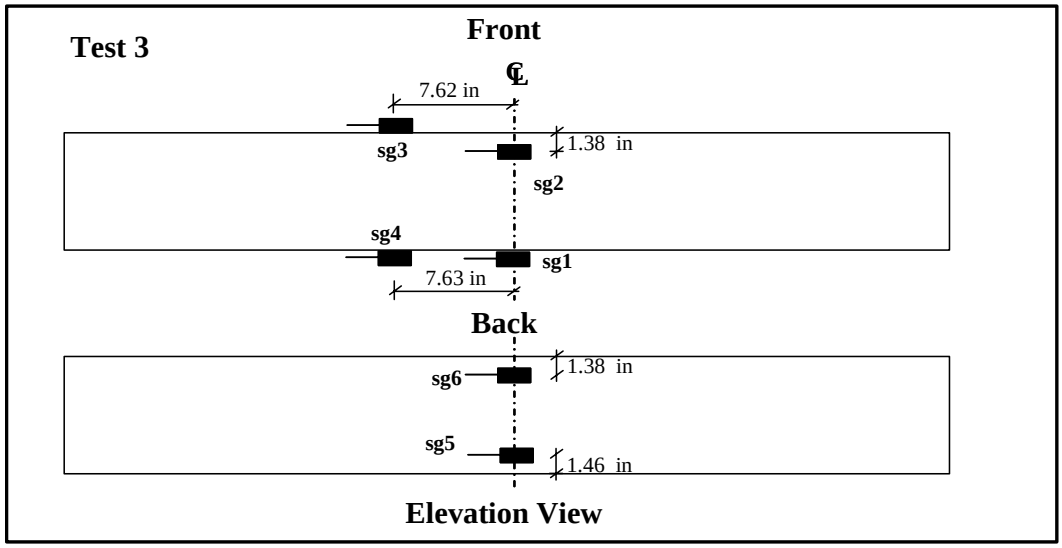

Figure 5-4 Strain gages for Test 3 (face thickness = 0.5 in.)

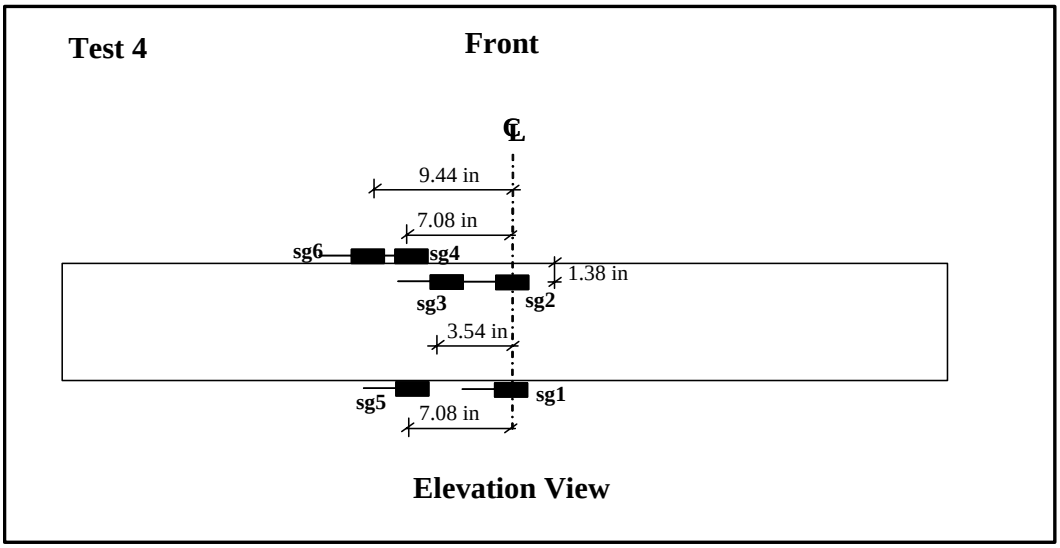

Figure 5-5 Strain gages for Test 4 (face thickness = 0.5 in.)

5.4 Test Setup

All beams were tested with a concentrated load at midspan. The test setup is illustrated in Figure 5-6 and Figure 5-7.

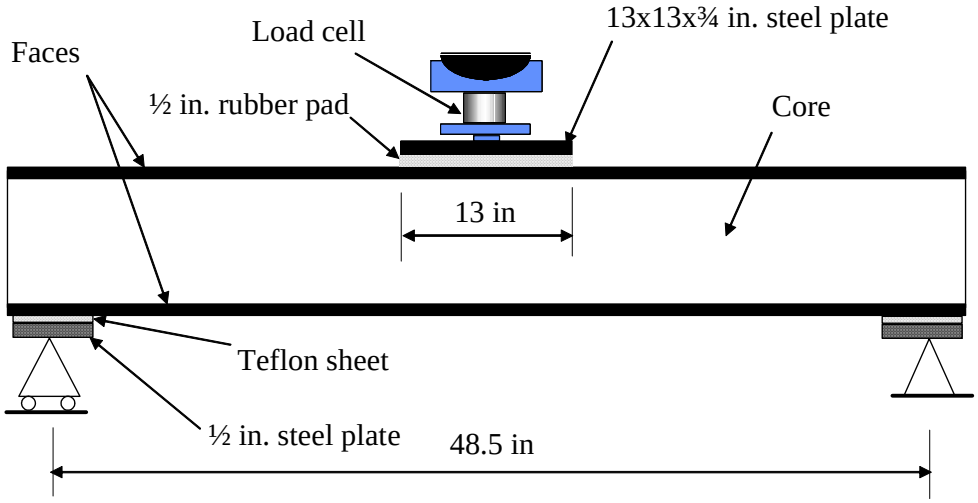

Figure 5-6 Schematic of the beam test setup

Figure 5-7 Beam test setup

The beams were simply supported on rollers at each end and the load was distributed uniformly using a 13x13x3/4-in. steel plate. The beams were tested using a rate of loading of approximately 0.0075 in./min. Data was recorded at a rate of one sample per second using a 16-channel data-acquisition system.

Crushing tests were also conducted on small panel samples to evaluate the uniaxial compression strength. The following sections present the results of the crushing tests and bending tests.

5.5 Crushing Tests

The manufacturer provided four 13-in.-by-12-in. specimens for crushing tests. Like the beam specimens, the height of the core was 6.5 in. Two were manufactured with 0.375-in. face and two with 0.5-in. face. They were fabricated together with the beams and were cut from the originally longer beams specimens. An MTS machine with a load capacity of one million pounds was used. All the specimens were tested under displacement control. The aim of these tests was to find the ultimate crushing load of the specimens.

The test setup is illustrated in Figure 5-8. Two 2-in.-thick steel plates and two 1-in.-thick rubber pads were used to distribute the load uniformly at the top and bottom as illustrated in Figure 5-8.

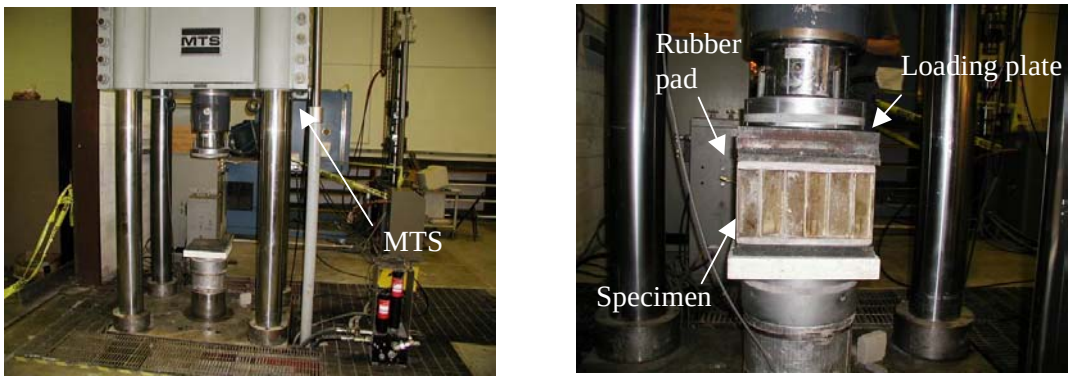

Figure 5-8 Crushing test setup

All the specimens failed in the same manner. The specimens emitted the first noise between 35 and 70 kips, and visual observation indicated that the core walls started to buckle between 120 and 130 kips. The crushing loads are shown in Table 5-2.

Table 5-2 Failure loads and stresses

	Failure Load (kips)	Actual Core Stress (ksi)	Nominal Core Stress (ksi)
Test 1 - 0.375	160	9.27	1.02
Test 2 - 0.375	164	9.48	1.05
Test 3 - 0.5	170	9.85	1.09
Test 4 - 0.5	155	8.98	0.99

The average crushing load was 162 kips with a standard deviation of 6.3 kips indicating a small scatter of results. Table 5-2 also shows the core crushing stresses calculated with equations (4.14) and (4.15). The average nominal and actual stresses at failure are 30% higher than those obtained by Lopez (2001). The specimens after failure are shown in Figure 5-9.

Test 1 – 0.375-in.-thick faces

Test 2 – 0.375-in.-thick faces

Test 3 – 0.5-in.-thick faces

Test 4 – 0.5-in.-thick faces

Figure 5-9 Crushing failure

5.6 Beam Test Results

5.6.1 Beams with Face Thickness of 0.375 inch

Test 1

Figure 5-10 shows the load-deflection curve for Test 1. The deflection was measured with the LVDT placed at midspan. At 20, 30, and 40 kips, the specimen was unloaded to evaluate the behavior in the unloading phase. Then, the specimen was loaded until failure. The figure indicates that the behavior is linear elastic up to failure during loading and unloading. The maximum vertical deflection recorded at midspan was 0.74 in. at a failure load of 103 kips. Figure 5-11 shows the data obtained from the strain gage labeled sg1, glued on the lower face surface at the middle of the beam. The maximum tensile strain recorded was 0.008601 at about 103 kips. The reading of the gage confirms a linearly elastic behavior up to failure.

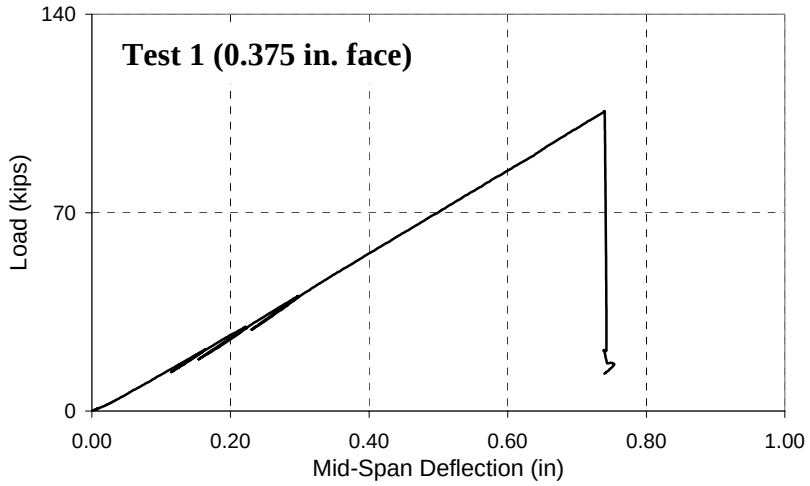

Figure 5-10 Load-deflection curve for Test 1

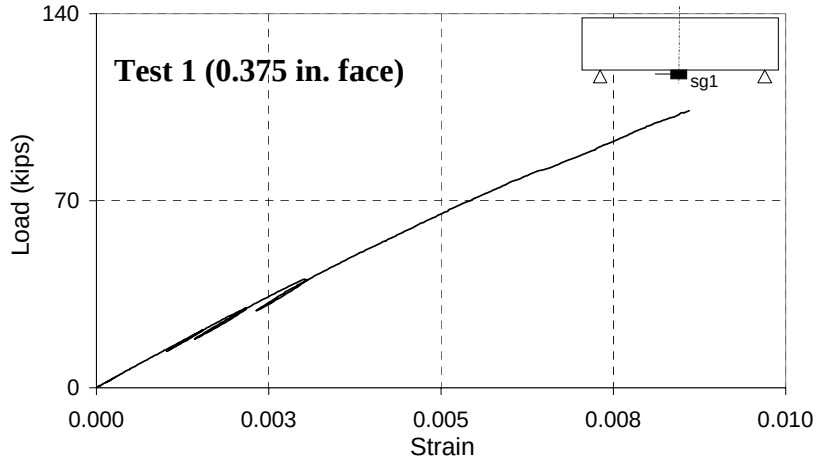

Figure 5-11 Load-strain curve for Test 1 (gage sg1)

Figure 5-12 shows the data obtained from the strain gage labeled sg3, glued on the side near the top face at the middle of the beam. In this case, the maximum compressive strain recorded at 103 kips was -0.007426. Considering that the gage was glued at 0.68 in. from the top surface, the calculated maximum compressive strain on the upper surface was -0.00912 using the plane-section assumption. This value agrees well with the maximum tensile strain recorded at the bottom face.

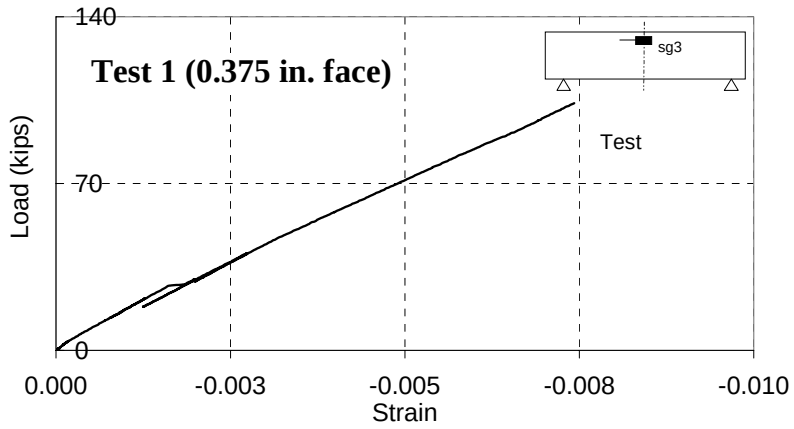

Figure 5-12 Load-strain curve for Test 1 (gage sg3)

Figure 5-13 shows the data obtained from the strain gage labeled sg4 placed 7.5 in. from the midspan on the top face. As expected, the strain recorded was smaller than the strain recorded at the middle of the beam. Figure 5-14 shows the load-strain curve from the strain gage (sg5) glued on the bottom surface and placed at about 7.5 in. from the midspan. The strain recorded at about 103 kips was 0.008412, which was considerably higher than the maximum compressive strain of -0.005437 recorded by the gage at the same location but on the upper face of the beam. The stress-strain curve also indicates a highly nonlinear behavior near the peak load.

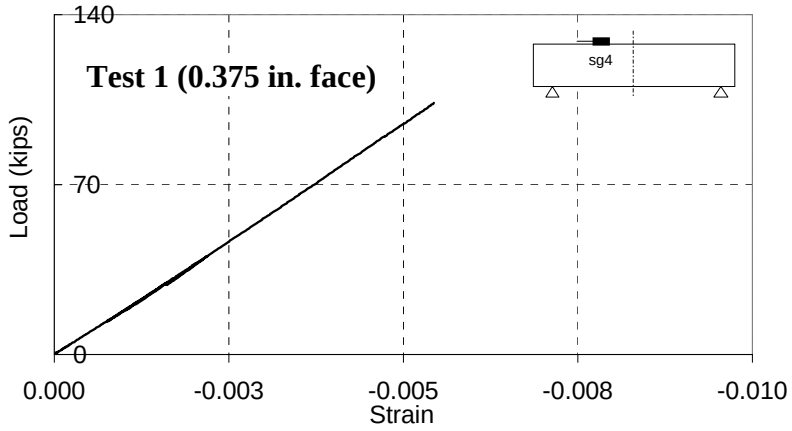

Figure 5-13 Load-strain curve for Test 1 (gage sg4)

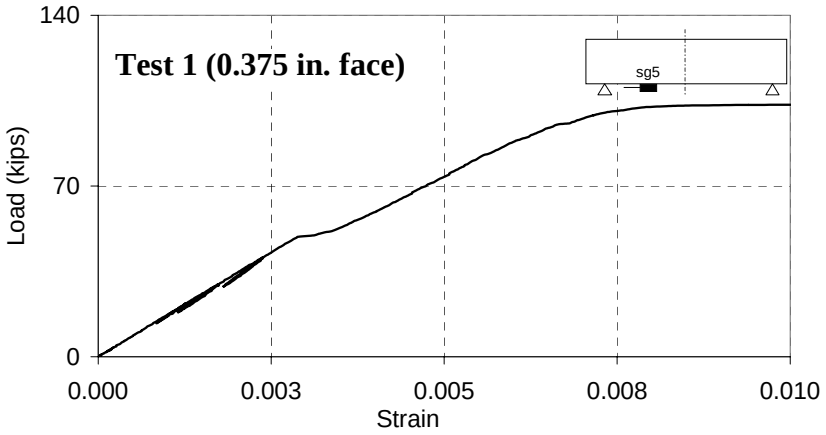

Figure 5-14 Load-strain curve for Test 1 (gage sg5)

The strain profiles at midspan shown in Figure 5-15 indicate that plane sections remained plane during bending. Figure 5-15 shows that the neutral axis shifted down right after reaching the 103-kip load indicating the delamination of the top face from the core.

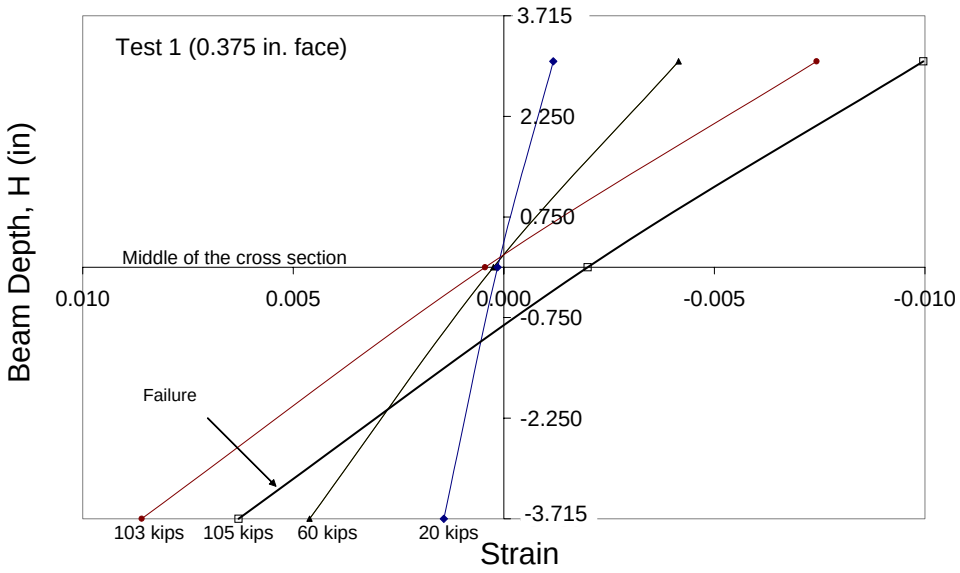

Figure 5-15 Strain profiles at different loading stages for Test 1 (midspan)

During the test, several types of damage occurred. At about 25 kips, a first noise was heard indicating that some fibers were breaking. In fact, the load-strain curve from strain gage sg3 exhibits some nonlinearity at about 27 kips as shown in Figure 5-12. Throughout the rest of the test, noises were heard indicating that fibers were probably breaking continuously during loading. Inspection of the beam after failure showed the presence of loose fibers. Finally, at a load of 103 kips, the top face started delaminating. The failure was brittle and released a large amount of energy. Debonding between the core and the upper face started under the load and propagated outward along the top core-face interface as shown in Figure 5-16. After that, the top face debonded. The core was subsequently subjected to a larger load which caused the local buckling of the core at both sides of the beam as illustrated in Figure 5-17. After failure, the top face and the core were completely detached as shown in Figure 5-18.

Figure 5-16 Failure mode in Test 1 – side view

Figure 5-17 Local buckling of the core in Test 1

Figure 5-18 Failure mode in Test 1 – end view

Test 2

The load-deflection curve for Test 2 is shown in Figure 5-19. The figure indicates that the behavior is linearly elastic until close to failure. The specimen failed at a load of about 76 kips.

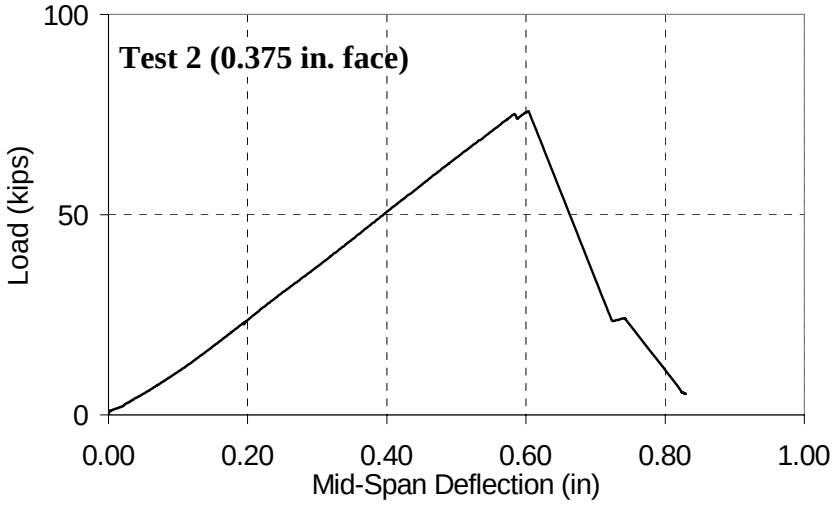

Figure 5-19 Load-deflection curve for Test 2

Figure 5-20 shows the data recorded by the strain gage labeled sg1, which was glued on the bottom face surface at the middle of the beam. The maximum tensile strain recorded was 0.006438 at about 76 kips.

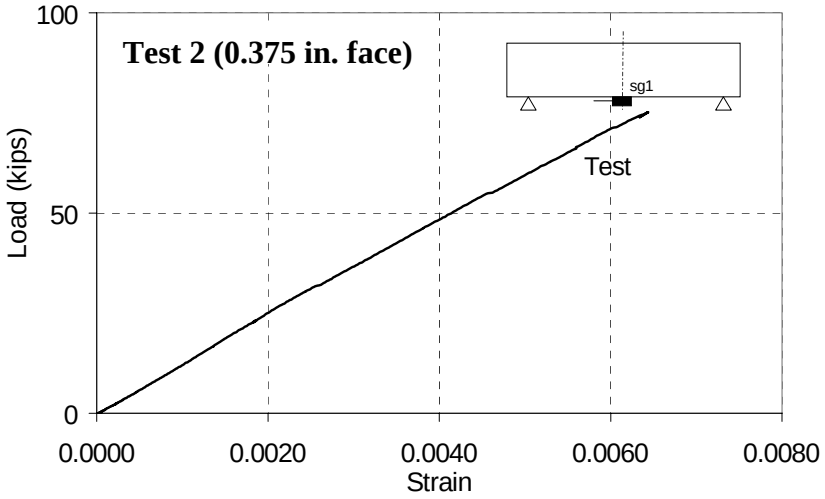

Figure 5-20 Load-strain curve for Test 2 (gage sg1)

Figure 5-21 shows the data obtained from the strain gage labeled sg2, glued on the side near the top face at the middle of the beam. The load-strain curve is not linear. The maximum compressive strain recorded at 76 kips was -0.004231, and the maximum compressive strain on the upper surface calculated from this value based on the plane section assumption is -0.006694, which is very similar to the maximum tensile strain recorded.

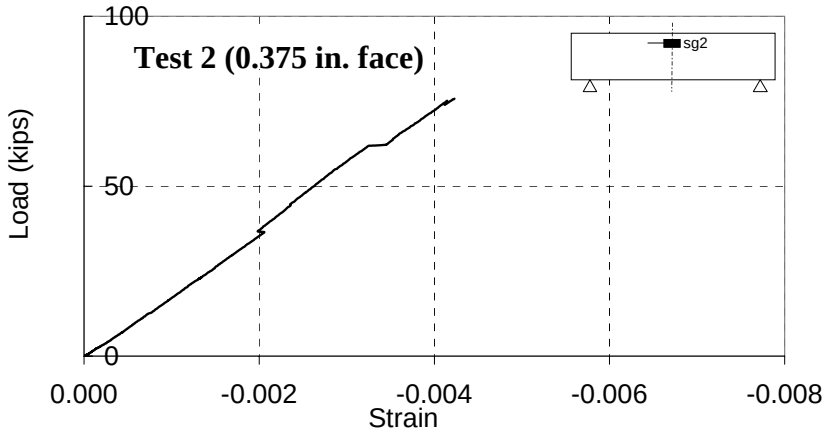

Figure 5-21 Load-strain curve for Test 2 (gage sg2)

Figure 5-22 shows the data obtained from the strain gage labeled sg3. Figure 5-23 and Figure 5-24 show the load-strain curves from the strain gages glued on the top and bottom surfaces, respectively. They were placed at about 7.5 in. from the midspan. The top ultimate strain recorded was -0.004403 while the maximum tensile strain at the bottom was 0.003135.

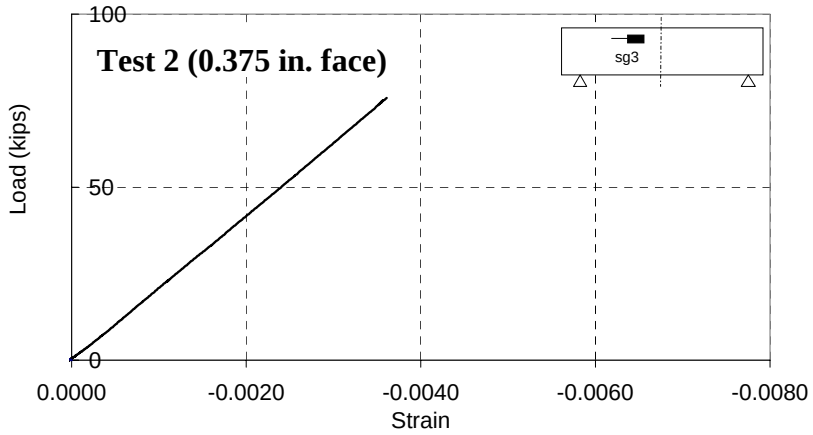

Figure 5-22 Load-strain curve for Test 2 (gage sg3)

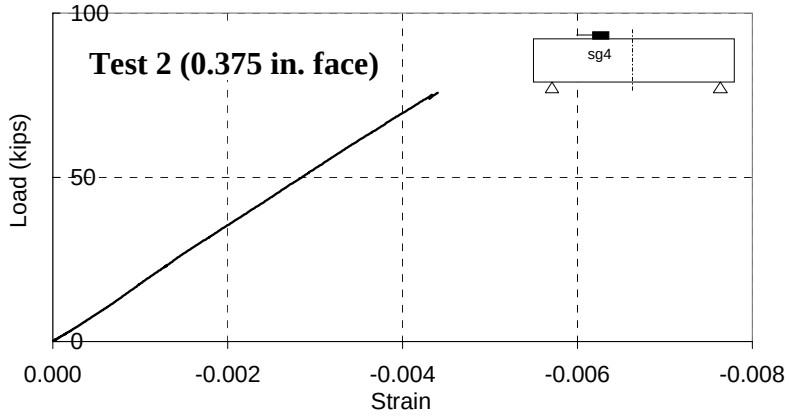

Figure 5-23 Load-strain curve for Test 2 (gage sg4)

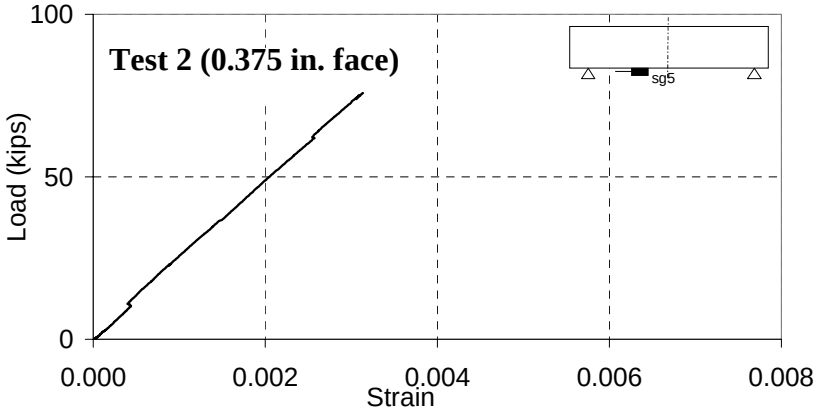

Figure 5-24 Load-strain curve for Test 2 (gage sg5)

Figure 5-25 shows that the load-strain curve from strain gage sg6 is linear elastic up to failure. Figure 5-26 shows the strain profiles at midspan. After failure at 76 kips, the neutral axis shifted down indicating that the upper face had delaminated.

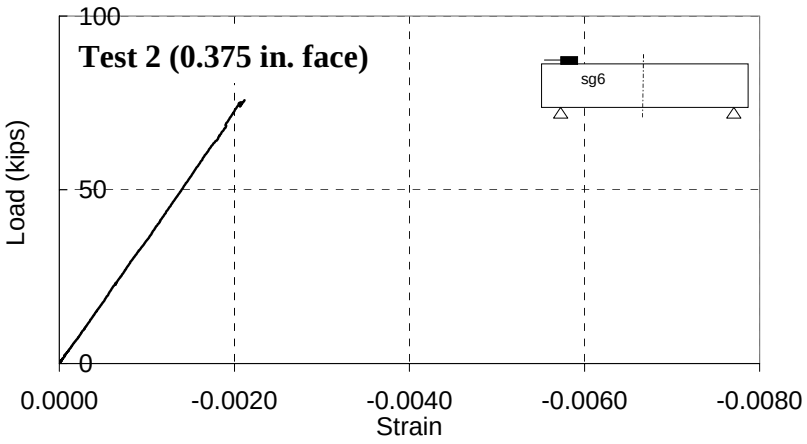

Figure 5-25 Load-strain curve for Test 2 (gage sg6)

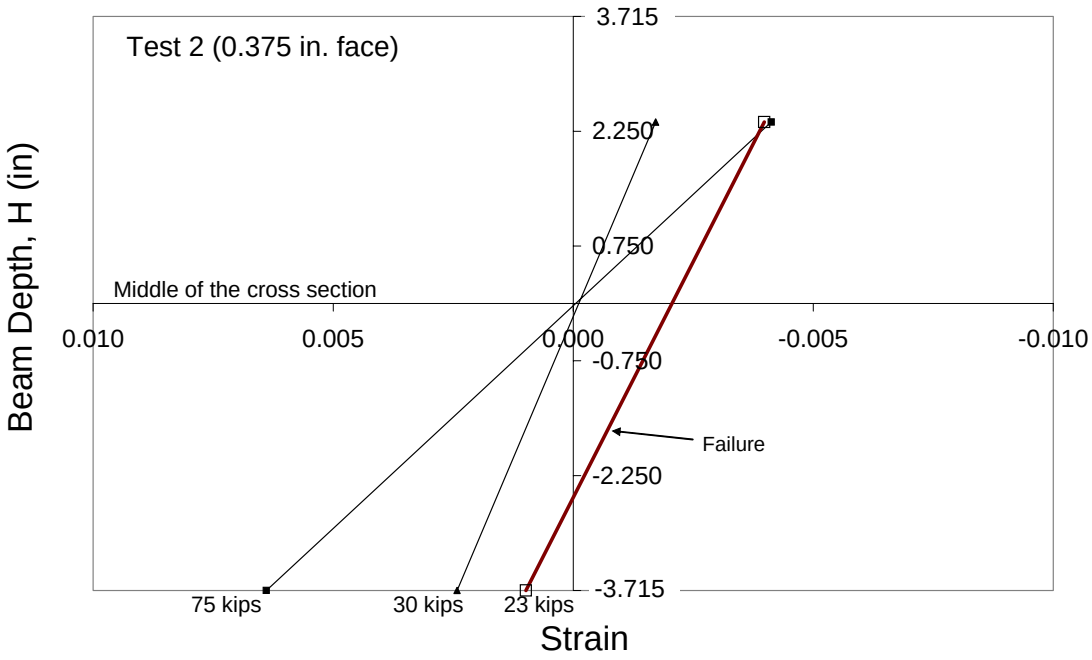

Figure 5-26 Strain profiles at different loading stages for Test 2 (midspan)

The failure in Test 2 was very similar to the failure reported in the first test. During the test, noises were heard indicating that some fibers were breaking during loading. At 75 kips, the load dropped slightly (Figure 5-19), probably because of a partial debonding between the top face and the core. Eventually, the partial debonding propagated and

triggered the brittle failure. At a load of 76 kips, the top face debonded. Debonding between the core and the upper face started under the load and propagated outward along the core-face interface as shown in Figure 5-27.

Figure 5-27 Failure mode in Test 2

As in the first test, the upper face was completely detached from the core as shown in Figure 5-28. The lost of composite action caused the core to carry more load, and consequently, the core buckled locally as shown in Figure 5-29.

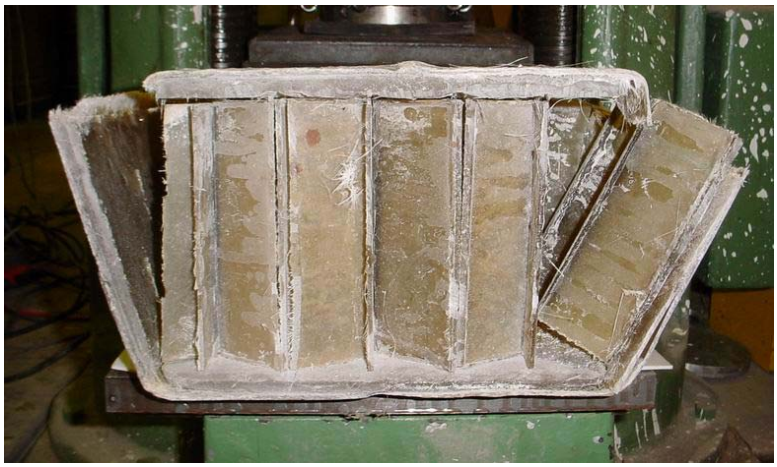

Figure 5-28 Debonding at top face-core interface in Test 2

Figure 5-29 Buckling of the core in Test 2

5.6.2 Beams with Face Thickness of 0.5 inch

Test 3

The load-displacement curve for Test 3 was linear up to about 23 kips as shown in Figure 5-30. At 23 kips and a deflection of 0.165 in, the upper face started debonding and the load-displacement curve became nonlinear. At 39, 47, and 50 kips, the load dropped suddenly indicating that the upper face continued to slip. This is well explained in Figure 5-31, which shows that, after the load dropped, the neutral axis at midspan shifted downward due to delamination of the top face. At 52 kips, the load dropped and the neutral axis shifted upward to the centroidal position, as shown in Figure 5-31, indicating that the bottom face slipped eventually causing the sudden failure of the beam.

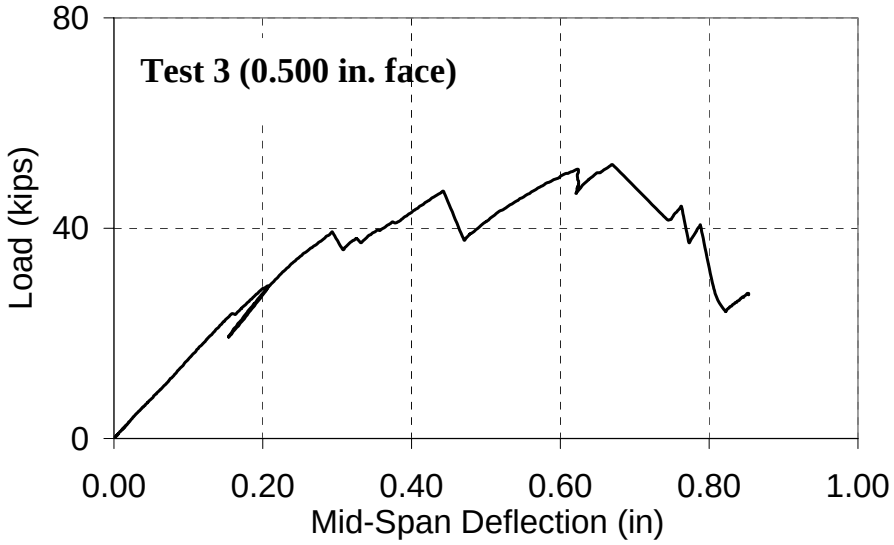

Figure 5-30 Load-deflection curve for Test 3

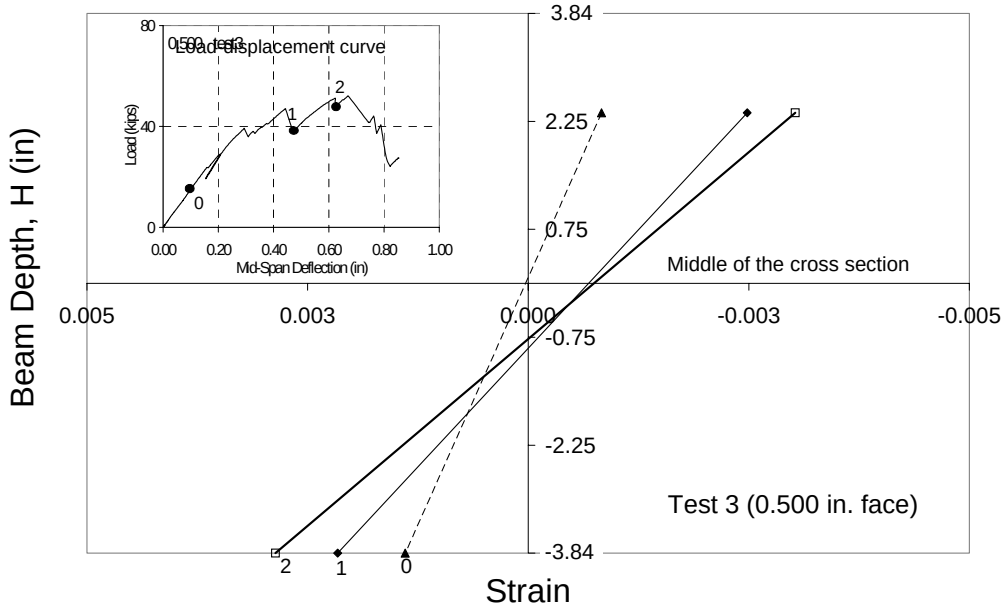

Figure 5-31 Strain profiles at different loading stages for Test 3 (midspan)

The reading from the strain gage placed at the middle of the beam on the bottom face indicated that the face-core system lost the full composite action at 40 kips. This can be deduced from the sudden stiffness change in the load-strain curve in Figure 5-32. The

strain reading from the strain gage located at the top is shown in Figure 5-33. Figure 5-34 and Figure 5-35 show the readings from the strain gages located at about 7.5 in. from the middle of the beam.

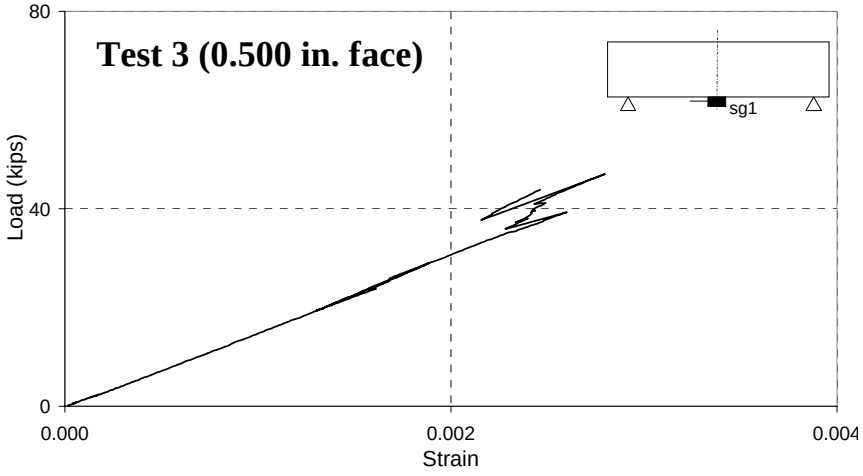

Figure 5-32 Load-strain curve for Test 3 (gage sg1)

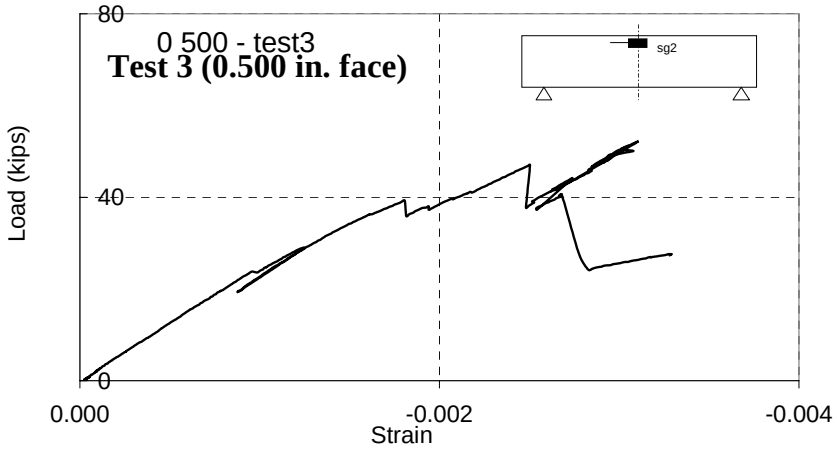

Figure 5-33 Load-strain curve for Test 3 (gage sg2)

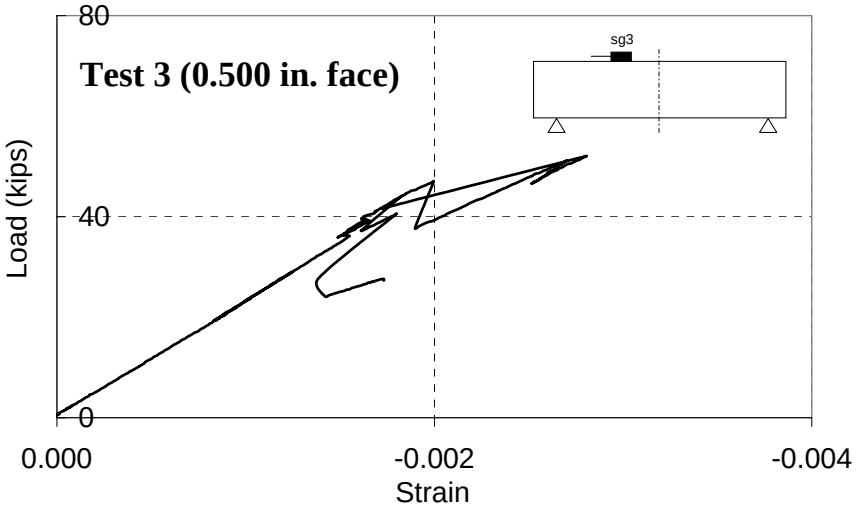

Figure 5-34 Load-strain curve for Test 3 (gage sg3)

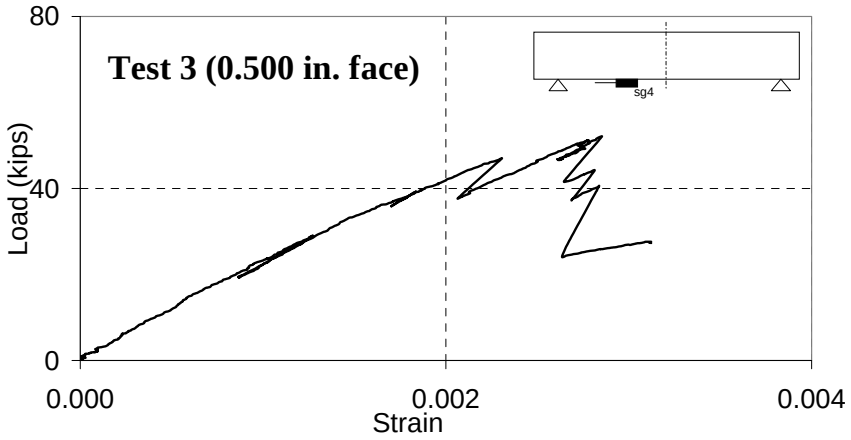

Figure 5-35 Load-strain curve for Test 3 (gage sg4)

Up to about 39 kips, the load-strain curves for gages sg3 and sg4 show a constant stiffness, as for the gages sg1 and sg2. At the section were these gages were located, the neutral axis did not change position up to the peak load as shown in Figure 5-36. This indicates that, in the beginning, the slip was localized at the middle and, later, it propagated toward the end of the beam.

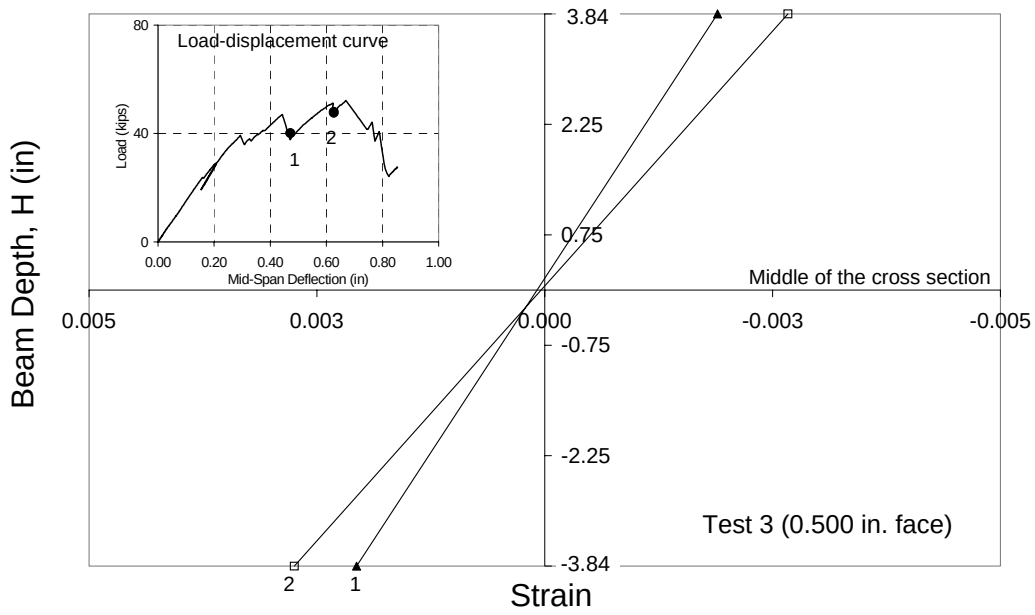

Figure 5-36 Strain profiles at different loading stages for Test 3 (sg3/sg4)

The failure observed in Test 3 was different from the failures reported in the previous tests. The beam failure was pseudo-ductile. The face debonded from the core progressively starting at 36 kips. The delamination started at the top of midspan and propagated toward the end of the beam. The top face did not debond uniformly and only the back side of the core buckled as shown in Figure 5-37.

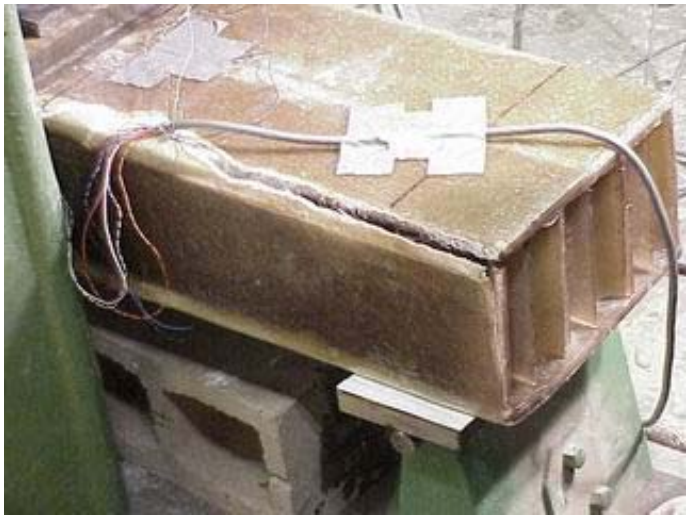

Figure 5-37 Failure mode in Test 3

This failure mechanism is probably due to workmanship in the manufacturing process. The bond between the top face and the core was not of uniform quality and this induced the premature debonding. This decreased the strength of the beam as compared to the two previous beams. After the test, visual inspection of the beam showed that one side of the face was completely debonded from the core.

Test 4

The load-displacement curve for Test 4 is perfectly linear up to 108 kips as shown in Figure 5-38. From 108 kips up to failure, the load-displacement curve becomes slightly nonlinear. The beam failed at 131 kips with a deflection of 0.76 in.

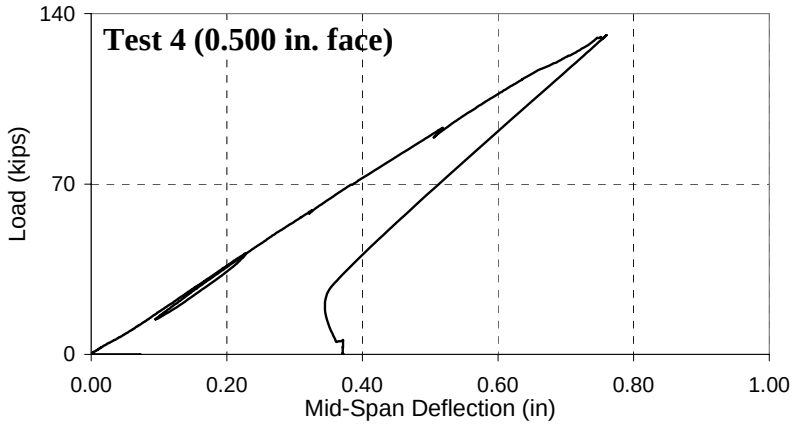

Figure 5-38 Load-deflection curve for Test 4

The strain gage located at midspan under the beam indicated that the response was linear elastic up to 108 kips as shown in Figure 5-39. The gage probably failed at a smaller load level than the beam. This may be due to gage malfunctioning or a localized failure (some fibers might have broken at this location).

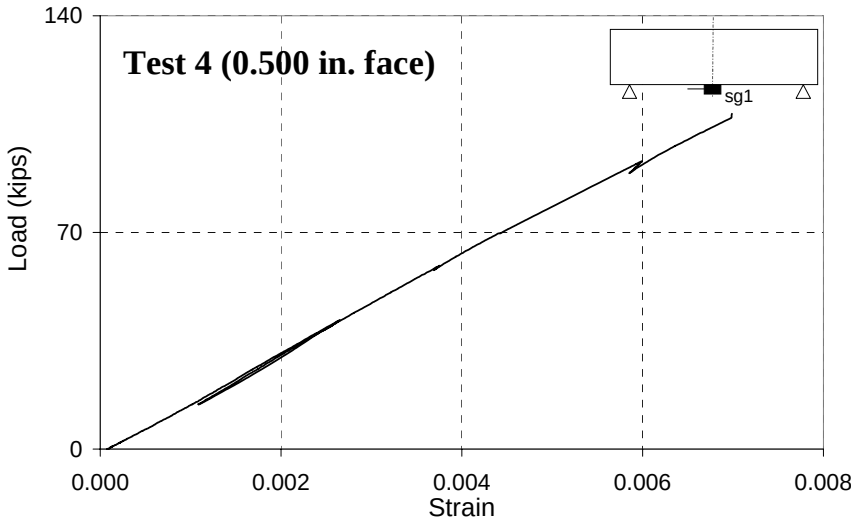

Figure 5-39 Load-strain curve for Test 4 (gage sg1)

The strain gage, sg2, glued at the middle to measure the maximum compressive strain as shown in Figure 5-5 did not work. However, at 3.54 in. from midspan, another strain gage, sg3, was glued on the side of the beam. It showed that the load-strain curve was linear up to 108 kips and then became slightly nonlinear. The top and bottom strain gages located at 7.5 in. from midspan showed a linearly elastic behavior until failure as shown in Figure 5-41 and Figure 5-42. Finally, Figure 5-43 shows that the strain gage, sg6, placed at 9.44 in. from midspan indicated a linearly elastic behavior up to failure.

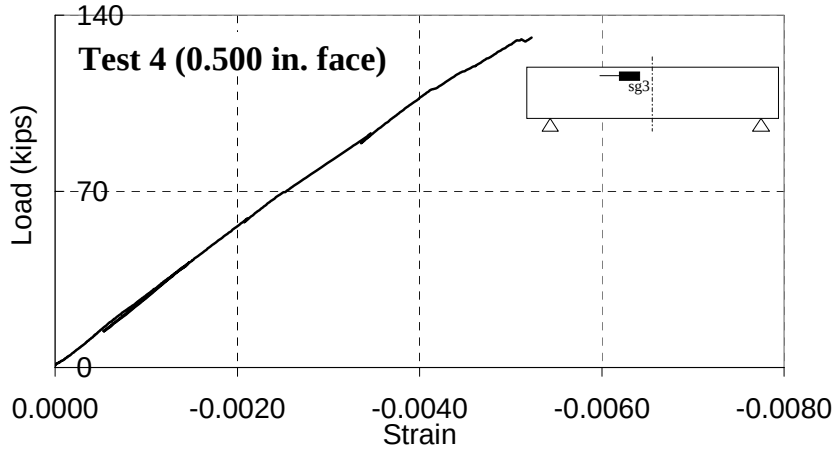

Figure 5-40 Load-strain behavior for Test 4 (gage sg3)

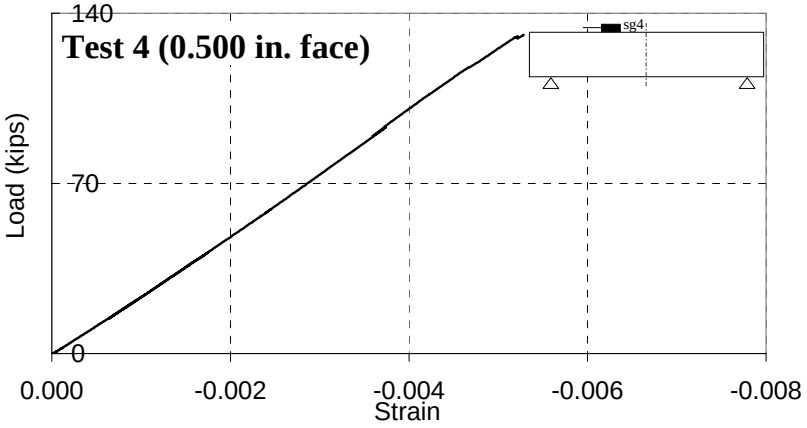

Figure 5-41 Load-strain behavior for Test 4 (gage sg4)

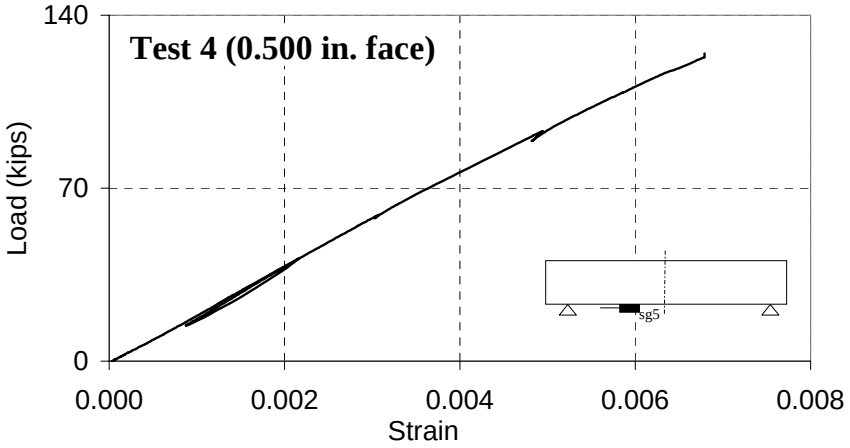

Figure 5-42 Load-strain behavior for Test 4 (gage sg5)

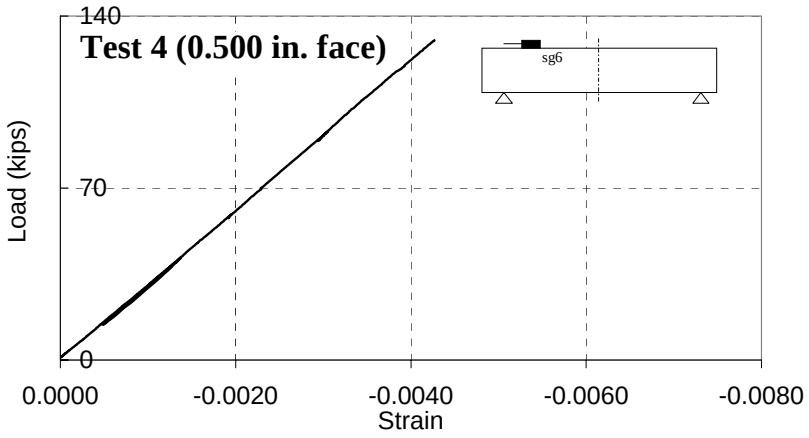

Figure 5-43 Load-strain behavior for Test 4 (gage sg6)

In Test 4, the first sound was registered at 20 kips, and noises were heard constantly thereafter at different loading stages indicating progressive damage (broken fibers). The load-displacement response was linearly elastic up to 108 kips. At about 108 kips, the top face started to debond from the core under the loading plate. The load-strain curve collected by sg1, located at midspan, became nonlinear at this load stage, while sg4 and sg6, located at 7.08 in. and 9.44 in. from midspan, respectively, did not register any stiffness change. The debonding process propagated from midspan toward the end of the beam eventually causing failure at 131 kips. After failure, both sides of the core buckled as shown in Figure 5-44. After failure, the top face was completely detached from the core as shown in Figure 5-45.

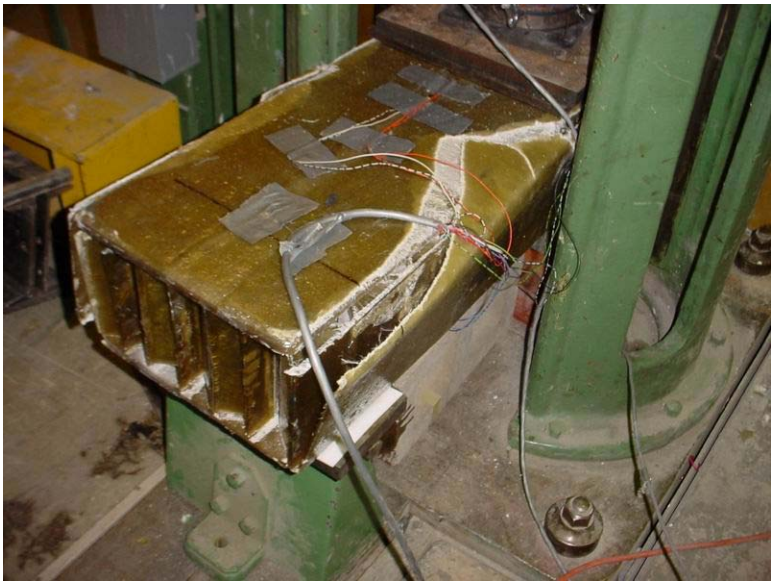

Figure 5-44 Failure mode in Test 4

Figure 5-45 Debonding at the face-core interface in Test 4

5.7 Summary of Test Results

Table 5-3 summarizes the results of the bending tests. The recorded failure loads were between 39 and 131 kips. This big scatter was mainly due to the bonding quality of

the face-core interface.

Table 5-3 Summary of test results

Test	Moment of Inertia *in⁴*	Failure load *kips*	Max displ. (δ) *in*	L/δ	Failure Mode	Max top strain at midspan *x1000*
1 - 0.375 in.	155	103	0.71	69	1	-8.1822
2 - 0.375 in.	143	76	0.60	80	1	-6.0838
3 - 0.5 in.	201	39	0.29	167	2	-2.4924
4 - 0.5 in.	201	131	0.76	64	1	-7.0055

In Table 5-3, the maximum top strain in Test 4 was recorded 3.54 in. from midspan (gage sg3), L is the beam span, and δ is the maximum displacement. The maximum strain at the top of the beam is calculated with the gage readings taken along the depth of the beams based on the plane-section assumption. Failure mode 1 represents a linearly elastic behavior till failure, and failure mode 2 represents a pseudo-ductile behavior with progressive damage.

Figure 5-46 shows the load-displacement curves for the four tests. The figure shows that the face thickness influenced the stiffness of the beams as reflected by their moment of inertia shown in Table 5-3.

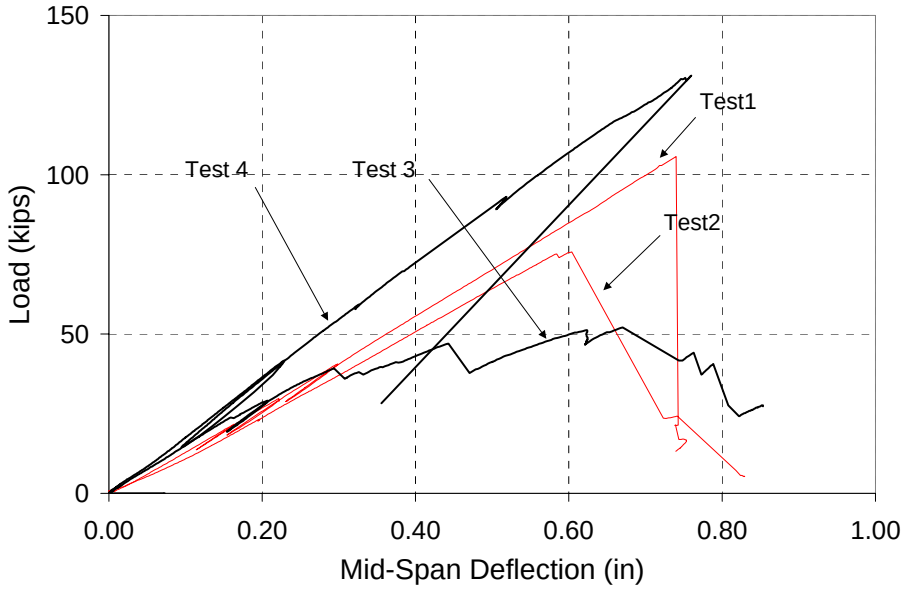

Figure 5-46 Load-displacement curves for the four tests

Section 600 of the City and County of Denver provisions requires that the midspan deflection shall not exceed 1/500 of the clear span for a one-foot-wide beam subjected to a 10-kip load. The span length, *L*, is 48.5 in. Therefore, *L/500=0.097* in. For Test 1, the midspan deflection at 10 kips was 0.080 in. For Tests 2, 3, and 4, they were 0.093, 0.068, and 0.060 in., respectively. However, it should be mentioned that the beams in Test 1, Test 3, and Test 4 were 13-in. wide. The midspan deflection is directly proportional to the moment of inertia of the beams. A 12-in.-wide beam deflects about 8% more than a 13-in.-wide beam. For Tests 1, 3, and 4, the adjusted deflections for a one-foot-wide beam are 0.087, 0.074, and 0.065 in., respectively. Therefore, the beams satisfied the deflection requirement.

The Ultimate Crushing Capacity, P_C, is calculated by assuming a tire contact area of 380 in.^{2} (AASHTO 1998) and using the crushing test results presented in Table 5-2.

Table 5-4 indicates that 45% of the ultimate crushing capacity is much higher than the Factored Load of 56.5 kips.

Table 5-4 Ultimate Crushing Capacity

	45% P_C (kips)
Test 1 - 0.375	175
Test 2 - 0.375	179
Test 3 - 0.5	186
Test 4 - 0.5	170

The interface shear stress at failure, τ_{ult}, is calculated using equation (4.20) and the Ultimate Shear Load Capacity, P_S, for a bridge panel is calculated from τ_{ult} of each beam by assuming an effective width of 7 feet. Table 5-5 presents the results. As shown, 45% of the Ultimate Shear Load Capacity is well above the maximum Factored Load of 56. 5 kips. Hence, the tests indicate that the panel sections satisfied the shear design requirement.

Table 5-5 Tested Ultimate Shear Capacity

	Failure Load (kips)	τ_{ult} (ksi)	45% P_S (kips)
Test 1 - 0.375	103	0.41	300
Test 2 - 0.375	76	0.33	240
Test 3 - 0.5	39	0.16	118
Test 4 - 0.5	131	0.54	398

The factor of safety against failure, P_U/P, can be calculated with the P_S and P_C values shown in

Table 5-4 and Table 5-5. For all the beams tested, the flexural load capacity P_F is not a dominating factor and is therefore not considered here. Hence, P_U is the ultimate load capacity that is the smaller of P_S and P_C, and P is the service load of 26 kips. The shear capacity, P_S, of the beam in Test 3 provides the minimum P_U, which leads to a factor of safety of 11. This factor of safety is two times the value shown in Table 4-1 because of the shear strengthening introduced into the test beams.

6 BEAM ANALYSES

6.1 Introduction

The Timoshenko beam theory and the finite element method are used to analyze the behavior of the beams that were tested. The following sections give a description of the analysis models used and the comparison of the theoretical results with experimental data.

6.2 Timoshenko Beam Theory

Because of the low span-to-depth ratio of the test beams, the Timoshenko beam theory is utilized to analyze the beam response. Perfect bond is assumed between the core and the faces, and FRP is considered a linearly elastic material up to failure. The loading plate is assumed to distribute the pressure uniformly as shown in Figure 6-1.

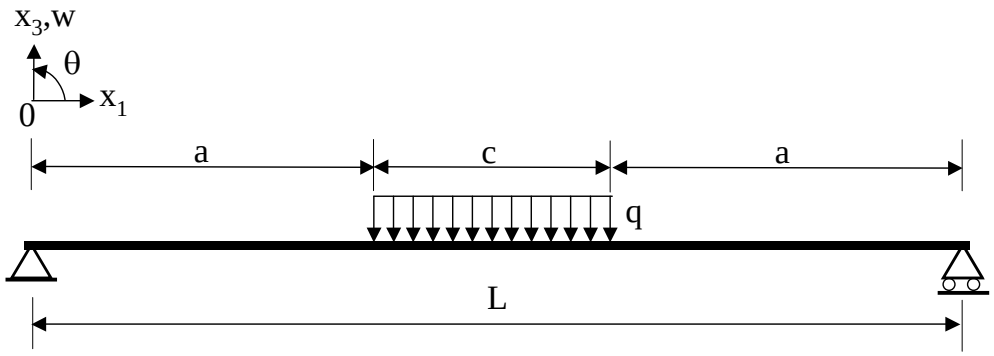

Figure 6-1 Schematic of the beam analysis

By including the effect of the shear deformation, the differential equation for beam deflection is given as:

$$\frac{d^2w}{dx_1^2} = -\frac{1}{E_{f11}I_2}\left(M(x_1) + \frac{E_{f11}I_2}{\kappa A G_{c13}} q(x_1)\right) \tag{6.1}$$

where E_{f11} is the modulus of elasticity of the face in the x_1 direction, $q(x_1)$ is the load applied per unit length of the beam, G_{c13} is the shear modulus of the core in the x_1-x_3 plane, κ is the shear correction factor, and A is the shear area. In this analysis, κ is assumed to be 1.0 and A excludes the cross-sectional area of the face, i.e., $A=bh$ (Figure 4-3). By integrating equation (6.1), we have:

$$w(x_1) = \frac{qc}{12E_{f11}I_2}x_1^3 + C_1x_1 + C_2 \quad \text{for} \quad 0 < x_1 < a \tag{6.2}$$

$$w(x_1) = -\frac{q}{24E_{f11}I_2}x_1^4 + \frac{(2a+c)q}{12E_{f11}I_2}x_1^3 + \frac{(2E_{f11}I_2 - a^2G_{c13}A)q}{3E_{f11}I_2}x_1^2 + C_3x_1 + C_4$$

$$\text{for} \quad a < x_1 < L/2$$

where $a=(L-c)/2$.

Finally, by applying the boundary conditions, it is possible to solve for the constants C_1, C_2, C_3 and C_4:

$$C_1 = -\frac{qc}{2G_{13}A} - \frac{qc}{24E_{f11}I_2}(6a^2 + 6ca + c^2) \tag{6.3}$$

$$C_2 = 0$$

$$C_3 = -\frac{q(2a+c)}{2G_{13}A} - \frac{q(2a+c)}{24E_{f11}I_2}(-2a^2 + 4ca + c^2)$$

$$C_4 = \frac{qa^2}{2G_{13}A} - \frac{qa^4}{24E_{f11}I_2}$$

Once $w(x_1)$ is known, $M(x_1)$ and, therefore, the strain and stress can be calculated as follows:

$$M(x_1) = -\frac{d^2w(x_1)}{dx_1^2}E_{f11}I_2 \tag{6.4}$$

$$\varepsilon(x_1, y) = \frac{d^2w(x_1)}{dx_1^2}y \tag{6.5}$$

$$\sigma(x_1, y) = E_{f11}\varepsilon(x_1, y) \tag{6.6}$$

In equations (6.5) and (6.6), y represents the distance between the neutral axis of bending and the point at which the strain and stress are calculated. In the analytical solution, the

strains and stresses are calculated by assuming that the plane sections remain plane during bending.

6.3 Elastic Finite Element Analyses

Finite element (FE) analyses are performed with a 2D mesh using the program Merlin (MERLIN II User's and Theory Manuals 2002). The 2D model is discretized using 3-node triangular plane-stress elements. The FRP is characterized by a linearly elastic orthotropic material model. The material properties used for the model are the homogenized face and core material stiffness properties shown in Table 3-2.

Figure 6-2 shows the boundary conditions and the mesh used in the analyses. To model the tests closely, two steel plates, which are free to rotate, are introduced at the supports. The plate used to load the beam in the test is modeled by applying a uniform traction as shown in Figure 6-2.

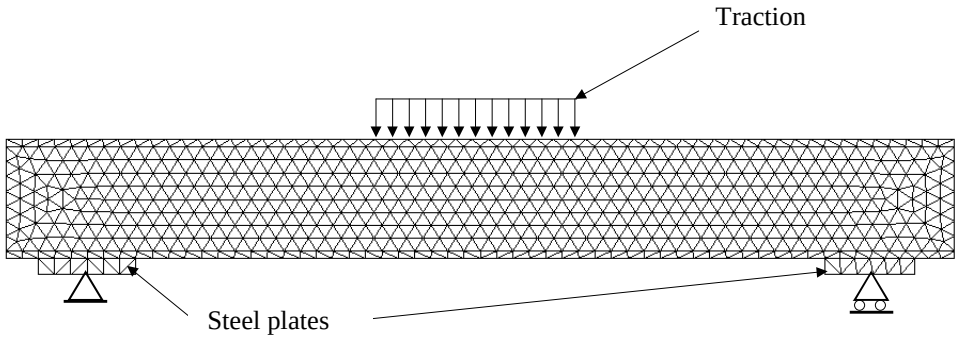

Figure 6-2 Finite element model of the test beams

6.4 Results of Elastic Analyses

6.4.1 Analytical Results from Timoshenko Beam Theory

Figure 6-3 through Figure 6-6 compare the experimental and analytical load-displacement curves for all the four tests. By comparing the results from the Timoshenko

beam theory and the Eurler-Bernoulli beam theory, as shown in the figures, we can observe that shear deformation is not negligible. The influence of the shear strengthening, shown in Figure 5-1, on the bending capacity is considered in the analytical model by assuming an additional mat thickness of 0.09 in. on each face of a beam. In general, the analytical solutions from the Timoshenko beam theory agree with the experimental response well until debonding occurs. Because of initial support settlements in the test setup, the experimental load-displacement curves are initially slightly softer than the calculated ones. Except for Test 4, the analytical load-displacement curves trace the experimental load-displacement curves well. When the faces started to debond, the experimental response changed from linearly elastic to nonlinear; this behavior cannot be captured with the linearly elastic model used here. For Test 4, the experimental result somehow shows a stiffer behavior than the analytical result.

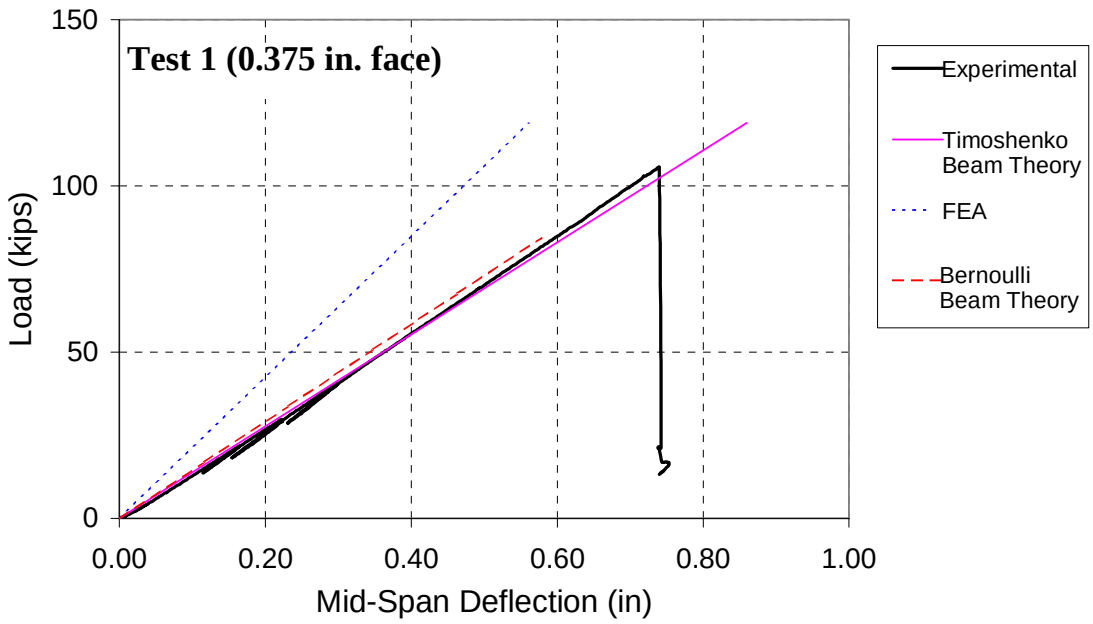

Figure 6-3 Comparison of load-displacement curves from analytical and FE models with experimental results for Test 1

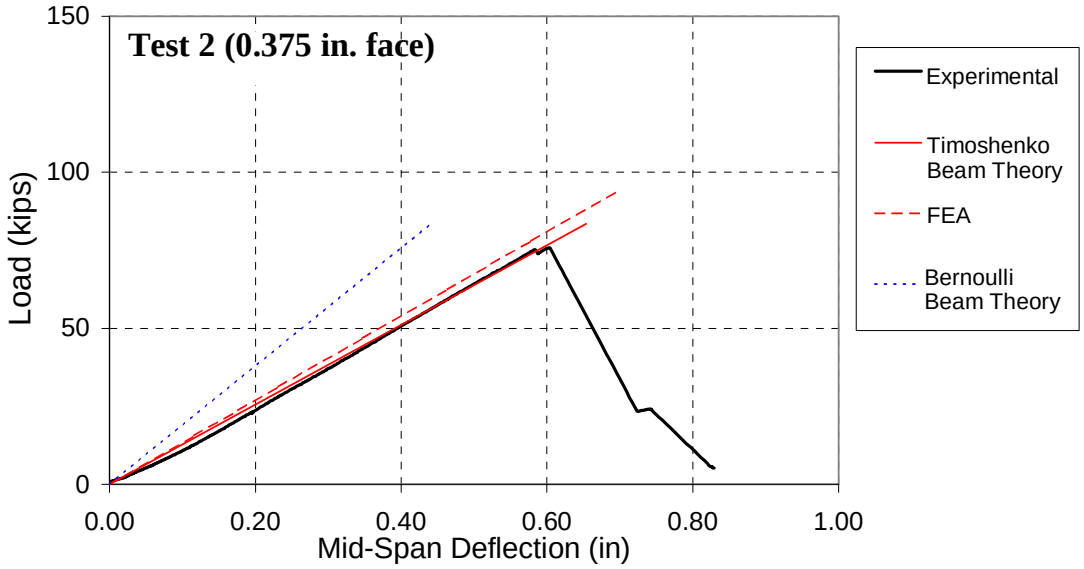

Figure 6-4 Comparison of load-displacement curves from analytical and FE models with experimental results for Test 2

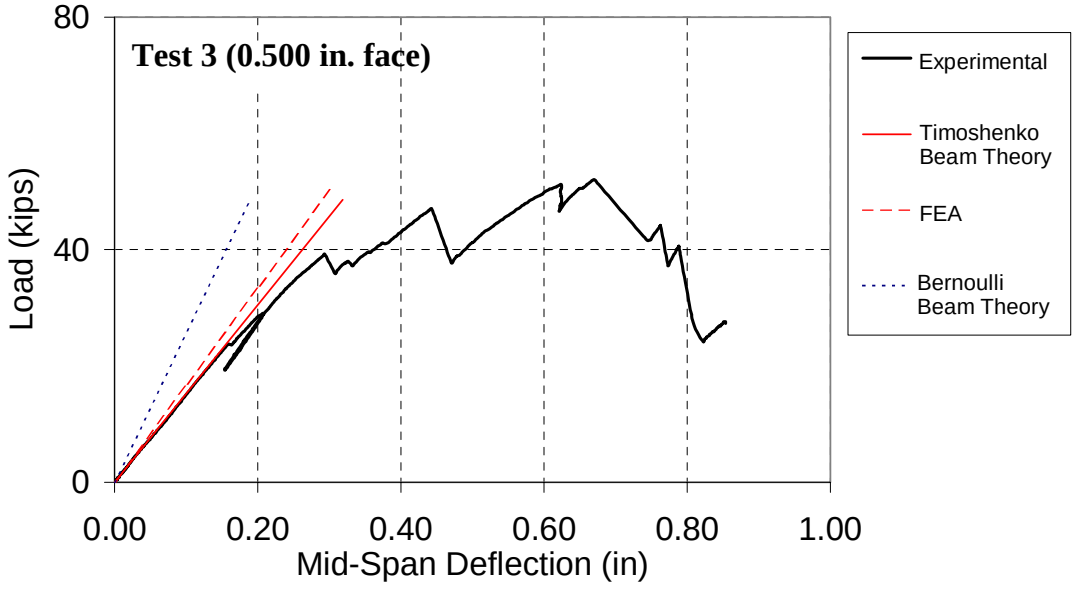

Figure 6-5 Comparison of load-displacement curves from analytical and FE models with experimental results for Test 3

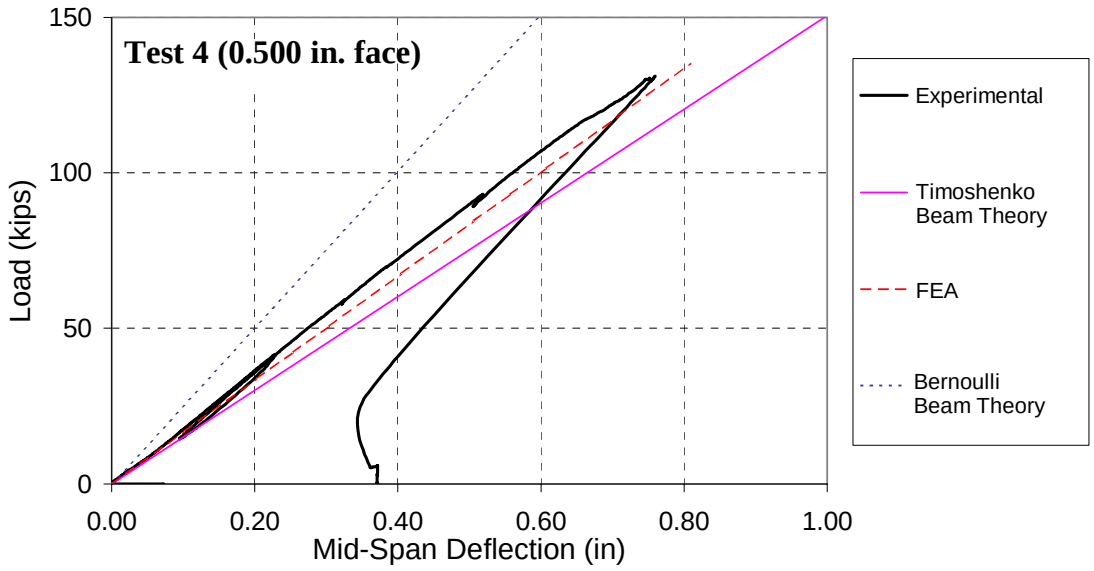

Figure 6-6 Comparison of load-displacement curves from analytical and FE models with experimental results for Test 4

Figure 6-7 through Figure 6-14 compare the bottom strain values obtained from the beam theory and the tests at midspan and at 7.5 in. from midspan. For all the four tests, the analytical load-strain curves are slightly softer than the experimental ones because of two possible reasons. First, in the analytical solution, the dimensions of the supports are not considered. Second, the beam theory assumes a uni-axial stress state, while, in reality, a beam is subjected to multi-axial stresses.

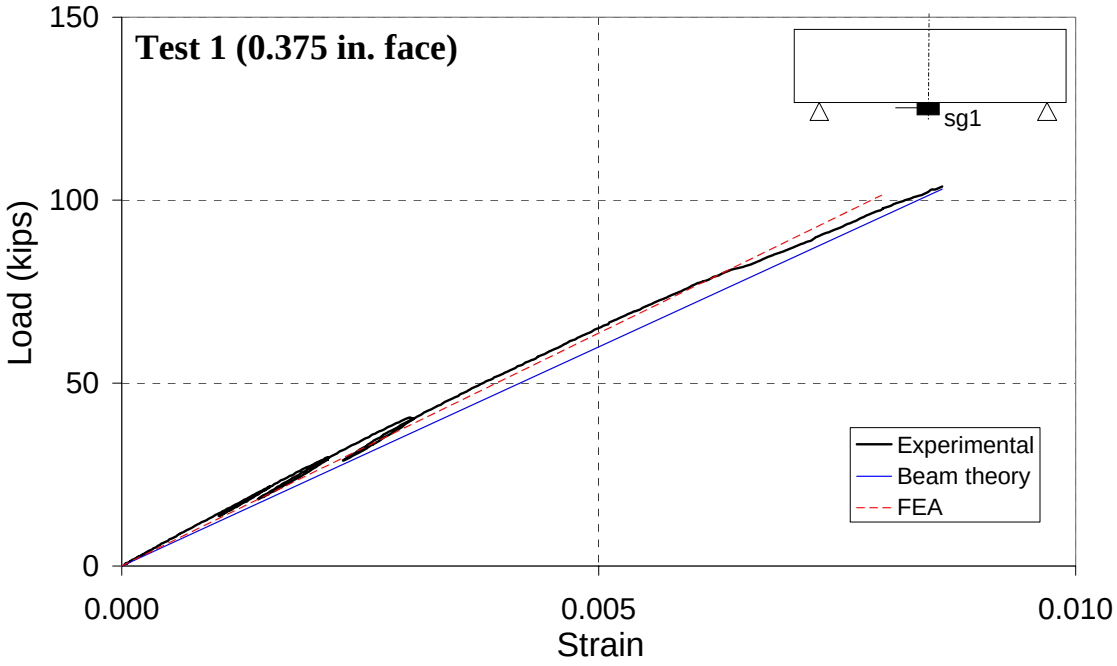

Figure 6-7 Analytical and numerical load-strain curves for bottom strain at midspan for Test 1

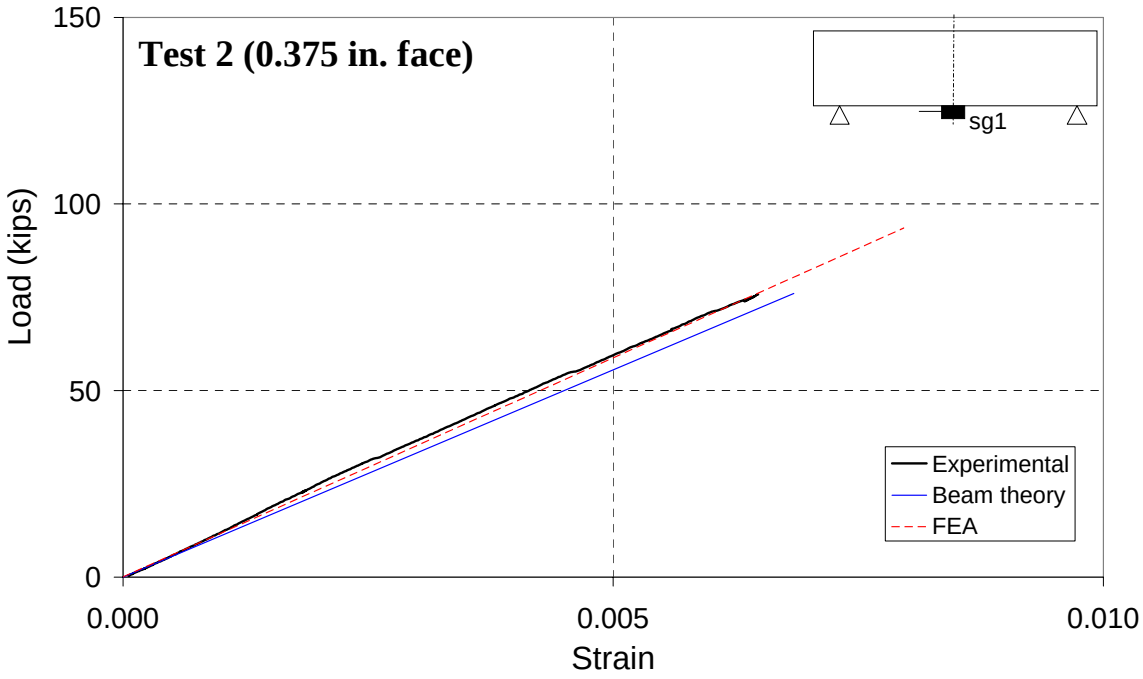

Figure 6-8 Analytical and numerical load-strain curves for bottom strain at midspan for Test 2

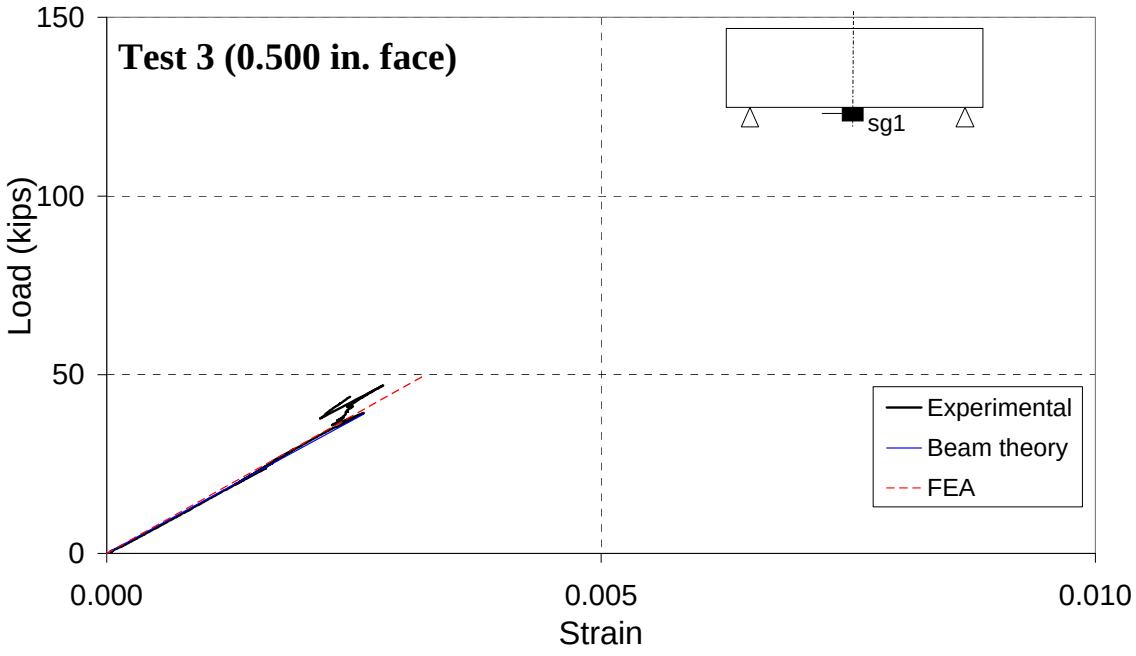

Figure 6-9 Analytical and numerical load-strain curves for bottom strain at midspan for Test 3

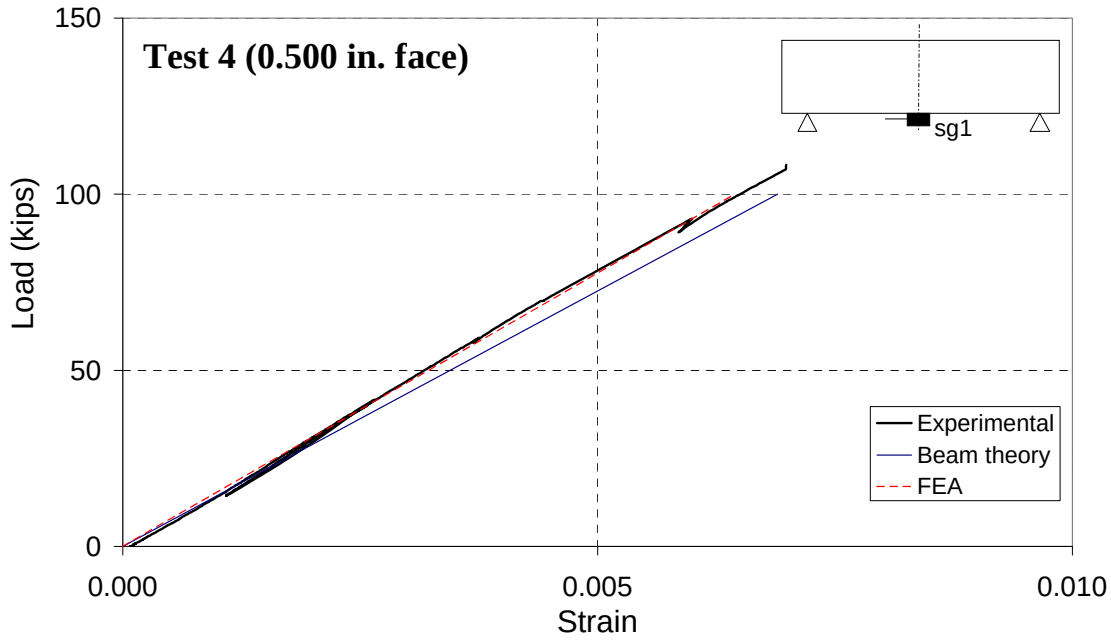

Figure 6-10 Analytical and numerical load-strain curves for bottom strain at midspan for Test 4

Figure 6-11 through Figure 6-14 compare the load-strain curves obtained from the analytical model and the tests for the bottom gage at 7.5 in. from midspan. Comparing Figure 6-11 with Figure 6-12, it is evident that the experimental load-strain curves from Test 1 and Test 2 are quite different. This is likely due to the malfunctioning of the gage in Test 2, which resulted in the experimental load-strain curve in Figure 6-12 much stiffer than the analytical result.

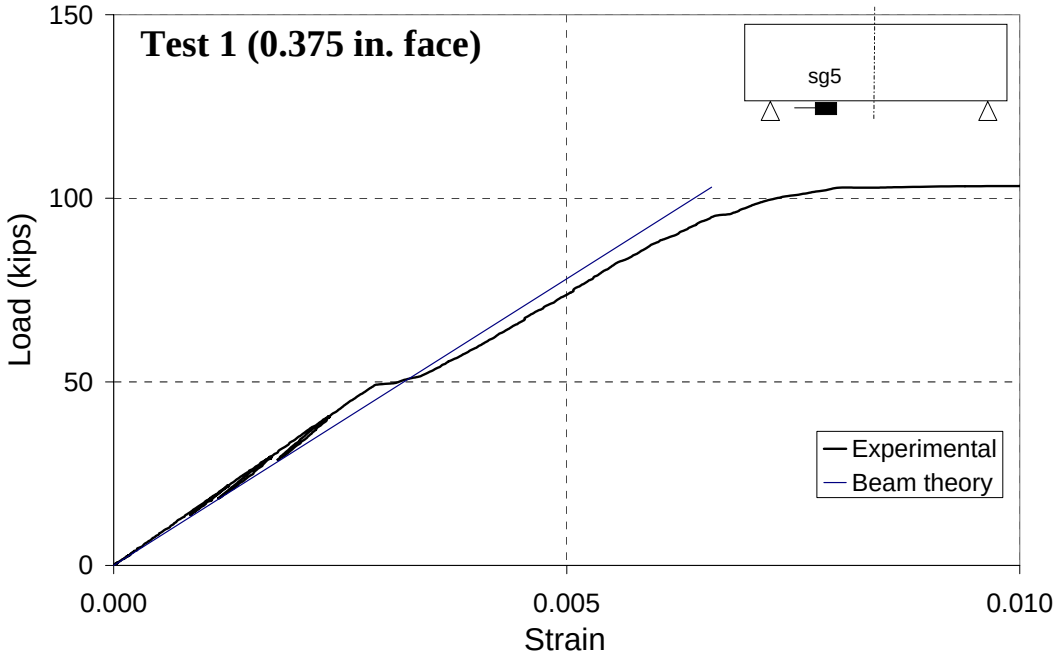

Figure 6-11 Analytical and numerical load-strain curves for bottom strain at 7.5 in. from midspan for Test 1

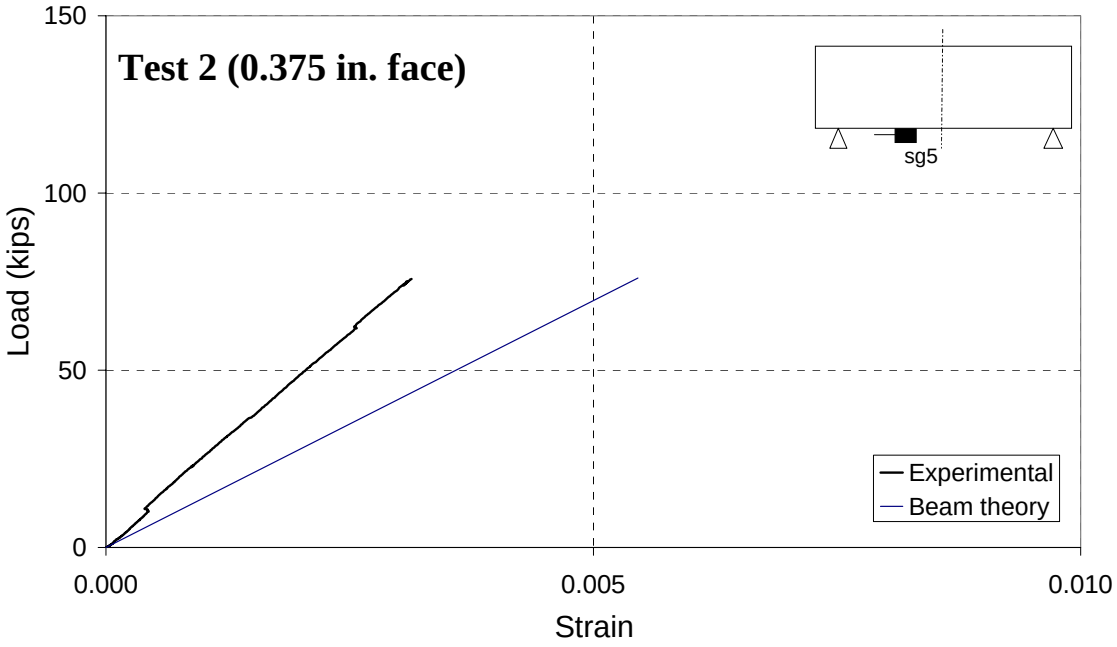

Figure 6-12 Analytical and numerical load-strain curves for bottom strain at 7.5 in. from midspan for Test 2

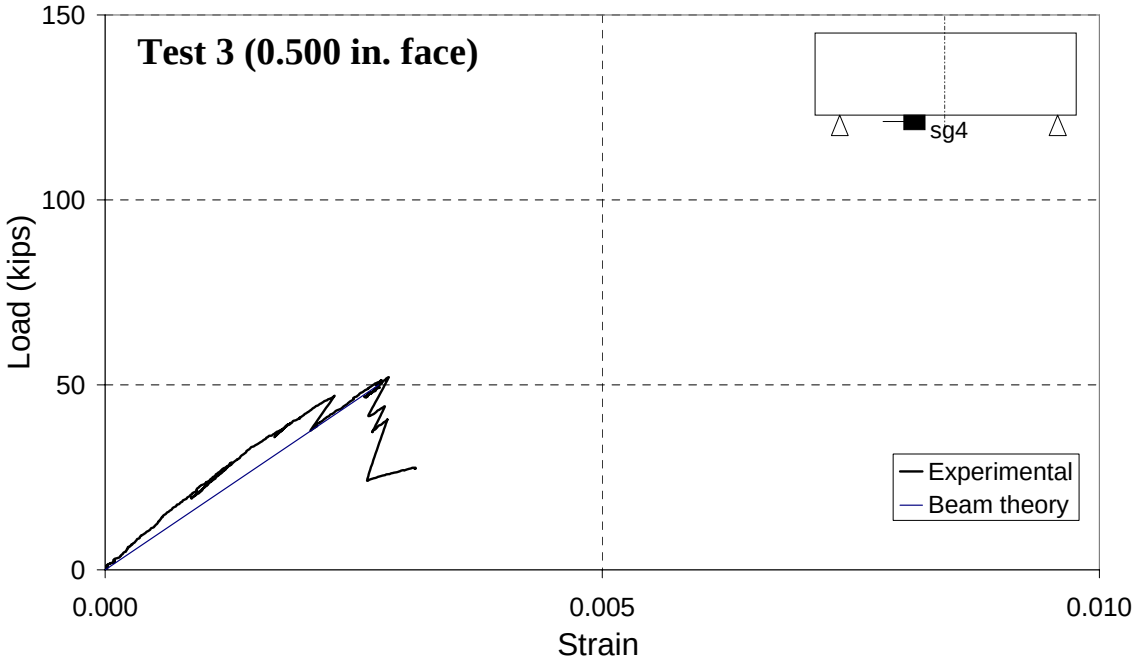

Figure 6-13 Analytical and numerical load-strain curves for bottom strain at 7.5 in. from midspan for Test 3

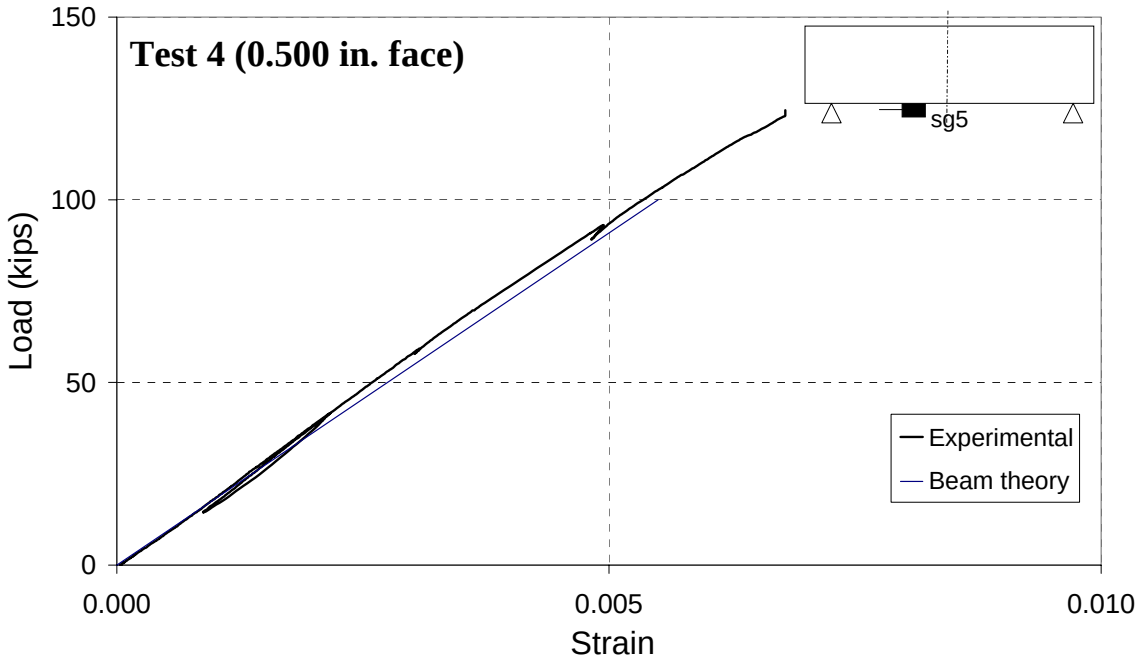

Figure 6-14 Analytical and numerical load-strain curves for bottom strain at 7.5 in. from midspan for Test 4

6.4.2 Numerical Results from Elastic Finite Element Analyses

All the results from the FE analyses are given as nodal values. Figure 6-3 through Figure 6-6 compare the experimental and FE load-displacement curves for all the four tests. The effect of the shear strengthening on the bending resistance is considered, as in the analytical model, by adding a thickness of 0.09 in. to each face. The numerical solutions agree with the experimental response well until debonding occurs. In the FE analyses, as in the Timoshenko beam model, the slip between the faces and the core is not considered.

Figure 6-7 through Figure 6-10 compare the strain values obtained at midspan from the FE analyses with the experimental results. For all four tests, the numerical results match the experimental data well. Unlike the Timoshenko beam theory, the FE analyses take into account the dimensions of the supports, and also provide a two-dimensional

stress state. For this reason, the FE model provides a better estimate of the beam stiffness than the beam theory.

The strain distribution along the top surface of the beam in Test 1 at the peak load of 103 kips is shown in Figure 6-15. The experimental value of the top strain at midspan is calculated by using the gage readings taken along the depth of the beam. As shown in the figure, the numerical results match the experimental data well. The discrepancy at the edge of the loading plate could be partially caused by the localized bending effect introduced by the stiff plate, which cannot be exactly captured with the assumption of a uniform traction. This could also be due to the small uncertainties in the exact location of the gages. However, the strain distribution at the peak load of 75 kips along the top face of the beam in Test 2 is well predicted as shown in Figure 6-16.

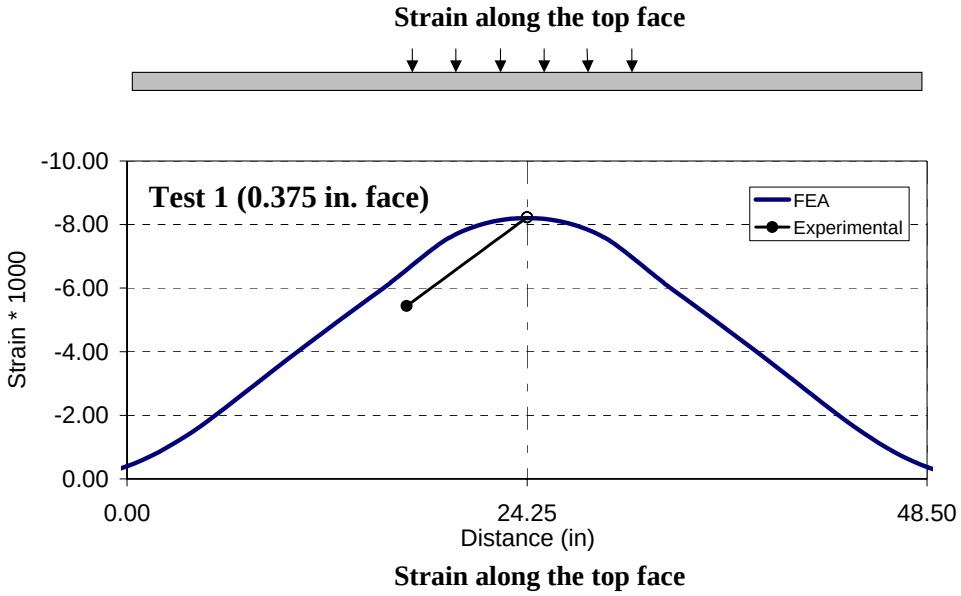

Figure 6-15 Strain distribution along the top face of the beam in Test 1

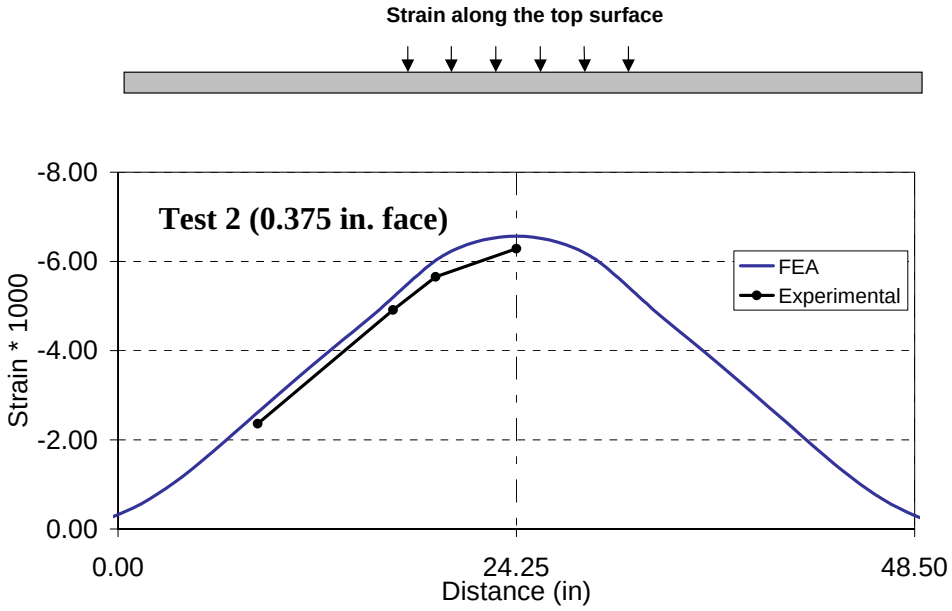

Figure 6-16 Strain distribution along the top face of the beam in Test 2

In the third test, the face debonded early as the load increased. The face started to debond at 23 kips. Below this load level, the FE analysis agrees with the experiment well as shown for a load of 16 kips in Figure 6-17. This was a stage when the beam was still acting as a full composite. After delamination, the difference between the FE analysis and test results increases as shown for a load of 48 kips in Figure 6-17. This is due to the loss of the composite action. The experimental strain in the face is smaller than the calculated value because of the face slip. Furthermore, Figure 6-17 shows that at a load of 48 kips, the experimental strain in the bottom face is larger than that in the top face. This indicates that the top face had more severe debonding than the bottom face, probably due to the localized bending effect caused by the steel loading plate.

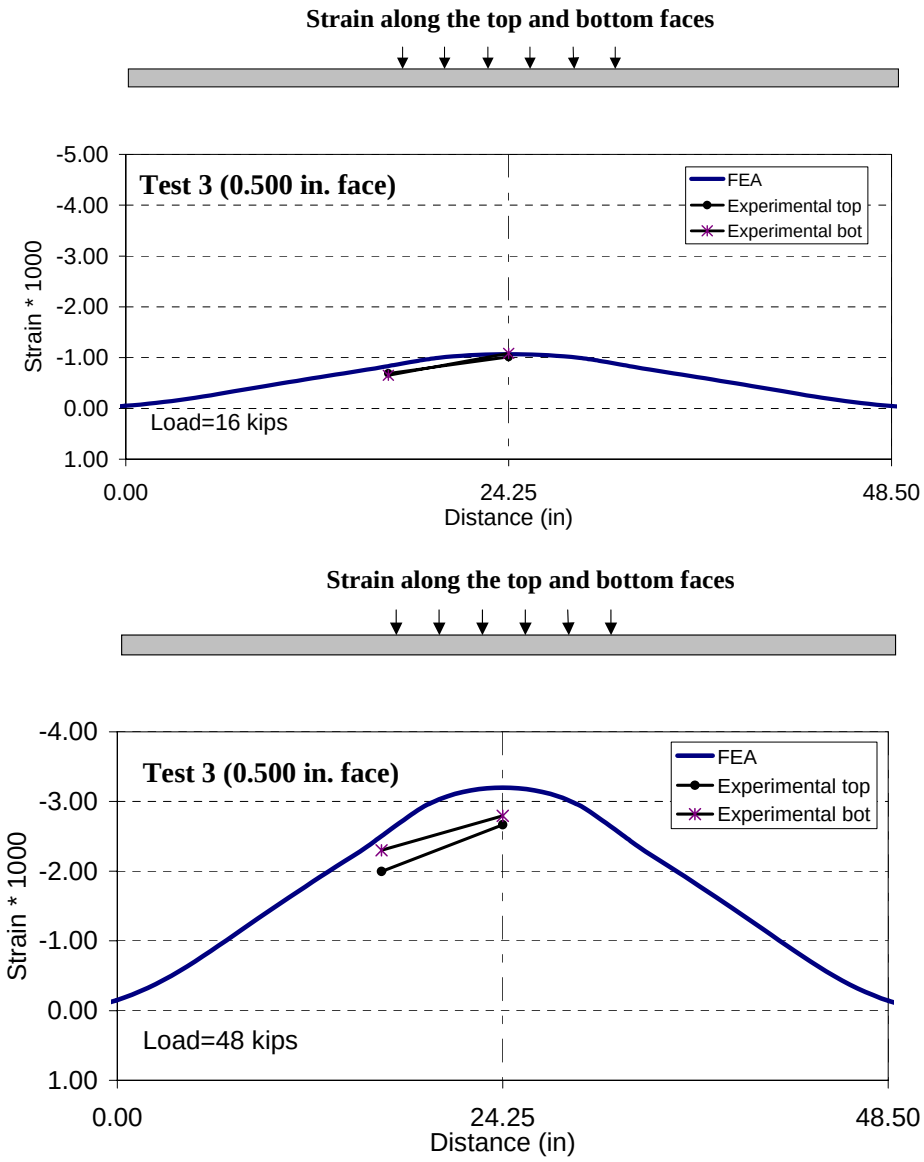

Figure 6-17 Strain distribution along the top and bottom faces of the beam in Test 3 at different loading stages (only the top stain is shown for the FEA)

Figure 6-18 compares the numerical and experimental strain distributions along the top face of the beam in Test 4 at a load of 130 kips. Again, the experimental values are lower than the numerical results probably due to debonding.

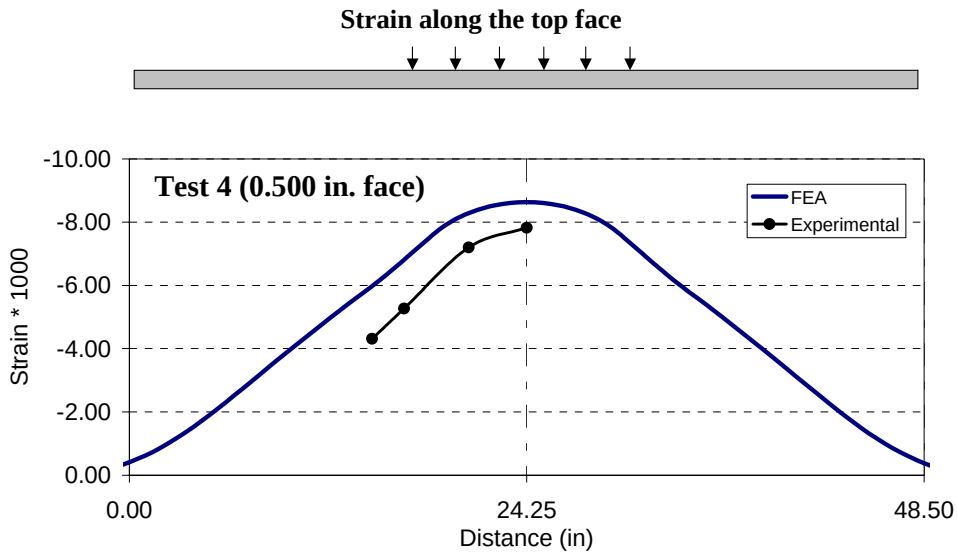

Figure 6-18 Strain distribution along the top face of the beam in Test 4

6.5 Delamination Analysis

Delamination of the top face of a beam is a complex phenomenon that is caused by a combination of high shear and peeling stresses. Peeling stresses are the tensile stresses that are normal to the interface. For the sandwich beams analyzed in this report, the peeling stresses appear to be very small compared to the shear stresses. Hence, it is only important to evaluate the shear stress distribution between the core and the face at failure.

The shear strength between the core and the face, τ, can be calculated with the simple beam theory, i.e., equation (4.20), FE analyses, and experimental strain measurements by considering the failure loads identified in the beam tests. In addition, the formula given by ASTM C393-94 (Standard Test Method for Flexural Properties of Sandwich Constructions) can be used. C393-94 suggests the following equation based on the simple beam theory to calculate the interface shear strength:

$$\tau_{13}^{\text{int}} = \frac{P}{(H+h)b} \tag{6.7}$$

where P is the load applied, and H, h and b are the beam dimensions shown in Figure 4-2.

Equation (6.7) is slightly different from equation (4.20) in that the former does not consider the dimensions of the loading plate and the supports. It should be noted that the shear strength is computed by considering the nominal core width, *b*, as shown in Figure 4-3.

In the FE analyses, the faces of the beams are modeled by a single layer of linear triangular elements and the interface shear stresses are computed at the nodes. Figure 6-19 shows the peeling stresses (σ_{33}) and the shear stresses (τ_{13}) at the top face-core interface of the beam in Test 1 obtained by the FE analysis at a load of 100 kips, which is just below the failure load of 103 kips. As mentioned before, the peeling stresses are so small that they have little influence on the delamination. The shear stresses are predominant and exhibit a peak just outside the loading plate. In the aerospace research community, this stress concentration behavior is a well-known problem for sandwich panels and is called the indentation problem. It is associated with local plate bending and it is due to the local deformation of the loaded face into the soft core. Several researchers (Thomsen and Frostig 1997, Polyakov 2000, Lee and Tsotsis 2000) investigated this problem and showed that the stress predictions based on classical theories are incorrect. Figure 6-20 shows the maximum and minimum principal stresses for Test 1 just below the load of 100 kips. The arch mechanism is clearly shown by the pattern of the minimum principal stresses. The maximum principal stresses indicate a tension oriented at about 45 degrees just outside the loading plate.

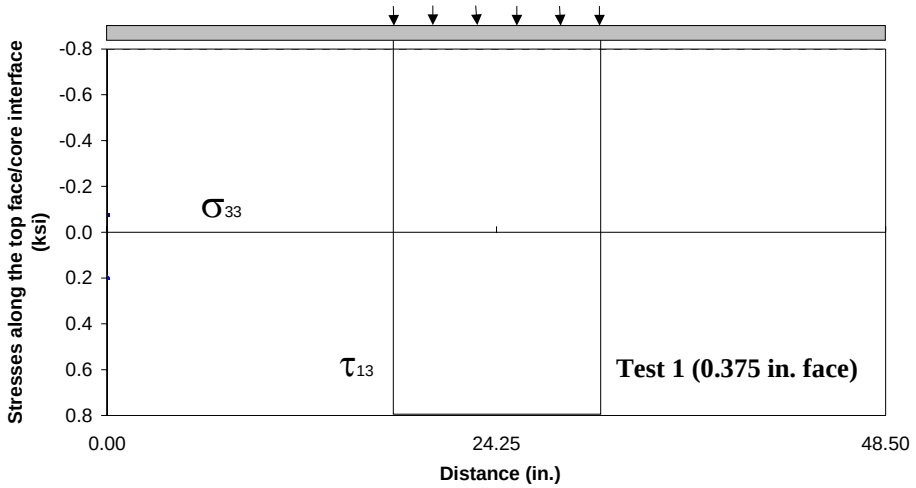

Figure 6-19 Stresses along the interface between the top face and the core of the beam in Test 1 from FE analysis

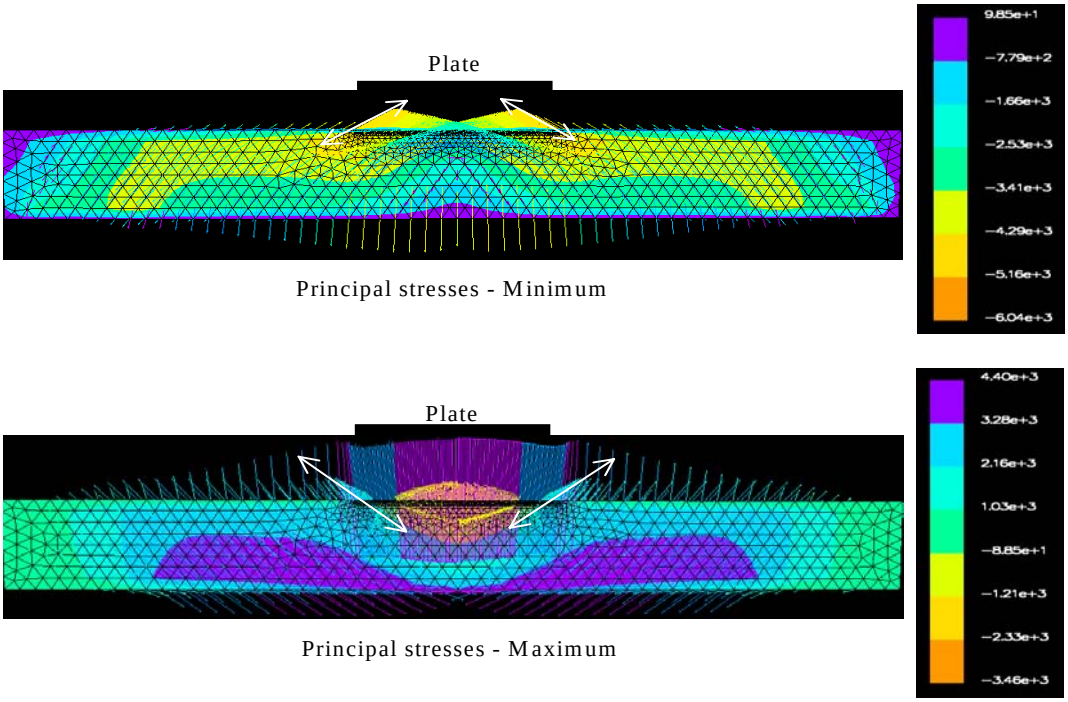

Figure 6-20 Maximum and minimum principal stresses for Test 1 from FE analysis

By considering a schematic similar to that shown in Figure 4-3, the interface shear stress can be estimated from the experimental strain readings in the following way. The resultant bending force in the top face of a beam can be estimated from the strain gage

readings. The net force per unit width acting on a segment of the face between locations *a* and *b* can be calculated as:

$$\Delta F_{a,b} = F_b - F_a = (\varepsilon_b - \varepsilon_a) E_{f11} s \tag{6.8}$$

where *s* is the face thickness, E_{f11} is the Young's Modulus of the face, and *a* and *b* are the locations of the points at which the strains are measured.

By considering the equilibrium of the face in the horizontal direction, $\Delta F_{a,b}$ is equal to the integral of the interface shear stress between *a* and *b*, i.e.,

$$\Delta F_{a,b} = \int_{x_a}^{x_b} \tau(x) dx \tag{6.9}$$

where τ is the shear stress. Considering an average shear stress τ between points *a* and *b*, we have:

$$\Delta F_{a,b} = \tau \int_{x_a}^{x_b} dx = \tau (x_b - x_a) \tag{6.10}$$

Hence, the average interface shear stress can be estimated as:

$$\tau = \frac{\varepsilon_b - \varepsilon_a}{(x_b - x_a)} E_{f11} s \tag{6.11}$$

Table 6-1 presents the shear strengths calculated for all four tests. In Table 6-1, the analytical results are obtained using equation (4.20), and the ASTM results are obtained with equation (6.7). The ASTM equation overestimates the shear stresses because the simplified equation does not take into account the dimensions of the supports and of the loading plate.

Table 6-1 Interface shear stress (ksi) (τ)

	Analytical	ASTM	Experimental	FEA
Test 1 – 0.375 (100 kips)	0.41	0.58	0.33 (sg4)	Max = 0.55; Av = 0.38 (69%)
Test 2 – 0.375 (75 kips)	0.31	0.43	0.30 (sg4-sg6)	Max = 0.46; Av = 0.31 (69%)
Test 3 – 0.500 (40 kips)	0.17	0.29	0.14 (sg3)	Max = 0.23; Av = 0.19 (83%)
Test 4 – 0.500 (130 kips)	0.54	0.70	0.55 (sg4-sg6)	Max = 0.67; Av = 0.55 (83%)

For Test 1 and Test 3, the shear stresses are estimated from the experimental results

with a single gage (sg4) reading by considering the equilibrium of the top face over a distance $x = x_b - x_a$, where x_a is at a free end of the beam as shown in Figure 6-21. For Test 2 and Test 4, the results are obtained by using the readings of the two gages indicated in Table 6-1. Only Test 2 and Test 4 had both sg6 and sg4 gages glued on the top of the beams in the shear span region, where the shear stress is almost constant.

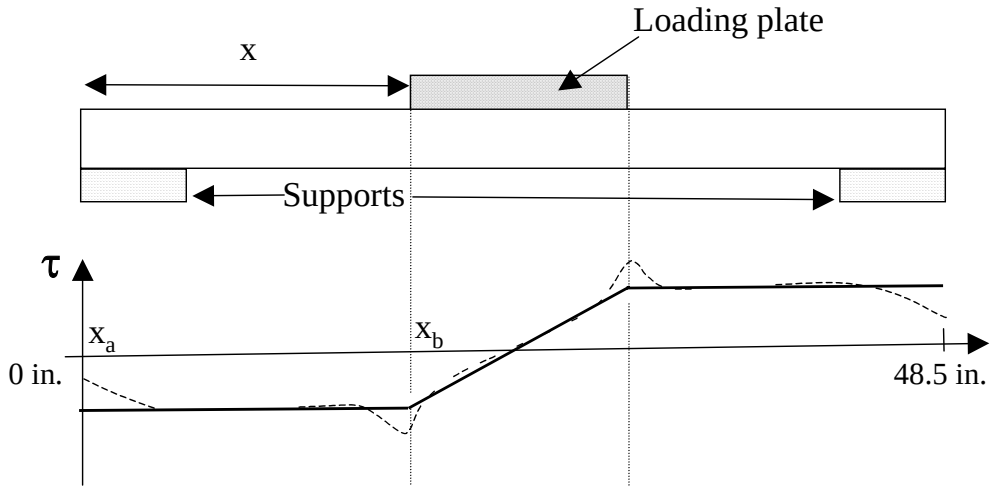

Figure 6-21 Average shear stress

The FE results presented in Table 6-1 show both the maximum shear stress values calculated and the average shear stresses calculated over the distance, x. The average stresses are calculated to compare the FE results to the experimental and analytical results. For the beams with 0.375- and 0.500-in. faces, the average shear stress is 69 % and 83% of the maximum shear stress, respectively. This means that by increasing the face thickness, we can minimize the localized bending effect induced by the loading plate.

The interface shear strengths obtained in this study are compared to that of prior studies (Stone et al. 2001 and Lopez 2001) in Table 6-2. Beams in the prior studies did not have the shear strengthening used in this study (see Figure 2-2).

Table 6-2 Comparison of the interface shear strengths (ksi) with and without shear strengthening

	Without shear strengthening			With shear strengthening	
	Analytical (Eq. (4.20))	ASTM (Eq. (6.7))		Analytical (Eq. (4.20))	ASTM (Eq. (6.7))
Stone 1 (2001)	0.14	0.19	Test 1 - 0.375	0.41	0.58
Stone 2 (2001)	0.21	0.28	Test 2 - 0.375	0.31	0.43
Lopez 1 (2001)	0.08	0.10	Test 3 - 0.500	0.16	0.29
Lopez 1 (2001)	0.085	0.15	Test 4 - 0.500	0.54	0.70
Average	**0.13**	**0.18**	**Average**	**0.36**	**0.50**

For short spans, the ASTM results overestimate the shear strengths and they are shown here only for completeness. The results show that the new shear strengthening detail increased the average shear strength by 2.8 times. In this study, the lowest shear strength value was found in Test 3, which failed in a ductile-like manner because of possible defects in the interface. This and prior studies have shown that the bonding between the faces and the core is the most important parameter governing the bending capacity of a panel. Quality control is important for all engineering materials but is especially critical for composite materials. It is therefore essential that the manufacturing process assures a good quality control of the face-core interface.

6.6 Nonlinear Fracture Mechanics Analysis of the Face-Core Interface

The delamination failure is studied by using a Nonlinear Fracture Mechanics (NLFM) model developed at the University of Colorado (Cervenka et al. 1998) and implemented in an interface element in the program Merlin (MERLIN II User's and Theory Manuals 2002). The discrete crack model used is a generalization of the classical Fictitious Crack Model of Hillerborg et al. (1976), modified to account for the shear effects along the fracture process zone (FPZ) and the crack. In this model, the interface strength is described by the following failure function (Cervenka et al. 1998):

$$F = (\tau_1^2 + \tau_2^2) - 2cTan(\phi_f)(\sigma_t - \sigma) - Tan^2(\phi_f)(\sigma^2 - \sigma_f^2) = 0 \qquad (6.12)$$

where c is the cohesion, ϕ_f is the angle of friction, σ_t is the interface tensile strength, τ_1 and τ_2 are the two tangential components of the interface traction vector, and σ is the

normal traction component. The evolution of the failure function is based on a softening parameter u_{ieff} which is the norm of the inelastic displacement vector $\mathbf{u}^{\mathbf{i}}$. The inelastic displacement vector is obtained by the decomposition of the displacement vector **u** into an elastic part $\mathbf{u}^{\mathbf{e}}$ and an inelastic part $\mathbf{u}^{\mathbf{i}}$. The inelastic part can subsequently be decomposed into plastic (i.e. irreversible) displacements $\mathbf{u}^{\mathbf{p}}$ and fracturing displacements $\mathbf{u}^{\mathbf{f}}$.

Linear softening laws describe the cohesive stresses in the FPZ. The critical opening and sliding corresponding to zero cohesion and tensile strength are denoted by w_σ and w_c, respectively, and they are determined from the condition that the areas under the linear softening law must be equal to mode I fracture energy, G^{I}_{F}, and mode II fracture energy, G^{IIa}_{F}, as shown in Figure 6-22. G^{IIa}_{F} is the mode II fracture energy as defined by Carol et al. (1992).

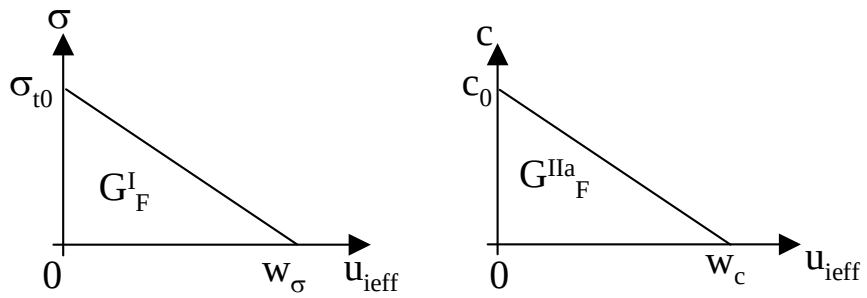

Figure 6-22 Linear softening law

The FE model used here is similar to that in Section 6.3 expect that the top face and the core in this case is connected by a line of interface elements based on the nonlinear fracture mechanics model described above, as shown in Figure 6-23, to allow the delamination to occur. The analyses are performed by increasing the displacement with 0.2-in. increments at the top of a rubber pad that is used to distribute the load uniformly as shown in Figure 6-23. Displacement control is used to capture the post-peak behavior of the load-displacement curve. The material parameters used in the FE analyses are presented in Table 6-3.

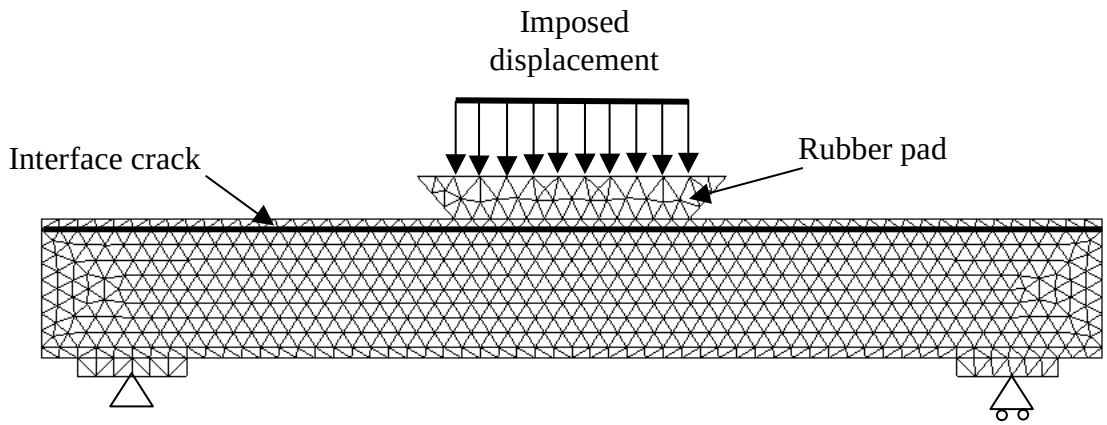

Figure 6-23 Finite element mesh for nonlinear fracture mechanics analysis

Table 6-3 Interface material parameters

Interface parameters	
Shear Stiffness K_t	284000 psi/in. (assumed)
Normal Stiffness K_n	284000 psi/in. (assumed)
Tensile Strength σ_{t0}	380 psi (glue tensile strength from manufacturer)
Cohesion c	550 psi (result from Test 1)
Friction Angle ϕ_f	53 degrees
Dilatancy Angle ϕ_t	45 degrees
Specific mode I fracture energy G^I_F	0.1 lbf/in.
Specific mode II fracture energy G^{IIa}_F	1.0 lbf/in.
Ratio of irreversible displacement γ	0.3
Maximum dilatant displacement u_{max}	0.4 in

The cohesion value is selected to match the result of Test 1. The interface specific mode I fracture energy, G^I_F, is based on tests conducted on similar sandwich panels by Smith (2001). The mode II fracture energy, G^{IIa}_F, is assumed to be 10 times G^I_F. The interface normal stiffness is chosen to be the highest possible value that provides a well conditioned numerical solution. The interface shear stiffness is assumed to be equal to the interface normal stiffness. Since the face-core interface normally exhibits a brittle fracture behavior, the friction angle ϕ_f, the dilatancy angle ϕ_t, ratio of irreversible displacement γ, and the maximum dilatant displacement u_{max} do not influence the numerical results too much. Hence, their values are arbitrarily selected. The analysis results are shown in Figure 6-24. The analysis of Test 1 shows an excellent agreement with the experimental result. This is expected as the model is calibrated to match this test. However, for Test 2 and Test 4 numerical peak loads are 21.5% higher and 28%

lower than the experimental results, respectively. This is because the same fracture properties are used in all the analyses and the interface strengths are different in different test beams as shown in Table 6-1. Similarly, the fracture parameters used do not trace Test 3 accurately. The numerical failure load for Test 3 is 2.66 times the experimental result. As already said, the premature failure in the test was caused by the fact that the top face was not glued to the core with a uniform quality. This reduced the interface shear strength and triggered the premature failure. It is expected that if the actual interface shear strengths were used in the analyses, the numerical results would match the experiments a lot better.

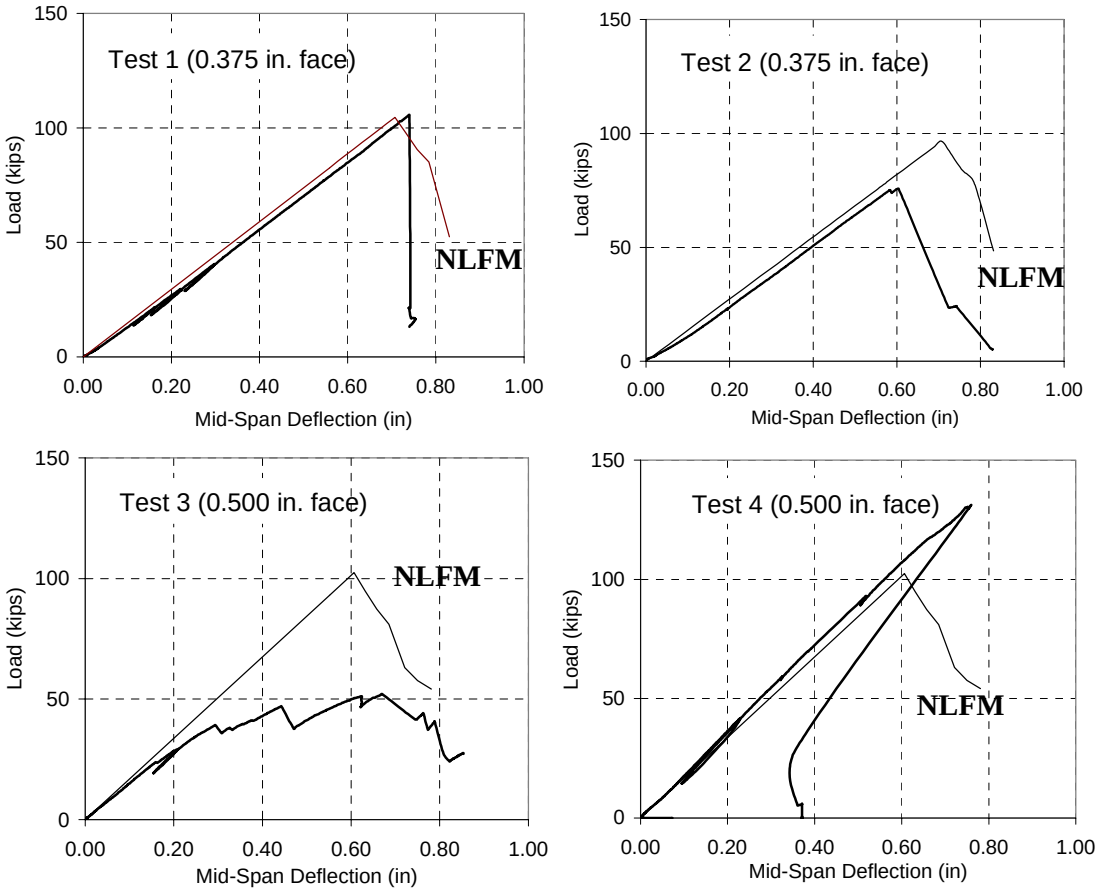

Figure 6-24 Finite element analysis results

Figure 6-25 shows the deformed shape at failure for Test 2. Debonding starts near the edge of the loading plate (Figure 6-25 (a)), and propagates toward the end of the

beam (Figure 6-25 (b)). This result matches the experimental observation.

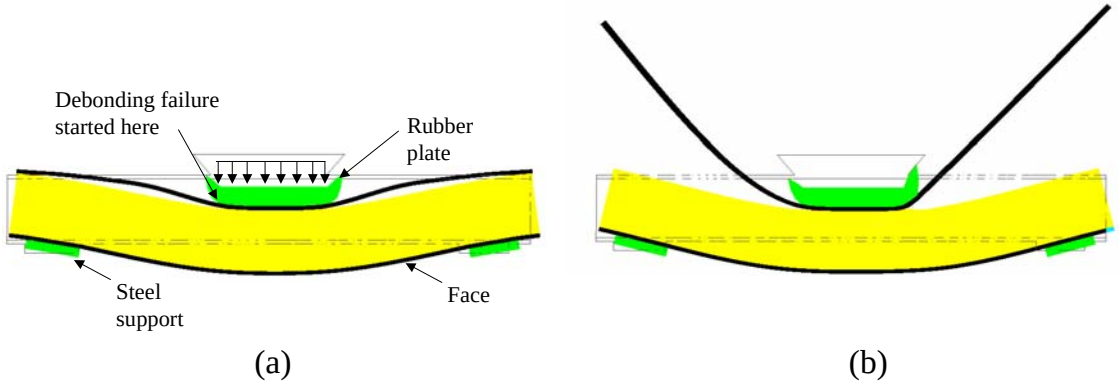

(a) (b)

Figure 6-25 Deformed shape after failure (Amplification factor of 5)

7 PANEL TESTS

7.1 Test Specimen

Tests were conducted to evaluate the static and fatigue load behavior of a GFRP sandwich panel. The panel dimensions are shown in Figure 7-1. The thickness of the faces of the test panel was 0.375 in., and the core height was 6.75 in. The total panel height was 7.5 in. The panel manufacturing process and geometry are described in Chapter 2 in detail.

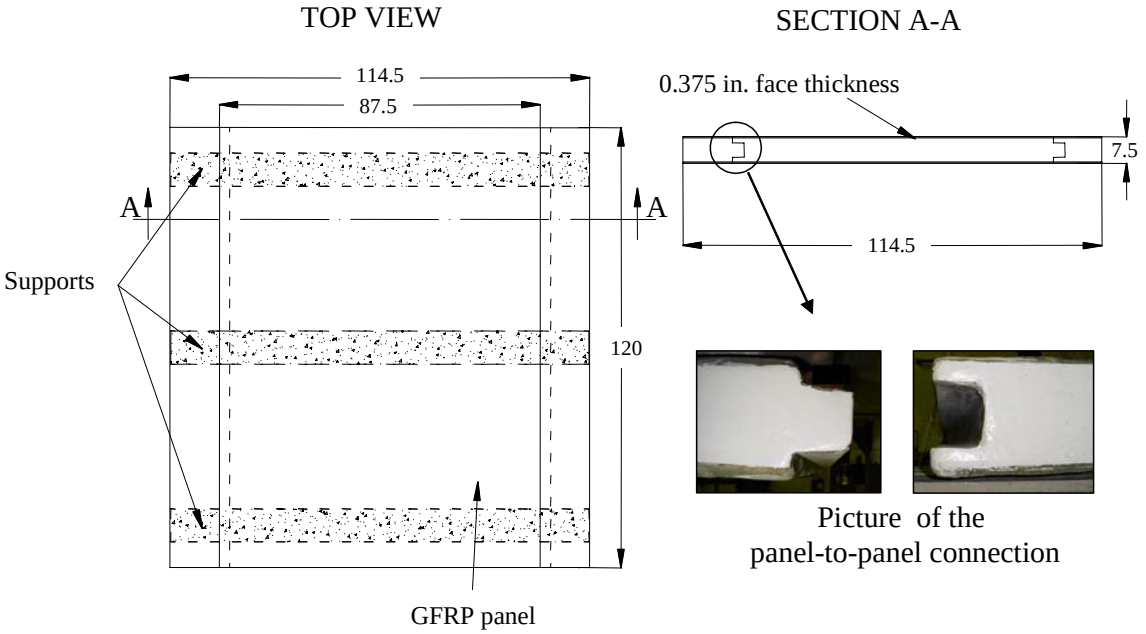

Figure 7-1 Panel dimensions (in inches)

As shown in Figure 1-1, the O'Fallon Park bridge deck consists of 6 panels attached to one another. Each panel is 87.5-in. wide and is connected to the other panels by using the connection shown in Figure 7-1. This type of connection was designed and used by Kansas Structural Composites, Inc. (KSCI) for the first time. The test specimen consisted of two panel-to-panel connections as shown in Figure 7-1 in order to evaluate the performance of the connections as well.

7.2 Test Setup

The panel was tested in a two continuous span configuration with two concentrated loads applied at midspan locations. The test setup is illustrated in Figure 7-2. A reaction steel frame was used to support the actuators. The loads were applied with 13x13x1-in. steel plates and ¾-in.-thick rubber pads between the plates and the deck.

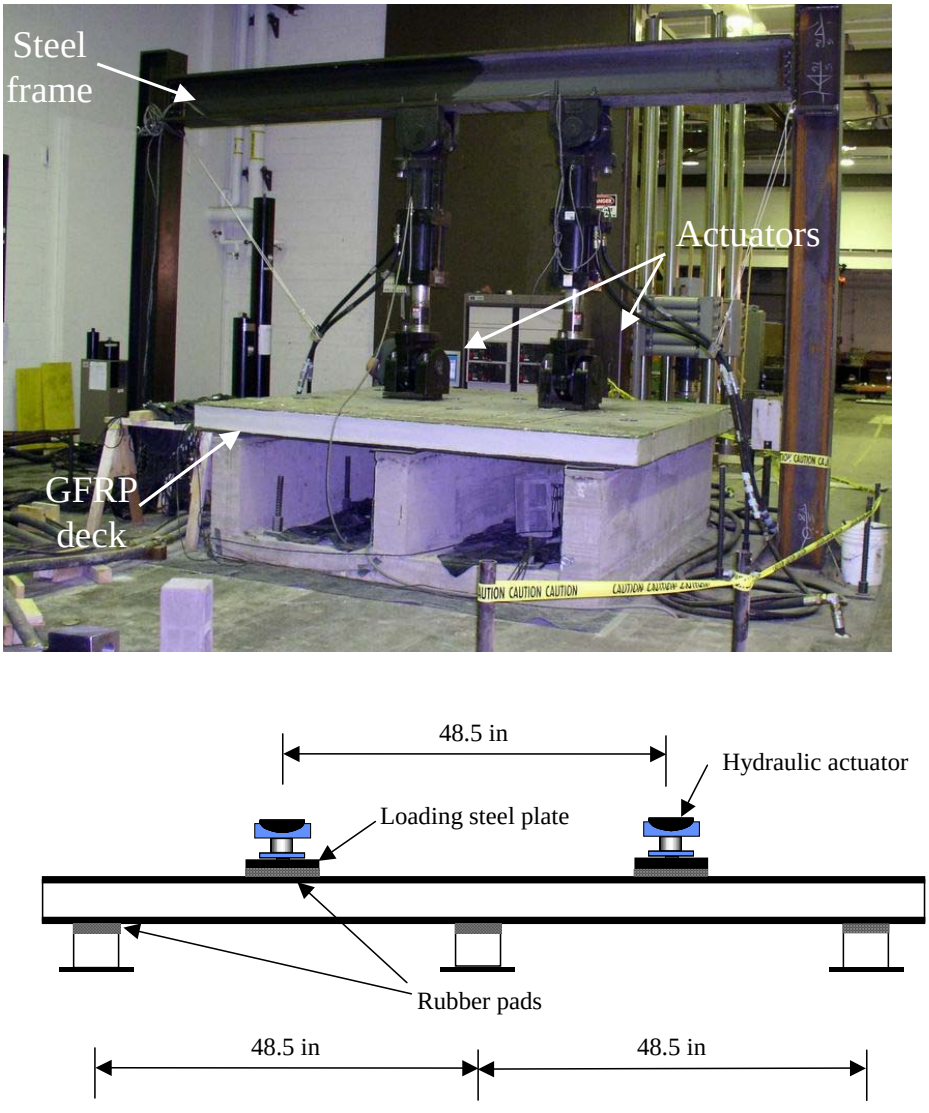

Figure 7-2 Test setup

The test setup was designed to reproduce a segment of the O'Fallon Park bridge

deck. The reinforced concrete support consisted of three risers. The concrete mix was provided by a local supplier. The mix had the following components per cubic yard: 383 lbs of cement, 1430 lbs of sand, 1680 lbs of size #57 aggregates, 259 lbs of water, 25.5 ozs of water reducer, 127 lbs of Class C fly ash, and 4 - 7 percent of air content. The concrete had a specified strength, f'_c, of 4,250 psi, and the steel bars had a specified yield strength, f_y, of 60,000 psi.

No. 4 bars at 4 in. on center were used as main reinforcement. No. 4 bars at 18 in. on center were used for shrinkage and temperature reinforcement as shown in Figure 7-3. After curing, the concrete base was tied down to the test floor with 8-¾-in.-diameter steel bars. Half-inch-thick elastomeric bearing pads were placed on the supporting risers as shown in Figure 7-4. Then, the deck was installed on the risers by Kansas Structural Composites, Inc. (KSCI) as shown in Figure 7-5.

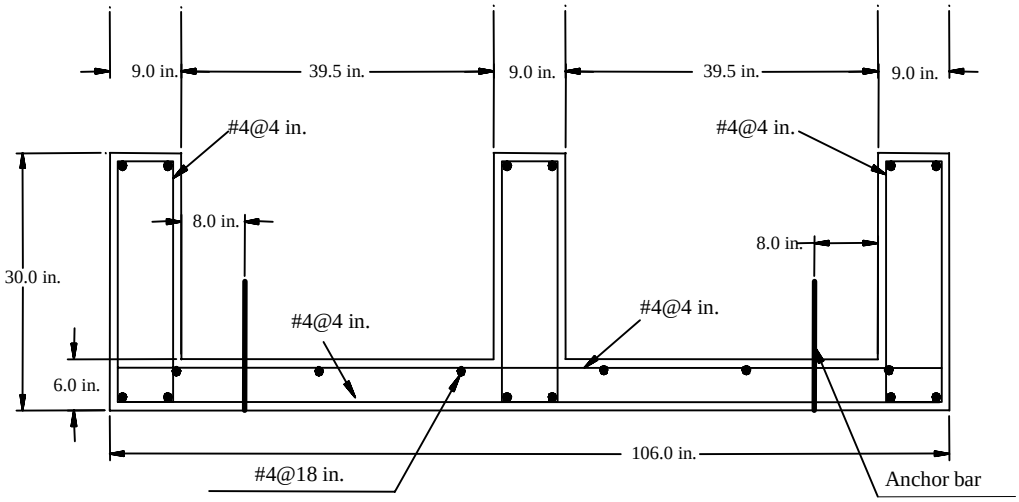

Figure 7-3 Reinforcement details for the supports

Figure 7-4 Support structure

The deck installation proceeded as follows:

- placed the main panel on the bearing pads; over each supporting riser, two holes were drilled into the GFRP panel as shown in Figure 7-5(1). Each hole was 18.75 in. from the center line (Figure 7-6) of the panel.
- drilled holes into the supporting risers for anchor bolts as illustrated in Figure 7-5(2);
- connected the panels together by gluing the panel-to-panel connections; placed a 3 oz. GFRP mat onto the panel top surface across the panel connections as shown in Figure 7-5(3);
- rolled vinylester glue onto the GFRP mat to firmly attach the connections as shown in Figure 7-5(4);
- anchored the deck to the supports by using ¾-in.-diameter galvanized anchor bolts as shown in Figure 7-5(5).

Figure 7-5 Deck installation procedure

7.3 Instrumentation

For strain and deflection measurements, strain gages and linear voltage differential transducers (LVDTs) were attached to the panel. Electrical high precision strain gages produced by Micro Measurements Group, Inc., with a resistance of 350 ohms, were used

along with M-Bond Type AE 10 adhesive system to measure strains. Deflection was monitored using LVDTs. Displacement and strain readings, as well as the load and stroke of the actuators, were recorded during the tests by using a 48-channels data-acquisition system. Figure 7-6 provides a schematic of the strain gage locations and Figure 7-7 indicates the LVDT positions on the panel. For the following discussion, the span on the north side is called Span 1, and the span on the south side is called Span 2, as shown in Figure 7-7.

7.4 Test Procedure

The objective of the tests was to evaluate the load carrying capacity of the GFRP deck panel under static and fatigue loads. The tests were divided into five loading phases as shown in Table 7-1. In Table 7-1, Actuator 1 was used to load Span 1 and Actuator 2 was used to load Span 2. Data were recorded at different loading phases to evaluate the structural performance of the panel as shown in Table 7-2

Table 7-1 Loading stages

	Load cycles	*Loading configuration*
Initial Static Test	0	Both spans loaded at the same time
Phase 1 – Cyclic	0 - 15,200	Actuators 1 and 2 180º off phase
Phase 2 - Cyclic	15,200-370,200	Actuator 1
Phase 3 - Cyclic	370,200 to 1,500,000	Actuator 1
Final Static Test	1,500,000	Actuator 1 and then 2

Table 7-2 Data recorded

	Load cycle No.	*Loading configuration*
Initial Static Test	0	Both spans loaded at the same time
Cyclic data 1	15,000-15,200	Actuators 1 and 2 180º off phase
Cyclic data 2	370,000-370,200	Actuator 1
Static test 1M	1,000,000	Actuator 1
Static test 1.5M	1,500,000	Actuator 1
Final Static Test	1,500,000	Actuator 1 and then 2

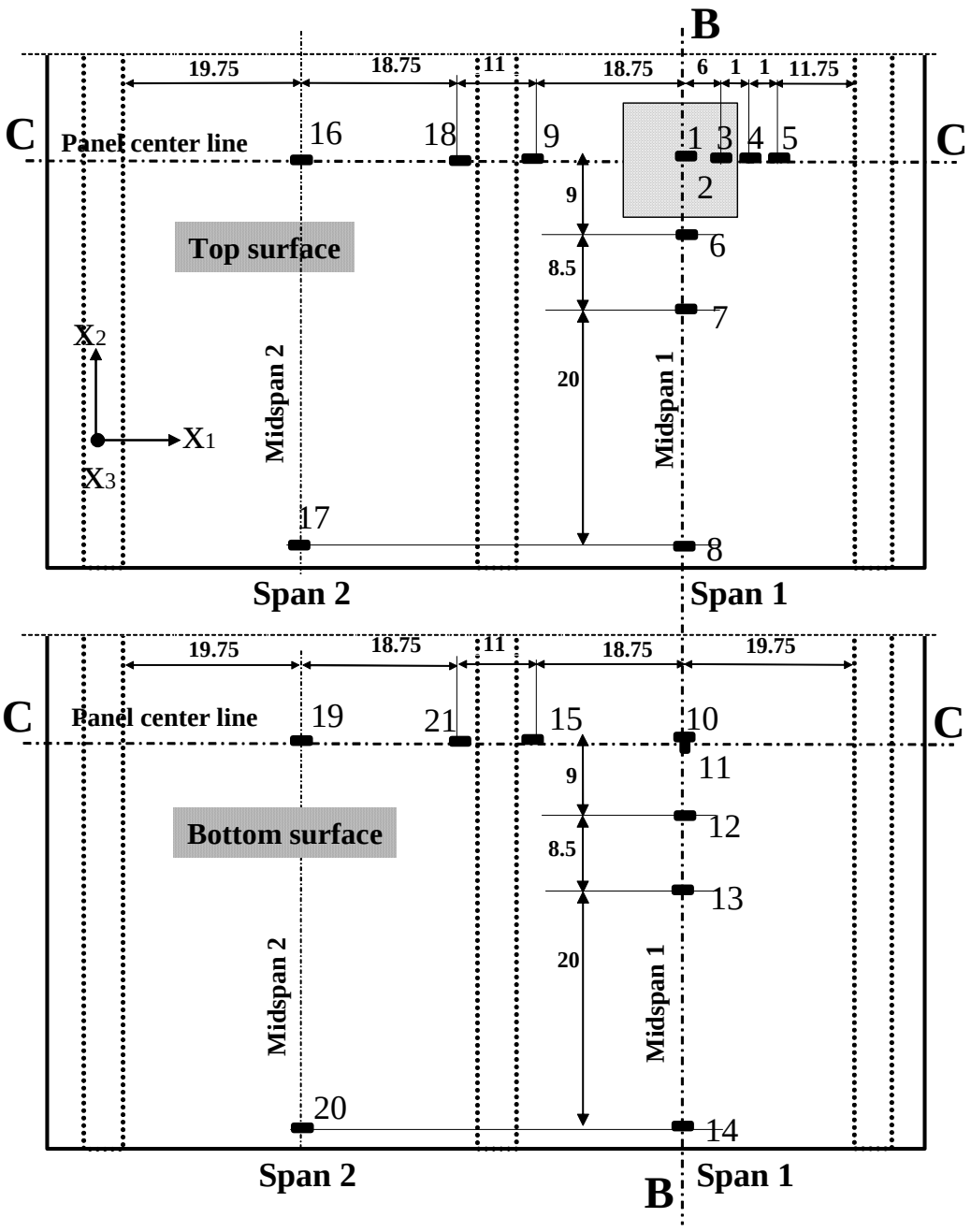

Figure 7-6 Strain gage locations for the panel test (all dimensions in inches)

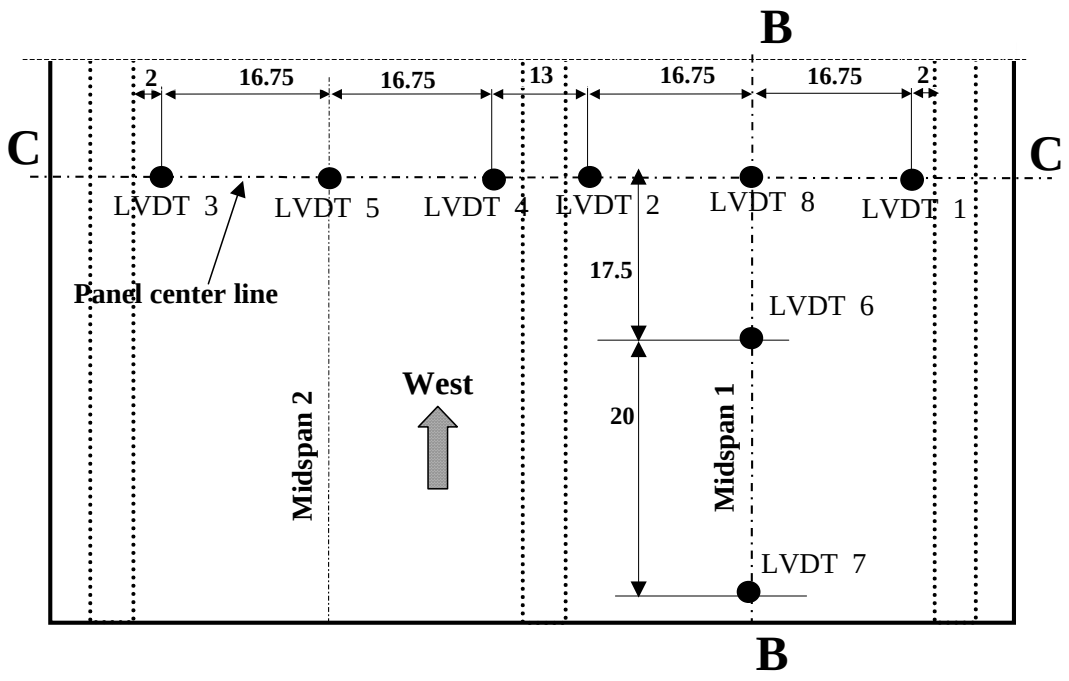

Figure 7-7 LVDT positions (all dimensions in inches)

The panel flexural stiffness was first evaluated through an initial static test, and then a fatigue test was performed to study the long-term performance of the GFRP deck. In the initial static test, both spans were loaded at the same time up to 22 kips. In the subsequent cyclic tests, the panel was loaded by each actuator with a harmonic load given as:

$$p(t) = p_i + p_0 \sin \omega t \tag{7.1}$$

where p_0 is the amplitude of a sine wave, p_i is the offset load, ω is the circular frequency and t is the time. Figure 7-8 shows a plot of the load cycles in which p_0 = 10 kips, p_i = 12 kips, and ω = 1 rad/sec. In this report, compressive load on the deck is considered positive.

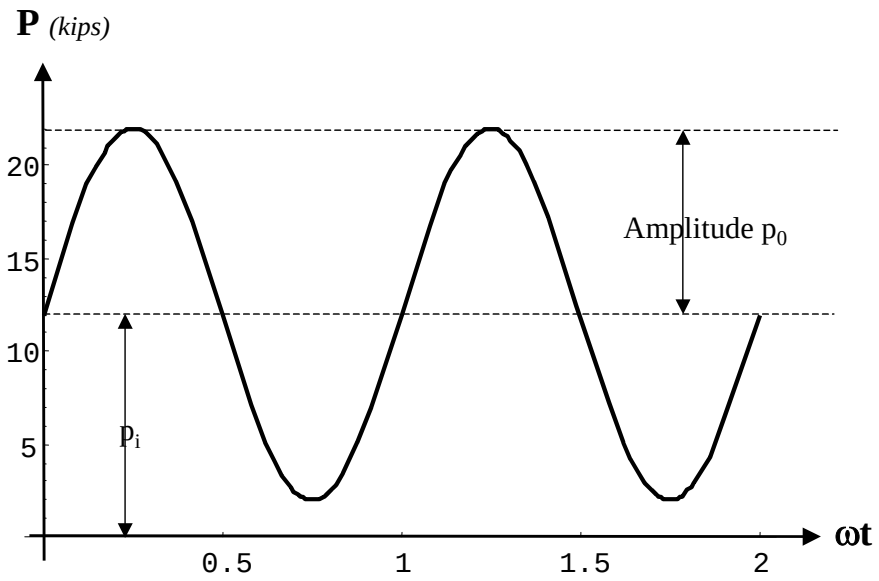

Figure 7-8 Cyclic load definition

The cyclic frequency is $f=2\pi\omega$ and was kept constant at 1.4 Hz during the three fatigue load phases. The values of p_0 and p_i and the loading schemes were varied in the cyclic tests as follows:

Phase 1: From 0 to 15,200 cycles, the loads in Actuators 1 and 2 were 180° off-phase with p_0 = 19 kips and p_i = 21 kips. At about 15,000 cycles, Span 2 started emitting a strong noise. Strain gage and LVDT data were recorded between 15,000 and 15,200 cycles to evaluate the panel damage (Cyclic data 1 in Table 7-2).

Phase 2: From 15,200 to 370,200 cycles, only Actuator 1 was used to load the panel with p_0 = 10 kips and p_i = 12 kips. Between 370,000 and 370,200 cycles, data were recorded to evaluate the panel performance (Cyclic data 2 in Table 7-2).

Phase 3: From 370,200 to 1,500,000 cycles, only Actuator 1 was used to load the panel with p_0 = 14 kips and p_i = 17 kips. At 1,000,000 cycles, the cyclic test was interrupted to perform a static test to evaluate the panel performance (Static Test 1M in Table 7-2). At about 1,500,000 cycles, Span 1 started emitting a strong noise. Thus, a static test was performed right after 1,500,000 to evaluate

the damage in the panel (Static Test 1.5M in Table 7-2).

At the end of the fatigue test, the two spans were loaded one at a time up to 100 kips, which is close to the loading capacity of the actuators used.

7.5 Initial Static Test

The purpose of the initial static test was to evaluate the flexural behavior of the virgin panel. In this test, both spans were loaded at the same time up to 22 kips. Both strain gage and LVDT data were obtained in this test. A schematic of the LVDT locations along the center line of the panel (line C-C in Figure 7-7) is shown in Figure 7-9.

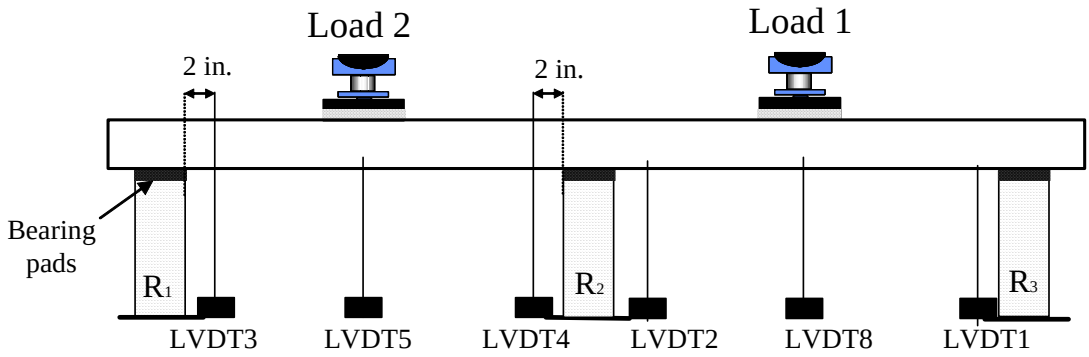

Figure 7-9 Elevation view of the LVDT locations

The panel stiffness was difficult to determine from the test results because it was influenced by the settlement of the bearing pads. For this reason, one LVDT was placed near each support to record the displacement due to the settlement of the bearing pads. Figure 7-10 shows the experimental load-displacement curves from all the LVDTs placed along line C-C shown in Figure 7-7.

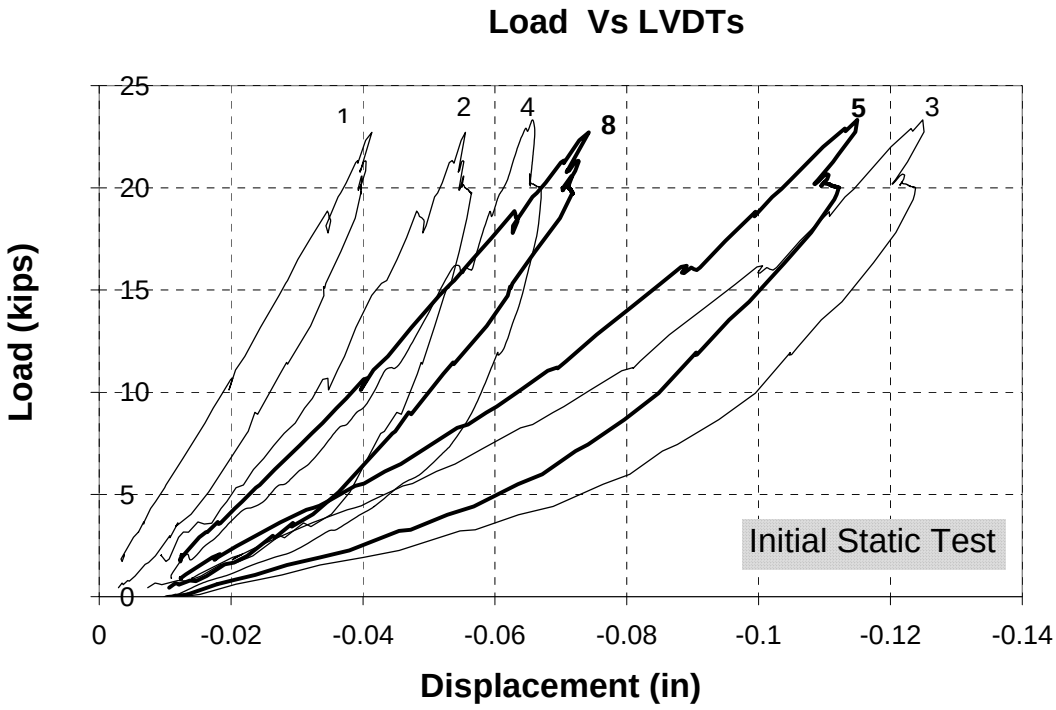

Figure 7-10 Load-displacement curves for the initial static test

The anchor bolts on riser R_1 (see Figure 7-9) slipped during the test. Visual inspection at the end of the static test showed that the bearing pad placed on riser R_1 moved from the initial position. The pad rotated and left a gap between the riser and the panel at the location of line C-C, and this explains why LVDT 3 registered a larger deflection than LVDT 5. The deformed shape of the panel at 22 kips, drawn with AUTOCAD 2000 using the LVDT readings, is shown in Figure 7-11. In this figure, a Bezier curve is used to approximate the deformed shape and estimate the actual deformation of the panel. A Bezier curve is a simple cubic equation and was originally developed by Pierre Bézier in the 1970's for CAD applications. A cubic Bezier curve is defined by four points: (x_0,y_0) is the origin point, and (x_3,y_3) is the destination point, and (x_1,y_1) and (x_2,y_2) are control points.

Equations (7.2) and (7.3) are used to define the points on a Bezier curve. The points on the curve are evaluated by varying the values of t between *0* and *1*. One equation

yields values for x, and the other yields values for y.

$$x(t) = a_x t^3 + b_x t^2 + c_x t + x_0 \quad (7.2)$$

$$y(t) = a_y t^3 + b_y t^2 + c_y t + y_0 \quad (7.3)$$

where:

$c_x = 3\,(x_1 - x_0)$
$b_x = 3\,(x_2 - x_1) - c_x$
$a_x = x_3 - x_0 - c_x - b_x$

$c_y = 3\,(y_1 - y_0)$
$b_y = 3\,(y_2 - y_1) - c_y$
$a_y = y_3 - y_0 - c_y - b_y$

All dimensions in Figure 7-11 are in scale, with the displacements in the x_3 direction amplified 30 times. The curve is forced to have a horizontal tangent at the center of the interior riser, R_2, and it is used to estimate the bearing pad settlements at the supports.

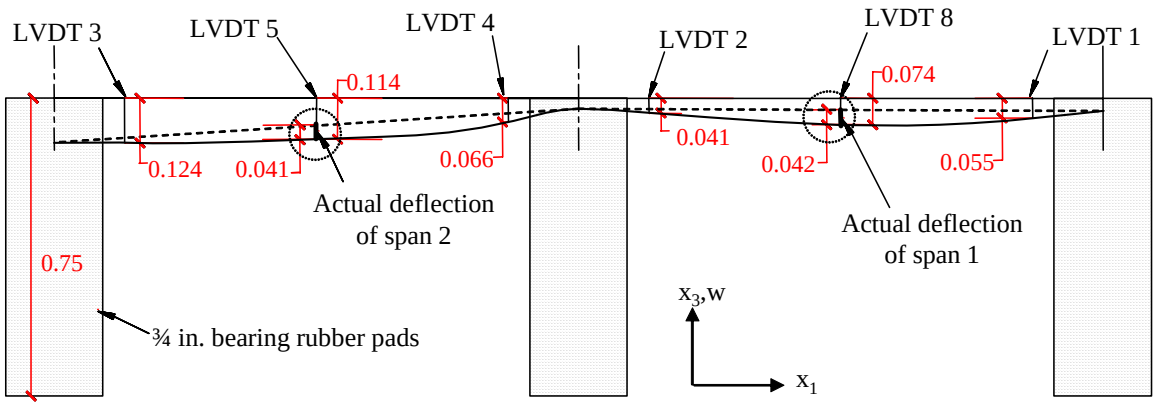

Figure 7-11 Deformed shape along line C-C (All dimensions in inches, deflections amplified 30 times)

The actual panel deflections at midspans are estimated with the deflection curve in Figure 7-11 by taking out the rigid-body displacement due to the support settlements. As shown in Figure 7-12, the load-vs-actual displacement curves for the two spans are much stiffer than those obtained with the unadjusted readings from LVDT 5 and 8.

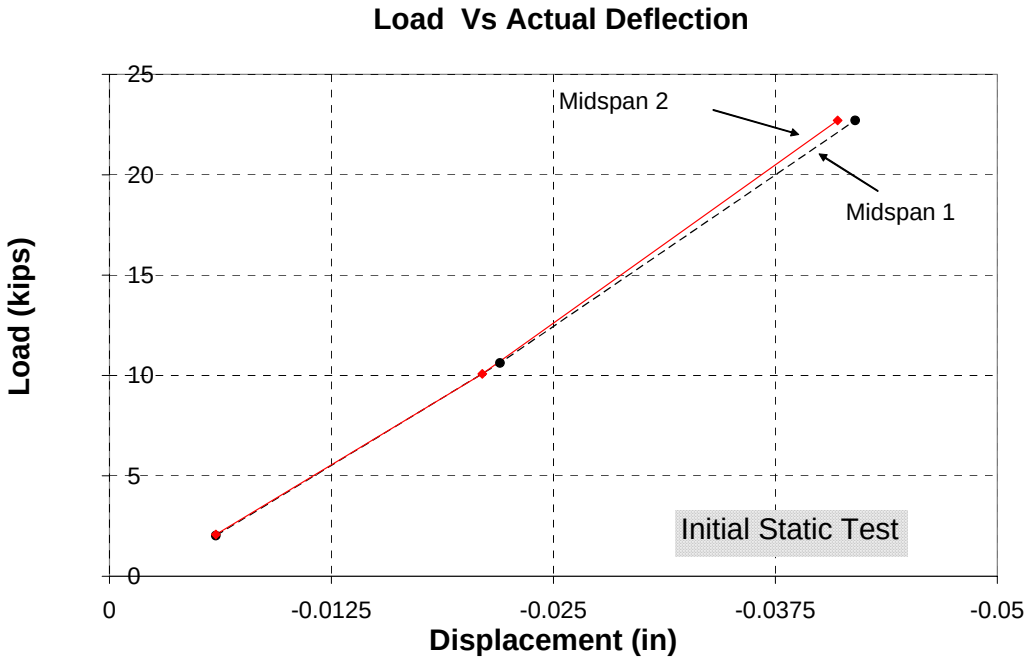

Figure 7-12 Load-vs-actual deflection curves for the initial static test

From the load-displacement curves in Figure 7-12, we can see that the midspan deflections under the service loads of 26 kips were 0.048 and 0.047 in. for Spans 1 and 2, respectively. These satisfy the deflection limit of L/1000 (0.05 in.) specified in the design provisions of the City and County of Denver.

Figure 7-13 shows the load-strain curves obtained from all the strain gages glued on the panel. Loads 1 and 2 are defined in Figure 7-9. The curves are linear. As expected, the strain decreases with increasing distance from line C-C (Figure 7-6). At 37.5 in. from line C-C, the deformation is negligible. Figure 7-14 shows the strains ε_{11} along line B-B (Figure 7-6) obtained from the gages glued on the top and bottom of Span 1, where ε_{11} is the longitudinal strain in direction x_1 as defined in Figure 7-6.

Figure 7-14 shows that the top surface had a distinct kink in the strain-vs-distance curve indicating localized deformation introduced by the loading plate. This localized bending is due to the indentation of the soft core as explained in Section 6.5. The gages glued on the bottom detected a less localized bending and showed a more linear variation

of strain with distance.

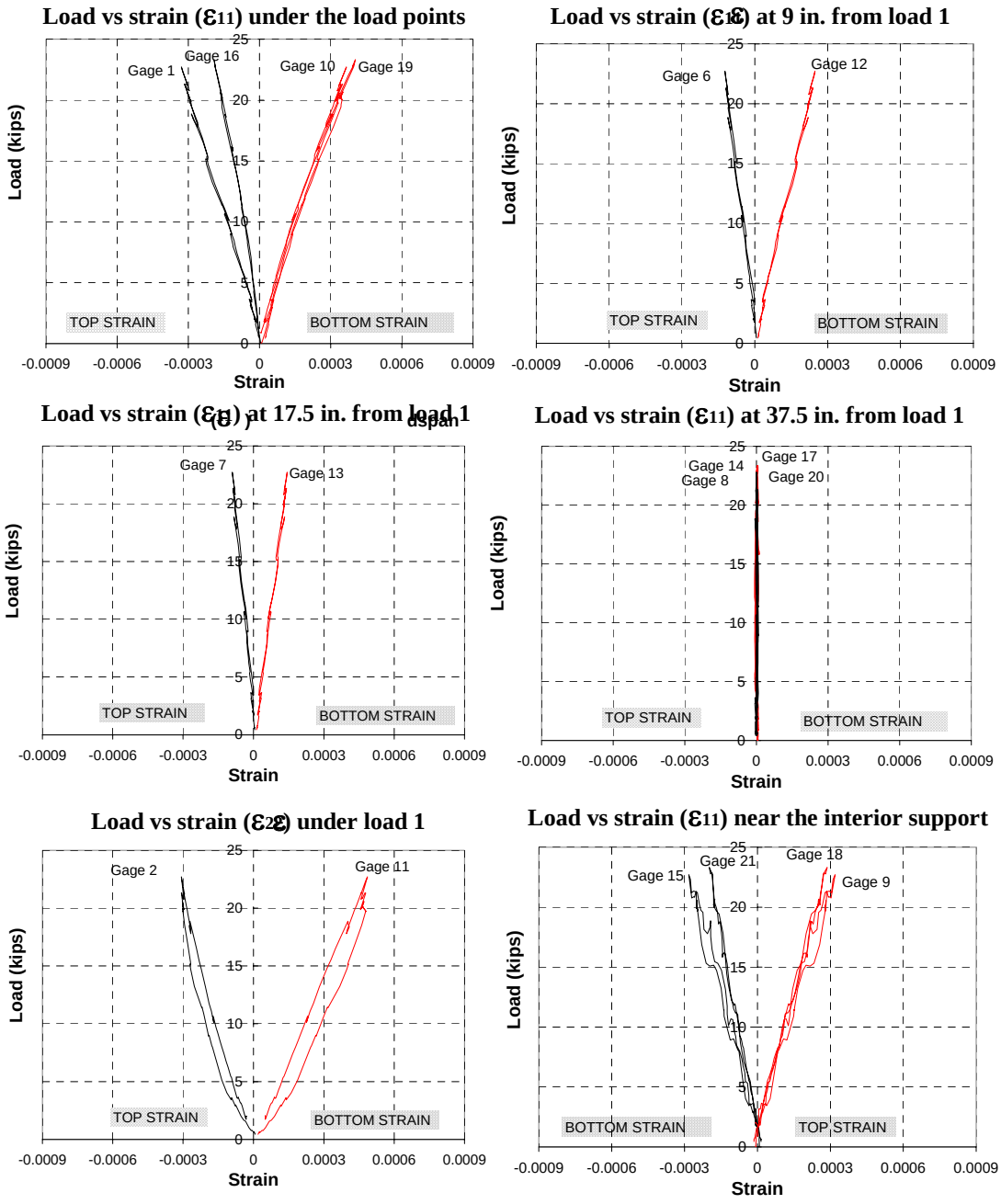

Figure 7-13 Load-strain curves for the initial static test

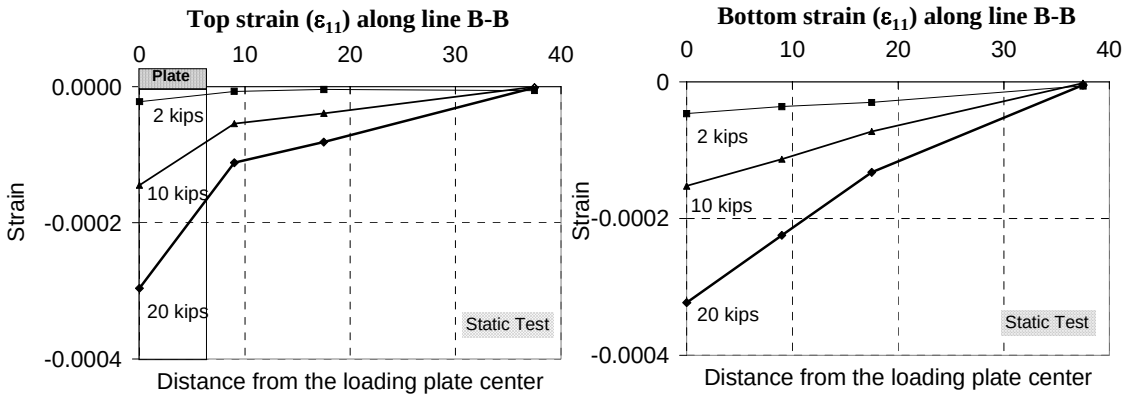

Figure 7-14 Strain ε_{11} along line B-B at different loading stages

The panel strain, ε_{11}, plotted along line C-C under a 20-kip load is shown in Figure 7-15. On the top of Span 1, two strain gages were glued just outside the loading plate as shown in Figure 7-6. The strain gradient, $d\varepsilon_{11}/dx_1$, gives an indication of the magnitude of the shear strain γ_{13} as explained in Section 6.5. Figure 7-15 indicates that the indentation of the core increases the shear strain near the loading plate. The different strain values between Span 1 and Span 2 are probably due to the gap caused by the rotation of the bearing pad on riser R_1. The gap decreases the strain at the middle of Span 2 as shown by the deflection curve in Figure 7-11.

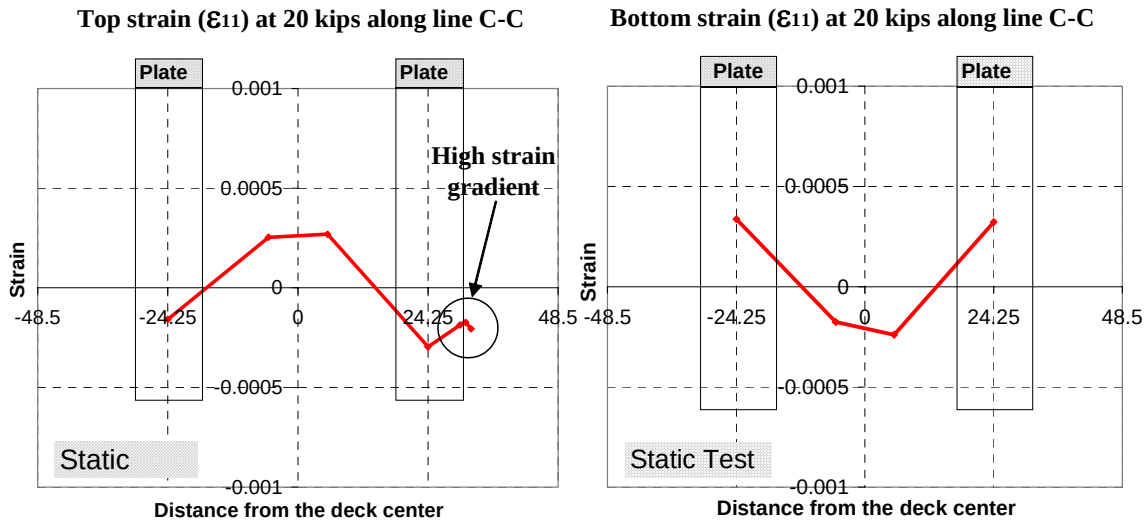

Figure 7-15 Strain ε_{11} along section C-C

The localized bending near the loading plate was observed clearly during the test as shown in Figure 7-16. Figure 7-17 shows the strain profiles along line C-C at 20-kip load and indicates that in Span 1, the neutral axis was at the mid-height of the panel cross section. However, in Span 2, the neutral axis was not at the mid-height of the panel section, but was shifted toward the upper face at the middle of Span 2 and shifted toward the lower face near the interior riser, R_2.

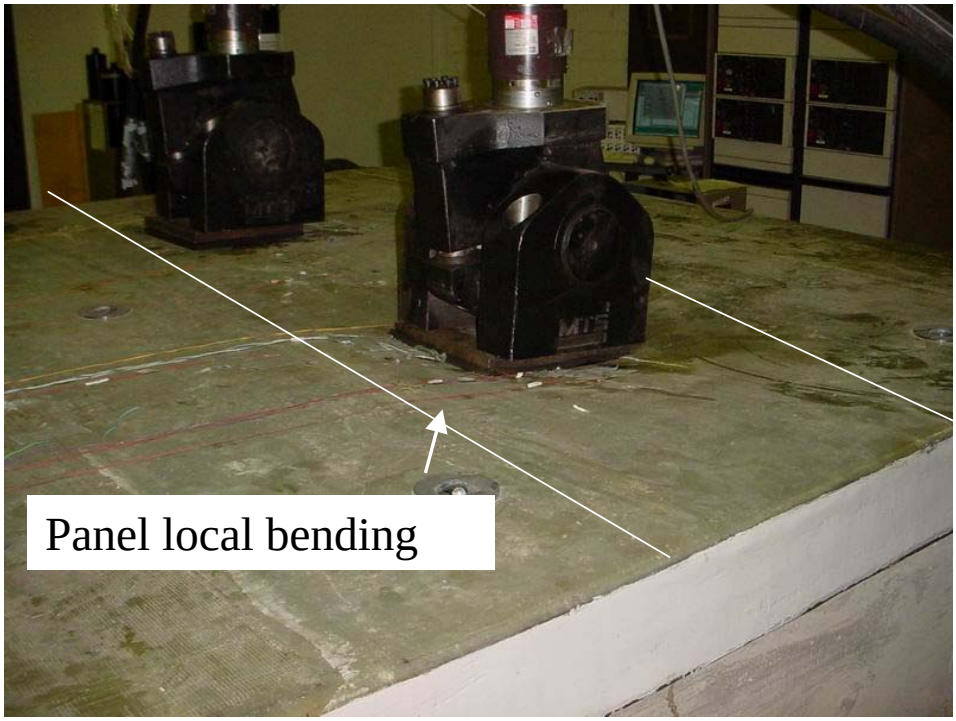

Figure 7-16 Picture of the panel local bending

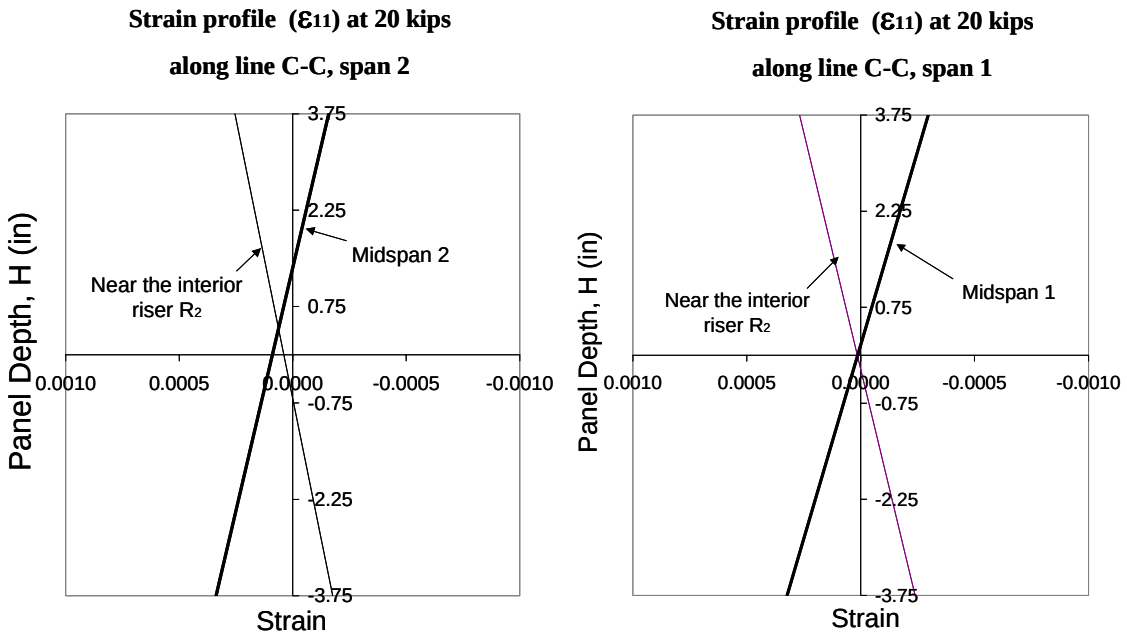

Figure 7-17 Panel strain profiles

Since no panel delamination was expected at this loading stage, the shift of the neutral axis was probably caused by the member tension exerted by the anchor bolts as the panel experienced excessive settlement at riser R_1, as illustrated in Figure 7-18.

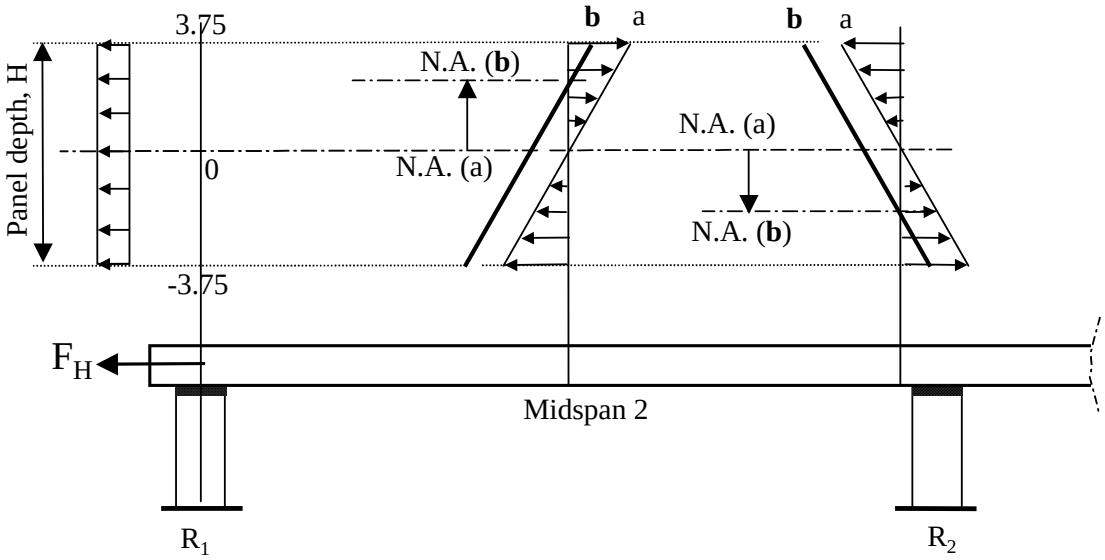

Figure 7-18 Membrane tension due to the anchor bolts

It must be mentioned that if the neutral axis shifts in opposite directions at midspan and near the interior riser, the cause is most likely the horizontal force. Conversely, if the neutral axis shifts in same direction, the cause could be the delamination of one of the two faces.

7.6 Fatigue Test

The aim of the fatigue test was to investigate the influence of the load cycles on the load carrying capacity of the panel and on the performance of the anchor bolts. The fatigue test had three different loading phases as described in detail in Section 7.4. In Phase 1 (from 0 to 15,200 cycles), the loads in Actuators 1 and 2 were 180° off-phase with a peak load of 40 kips. In Phase 2 (from 15,200 to 370,200 cycles), only Actuator 1 was used with a peak load of 22 kips. In Phase 3 (from 370,200 to 1,500,000 cycles), only Actuator 1 was used with a peak load of 31 kips.

7.6.1 Phase 1 - 0 to 15,200 cycles

The two spans were loaded by two actuators with sine waves that were 180° off-phase and a maximum load of 40 kips in each actuator. At about 14,000 cycles, Span 2 started emitting a strong noise near the loading plate. Inspection of the panel did not show any external damage. The noise was very likely caused by the delamination of the upper face from the core. Between 15,000 and 15,200 cycles, data were recorded for 200 cycles (Cyclic data 1 in Table 7-2). The load-strain curves are shown in Figure 7-19.

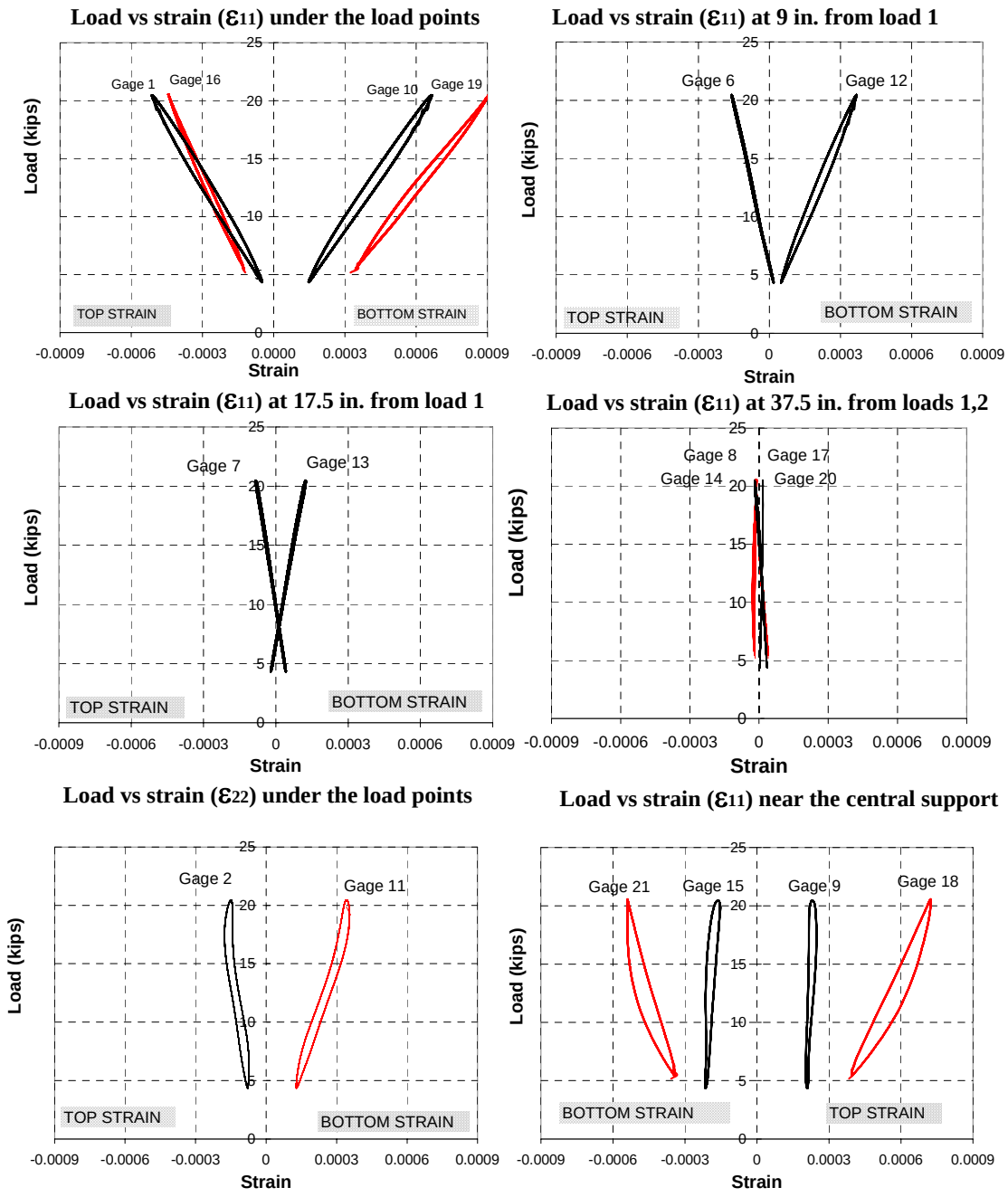

Figure 7-19 Load-strain curves for all the strain gages at 15,000 cycles

Gages 16, 18, 19 and 21 glued on Span 2 show permanent deformation. Gages 16 and 19 were attached to the top and bottom faces of the panel right underneath the load in Span 2. Gage 19 showed a larger strain than gage 16. This was probably caused by the delamination of the top face. The gages glued at 37.5 in. from the loading point showed

small strains as in the initial static test. The gages glued on the negative moment region of Span 2 (gages 18 and 21) showed large deformation compared to the corresponding gages in Span 1.

Figure 7-20 compares the load-displacement curves obtained from the midspan locations at the initial static test (0) and between 15,000 and 15,200 cycles. As indicated in Table 7-1, the loading schemes are different, and, therefore, the stiffnesses cannot be compared directly. However, LVDT 8 showed similar results at the initial static test and between 15,000 and 15,200 cycles, while LVDT 5 indicated a much larger deformation between 15,000 and 15,200 cycles than at the initial static test. This is probably due to the delamination of one of the faces from the core in Span 2.

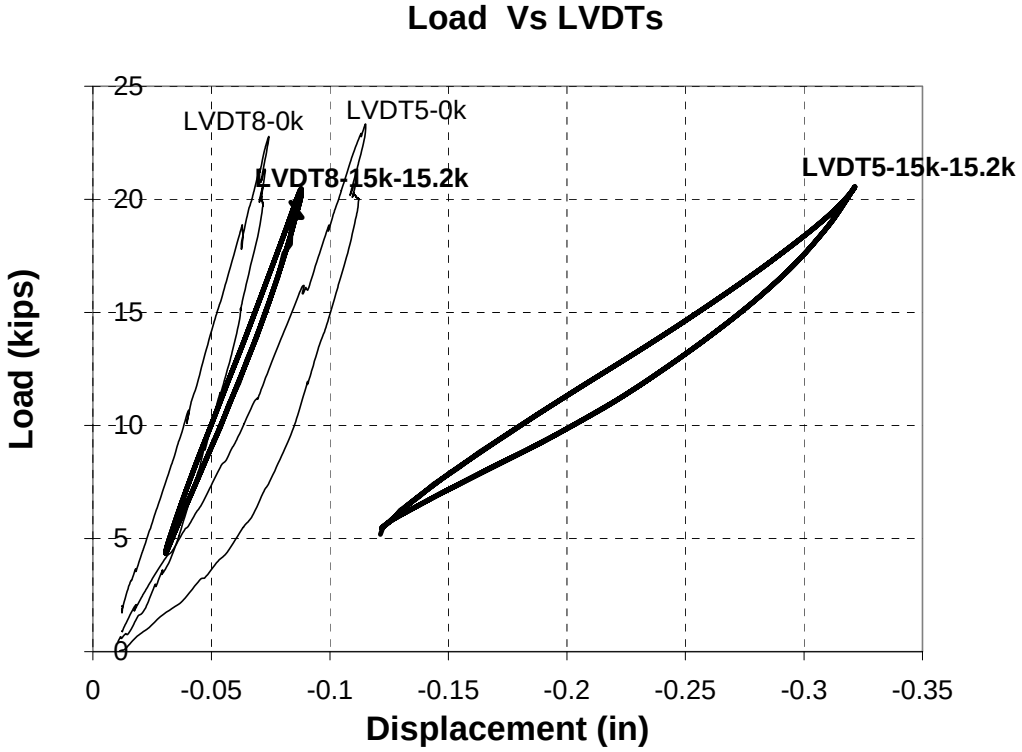

Figure 7-20 Comparison of the load-displacement curves at the initial static test (0k) and between 15,000 and 15,200 cycles

7.6.2 Phase 2 -15,200 to 370,200 cycles

Between 15,200 and 370,200 cycles, only Actuator 1 was loaded with a maximum load of 22 kips. Until 370,000 cycles, no noise emission was noted and cyclic test data were recorded to evaluate the panel performance (Cyclic data 2 in Table 7-2). The strain gage readings obtained in Span 1 between 15,000 and 15,200 cycles (15k - 15.2k) and between 370,000 and 370,200 cycles (370k - 370.2k) are compared in Figure 7-21. The loading schemes were different; between 15,000 and 15,200 cycles, both spans were loaded sinusoidally with a phase angle of 180°, whereas between 370,000 and 370,200 cycles, only Actuator 1 was loaded. This means that between 15,000 and 15,200 cycles, when Span 1 was loaded with 20 kips, Span 2 was loaded with 2 kips; between 370,000 and 370,200 cycles, when Span 1 was loaded with 20 kips, Span 2 was not loaded. The latter loading scheme produced a larger uplift force on the damaged anchors, and, therefore, induced a larger horizontal membrane force F_H (Figure 7-15) on the panel.

The slopes of the load-strain (ε_{11}) curves under the point load between 15,000 and 15,200 cycles and between 370,000 and 370,200 cycles are very similar, and this indicates that there was no damage in the deck. The stiffer behavior of the load-strain (ε_{22}) curves between 370,000 and 370,200 compared to those between 15,000 and 15,200 cycles could have been caused by the horizontal membrane force acting on the panel as mentioned previously.

Gage 8, glued at the end of the panel (37.5 in. from load 1) on the top face of Span 1 indicated permanent deformation between 370,000 and 370,200 cycles. This is in contrast with the initial static test in which the same gage did not show any deformation. Therefore, it is very unlikely that the panel was damaged at this location by the cyclic loading. Probably, this permanent deformation is due to the permanent anchor bolt slippage at riser R_1, which prevented the panel at the supported end from bouncing back to the undeformed configuration.

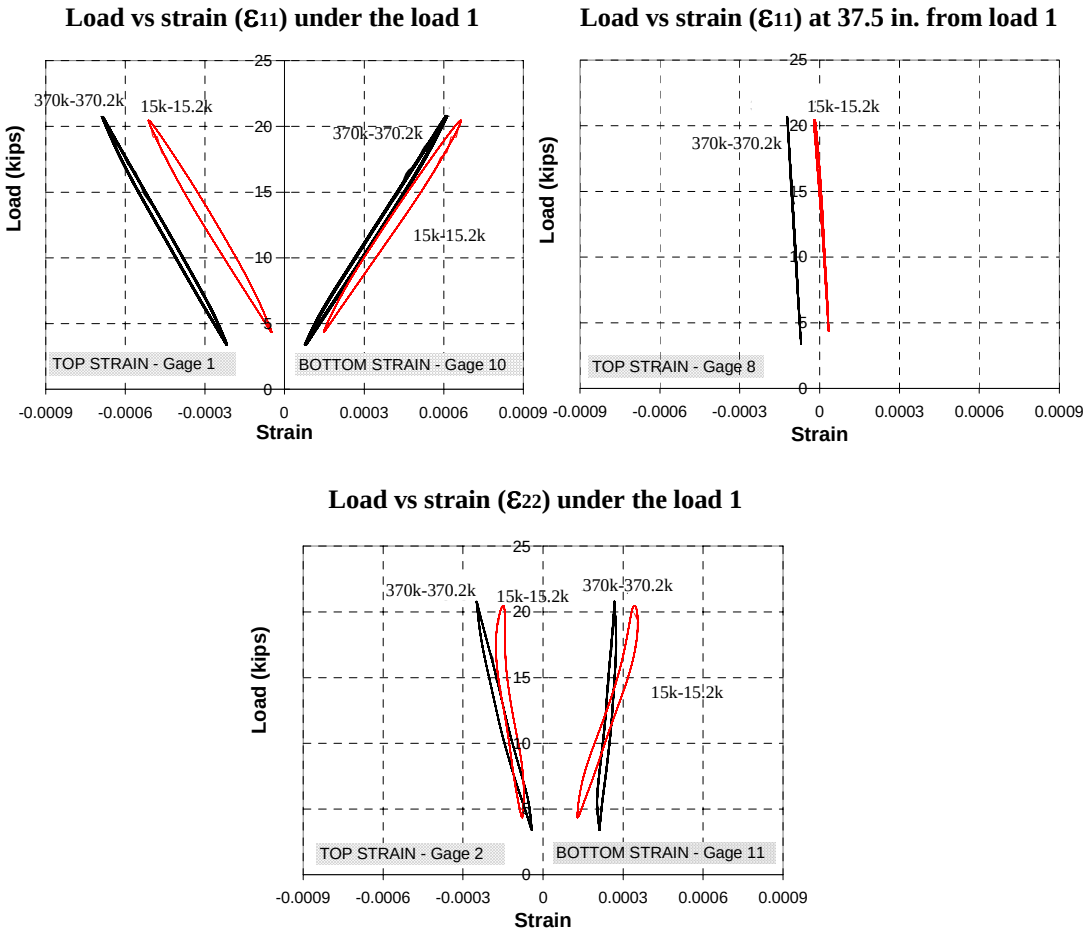

Figure 7-21 Load-strain curves at 370,000 cycles

7.6.3 Stage 3 - 370,200 to 1,500,000 cycles

At 370,200 cycles, the deck was examined and no damage was observed. The loading of Actuator 1 was increased to a maximum load of 31 kips for subsequent cycles. At 1,000,000 cycles, the test was interrupted to perform a static test to evaluate the panel behavior (Static Test 1M in Table 7-2). To compare the results with those of the initial static test, both spans were loaded at the same time up to 20 kips. Figure 7-22 shows that the strains under the loading plates and near the interior support, R_2, were larger at 1,000,000 cycles than at the initial static test for both spans under similar loads. The stiffness change is probably due to damage in the interface between the faces and the

core. In particular, in Span 2, the strain near the middle support (negative moment region) at 1,000,000 cycles is more than four times larger than the strain at 0 cycle.

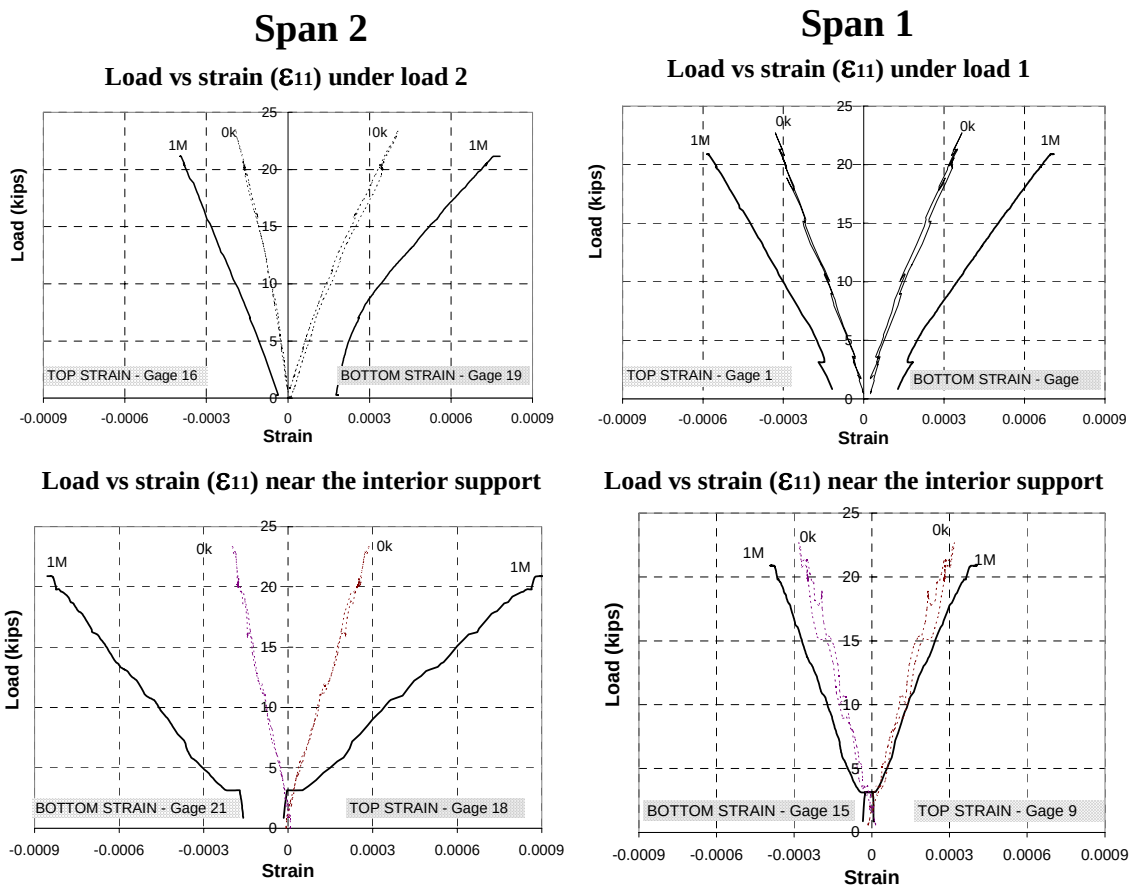

Figure 7-22 Load-strain curves at 1,000,000 cycles

The strain profiles in Figure 7-23 indicate that the neutral axis in Span 1 did not change position during the fatigue loading. The softening was probably caused by the delamination of Span 2. For Span 2, near the interior riser, R_2, the neutral axis at 1,000,000 cycles shifted upward, whereas at midspan, the neutral axis did not move, as shown in Figure 7-24. The progressive damage of the panel is different from that of the beams tested previously. In the beam tests, when one of the two faces delaminated, the neutral axis shifted from its initial position (the neutral axis shifted upward if the lower face debonded and downward if the upper face debonded) and the failure ensued. In the panel test, the delamination of the faces was not necessarily followed by collapse because damage could be local and stress redistribution could occur.

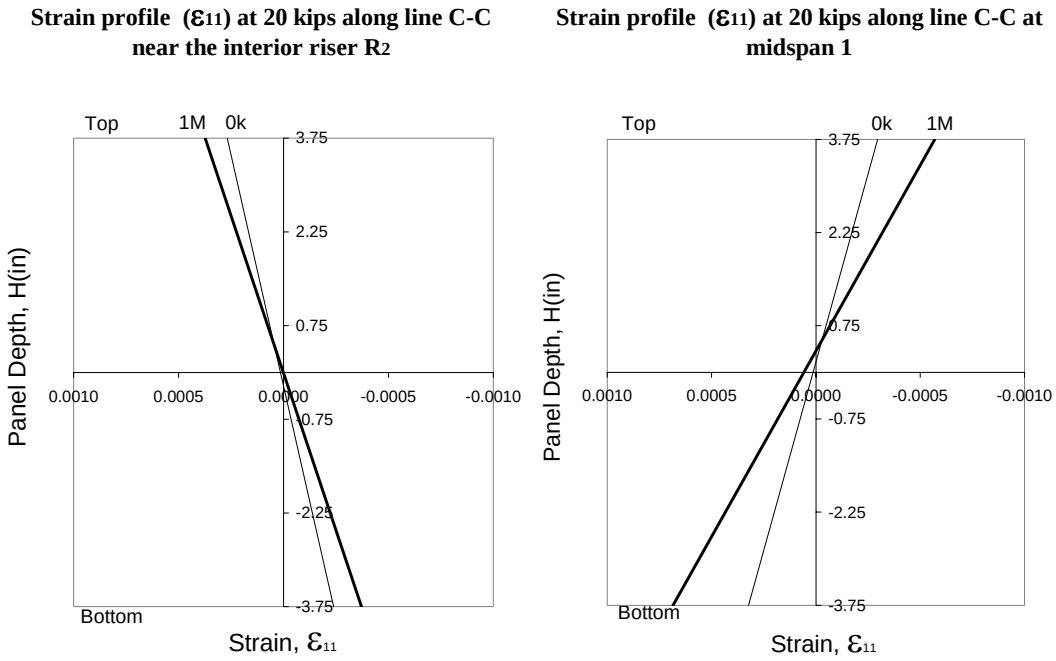

Figure 7-23 Strain profiles in Span 1

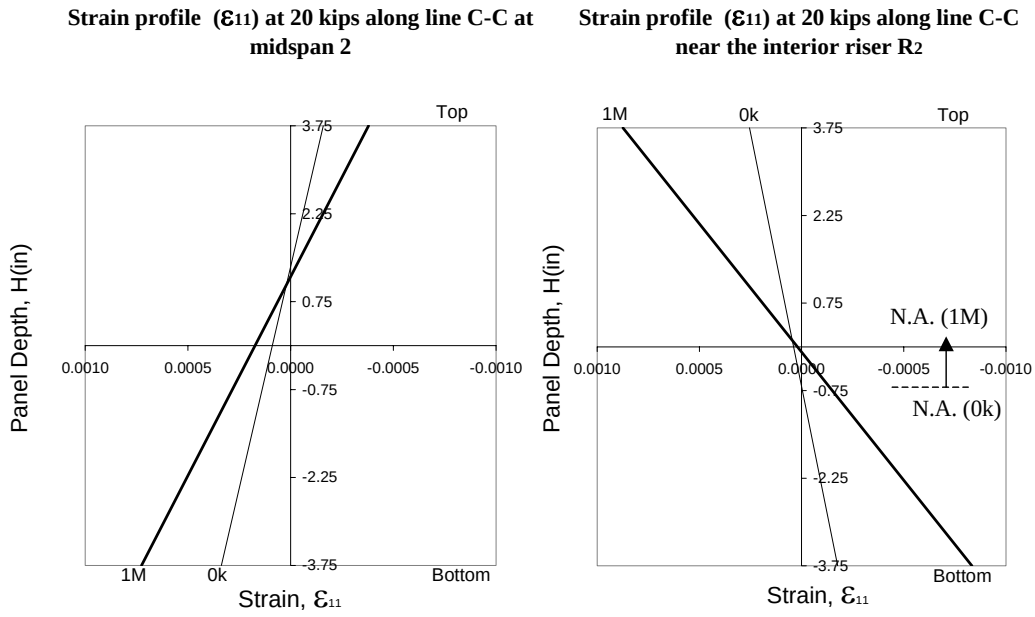

Figure 7-24 Strain profiles in Span 2

Figure 7-24 indicates that, near the interior riser, the top face was carrying less load than the bottom face at the initial static test and that the two faces were carrying the same amount of load at 1,000,000 cycles. This indicates that the bottom face could have delaminated after the fatigue load cycles.

At 1,500,000 cycles, Span 1 started emitting a strong noise. Then, a static test was performed to evaluate the panel behavior (Static Test 1.5M in Table 7-2). Figure 7-25(a) compares the static load-actuator displacement responses at 1,000,000 and 1,500,000 cycles. The figure does not represent the true flexibility of the panel because the actual displacement includes the flexibility of the steel reaction frame that supported the actuator as well as the support settlements at the risers. The graph is used only to show that the overall stiffness decreased with load cycles. Figure 7-25(b) shows the comparison of the adjusted displacement at the middle of Span 1 at 1,500,000 cycles (1.5M) and the LVDT 8 reading at the initial static test (0k). To find the adjusted midspan displacement, the stiffness of the steel frame is first evaluated by using the initial static test data. Then, using this stiffness the steel frame displacement is calculated and subtracted from the actuator displacement to find the adjusted midspan displacement at 1,500,000 cycles. As shown, the stiffness of Span 1 decreased with increasing loading cycles probably because of the local delamination of the upper face from the core.

Figure 7-26 shows the load-strain curves at 0, 1,000,000 and 1,500,000 cycles. The strain profiles for Span 1 in Figure 7-27 indicate that the neutral axis moved upward from 0 to 1,500,000 cycles indicating that the lower face delaminated from the core.

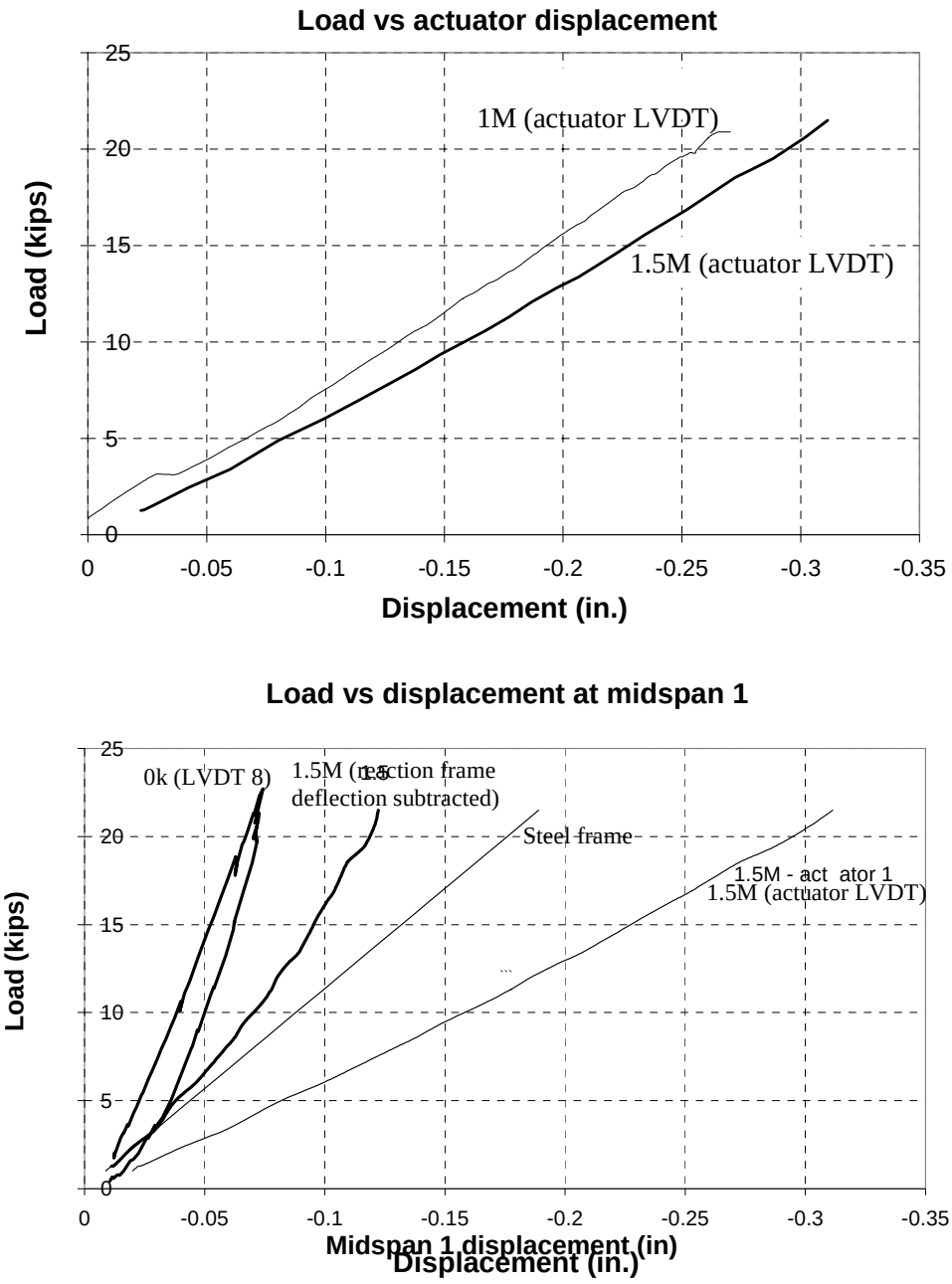

Figure 7-25 Load-displacement curves for Span 1

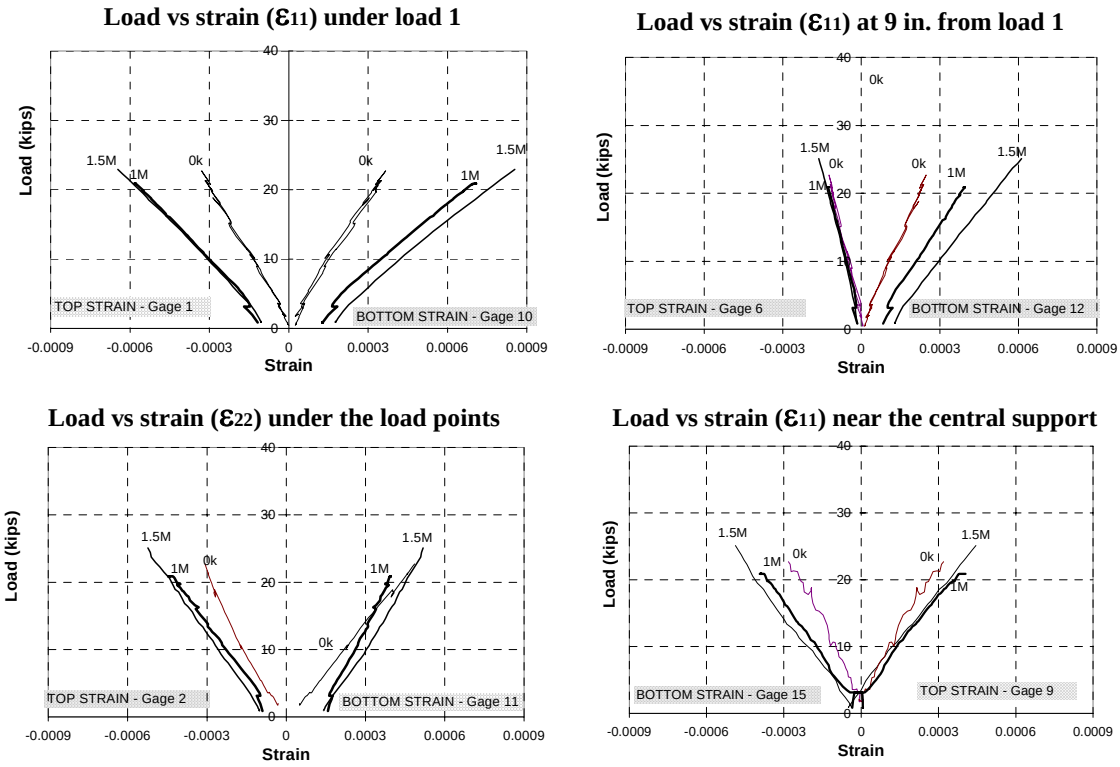

Figure 7-26 Load-strain curves at 1,500,000 cycles for span1

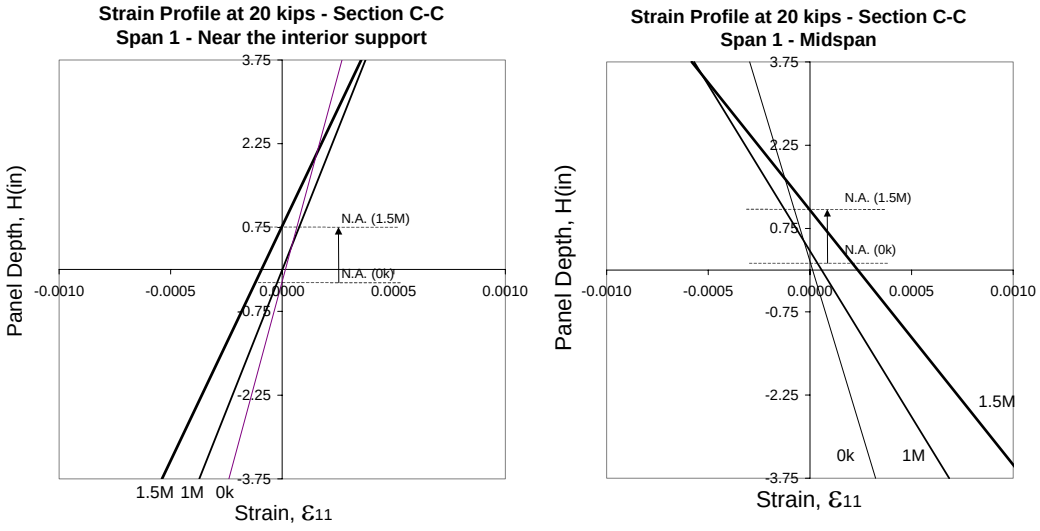

Figure 7-27 Strain profiles at different loading cycles

7.7 Final Static Test

After the fatigue test was completed, the two spans were loaded one at a time up to 100 kips. Figure 7-28 shows the load-actuator displacement response for Span 1. The beams that were tested previously and the panel behaved differently after delamination. For three out of the four beams tested, the failure was brittle. One beam showed a ductile-like behavior because the upper face was not glued uniformly to the core and had progressive delamination. The latter is similar to the panel behavior. In the panel, a crack formed in the face-core interface near the loading plate when the maximum shear stress exceeded the interface shear strength and the crack propagated gradually causing a ductile-like failure.

.

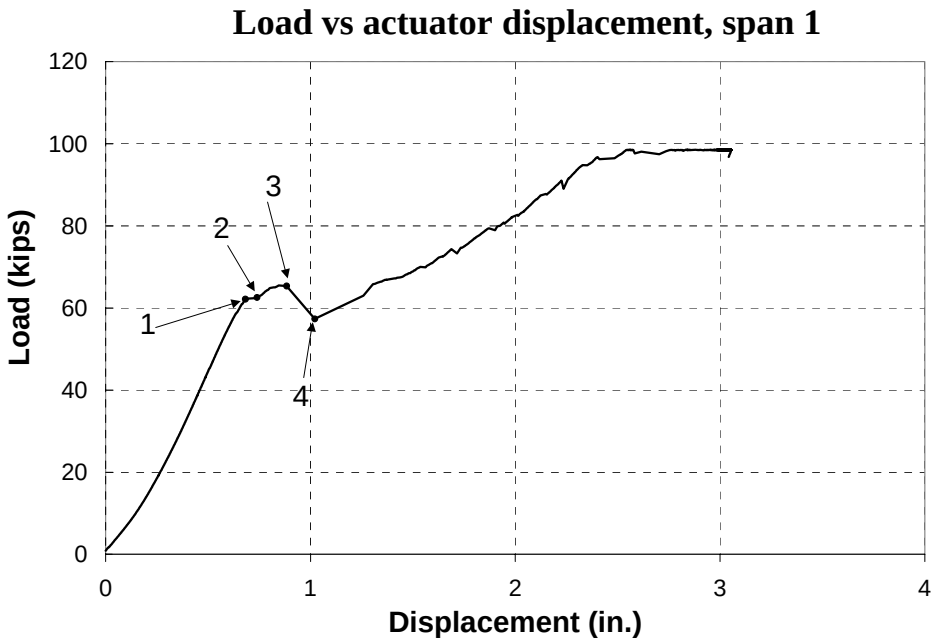

Figure 7-28 Load- actuator displacement curve for Span 1

The strain profiles for Span 1 at different loading stages, 1, 2, 3 and 4 in Figure 7-28, are shown in Figure 7-29 and Figure 7-30. Both strain profiles show that the neutral axis moved downward between stages 1 and 2. This response indicates that the top face delaminated from the core.

Figure 7-29 shows that the strain at the bottom face near the interior riser was zero at stage 2, and the strain became positive at stage 3. Furthermore, at stage 3, the neutral axis near the interior riser was outside of the cross section. This is possible only if there was a horizontal tensile force acting on the panel (see Figure 7-18), which was probably caused by the anchor bolts as explained earlier. Figure 7-30 indicates that between stages 2 and 3, the neutral axis at midspan moved upward confirming that there was a horizontal force acting on the panel.

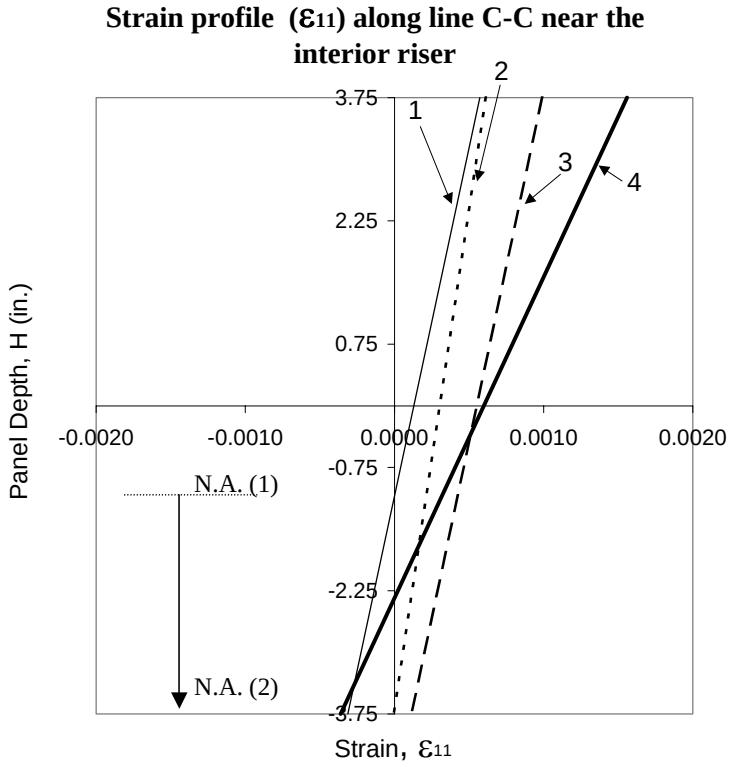

Figure 7-29 Strain profiles in Span 1 near the interior riser at 1,500,000 cycles

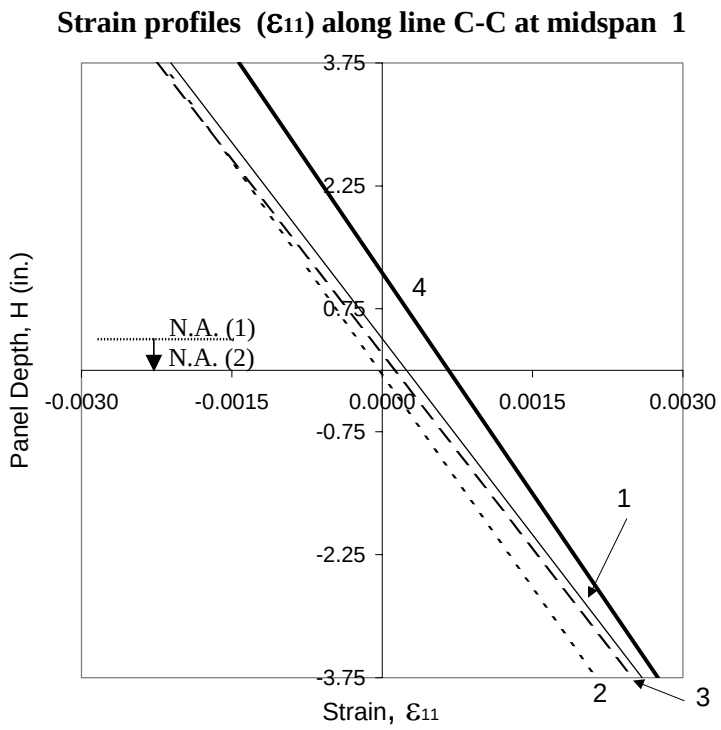

Figure 7-30 Strain profiles at the middle of Span 1 at 1,500,000 cycles

Between stages 3 and 4, the bottom face delaminated and the neutral axis shifted upward at the midspan and near the interior riser as shown in Figure 7-29 and Figure 7-30. The interface delamination was followed by a strong noise emission and a large load drop (stage 3 in Figure 7-28), which indicates a sudden energy release. A visible crack formed in the top face as shown in Figure 7-31. However, even when both faces delaminated, the panel did not collapse but was still carrying load because the damage was localized. This ductile-like behavior is desirable because it gives a warning prior to collapse.

Figure 7-31 shows the loading area under the plate after the test. The crack highlighted in the figure opened at stage 3 and propagated with increasing load. Figure 7-15 shows that the maximum shear strain is near the loading plate edges. The high shear stress, due to the localized bending, exceeded the shear strength of the interface between the core and the face and triggered the formation of the crack near the loading plate edge.

After stage 4, as indicated in Figure 7-28, the load-actuator displacement curve shows small load drops, which were accompanied by noise emissions during the test. This means that the delamination propagated during the test. The figure shows that the damage propagation decreases the panel stiffness.

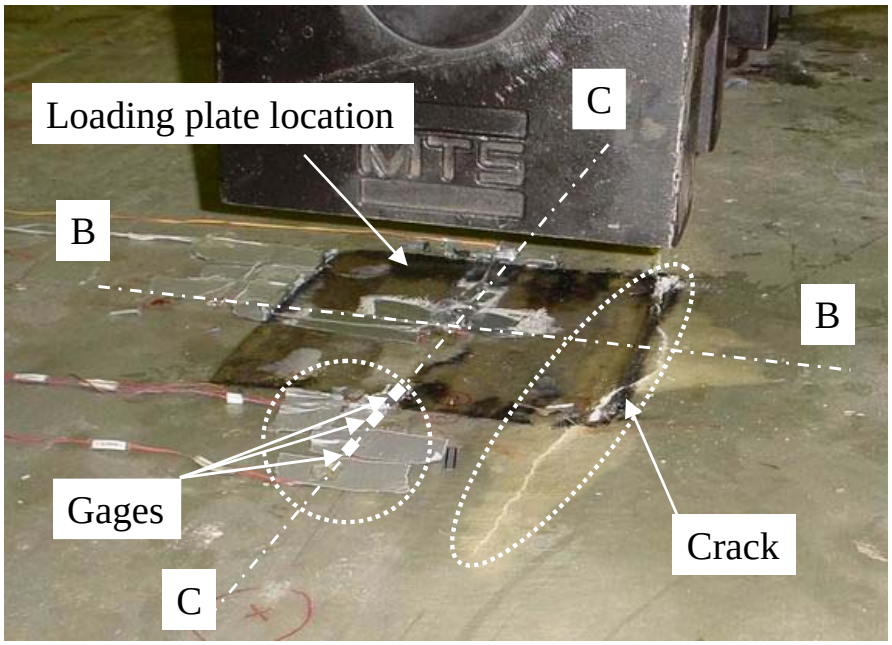

Figure 7-31 Crack located outside the loading plate in Span 1

Figure 7-32 shows the load – actuator displacement curves for both spans. The load – actuator displacement for Span 2 does not show as large a load drop as for Span 1. Probably, the delamination of both faces occurred during the fatigue test, and for this reason, the curve does not show a sudden large load drop. This prior damage caused stiffness reduction as shown in Figure 7-32. The unloading branch indicates that there was a permanent plastic deformation when the panel was completely unloaded.

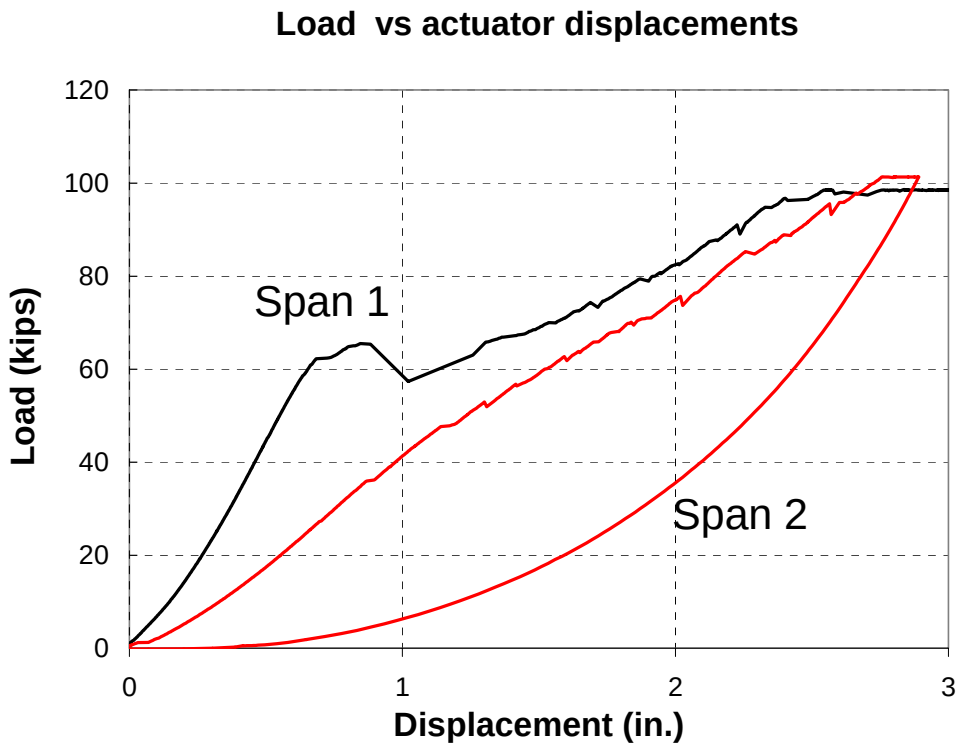

Figure 7-32 Load – actuator displacements for Span 1 and 2

7.8 Final Remarks

The initial static test has indicated that the mechanical anchor that attached the GFRP panel to the concrete supports did not work very well. Some of the anchor bolts on an external support slipped when each of the two spans was subjected to a load up to 22 kips. Because of this observation, the anchor bolts have been switched to epoxy anchor for the O'Fallon Park bridge.

8 ANALYSIS OF PANEL BEHAVIOR USING PLATE THEORY

8.1 Introduction

The Kirchhoff-Love plate theory is used here to analyze a GFRP panel that has the same cross-sectional properties as the O'Fallon Park deck to gain a better insight of the experimental results. The major drawback of this theory is that it does not take into account the shear deformation. Consequentially, the Kirchhoff-Love theory gives accurate results only if the ratio of the smaller lateral dimension of the plate to its thickness is at least ten (Szilard 1974). In the case of the O'Fallon Park deck, this ratio is only 6.5. Hence, to check the accuracy of the analytical solution, the panel is analyzed in Chapter 9 with the finite element method.

In the actual test, the panel had two spans. However, in the analytical solution, the panel is assumed to be simply supported along two opposite edges and free along the other two for sake of simplicity. The panel model has a span of 48.5 in. (center-to-center distance of the risers in the original test panel) and a variable width, *b*, as shown in Figure 8-1.

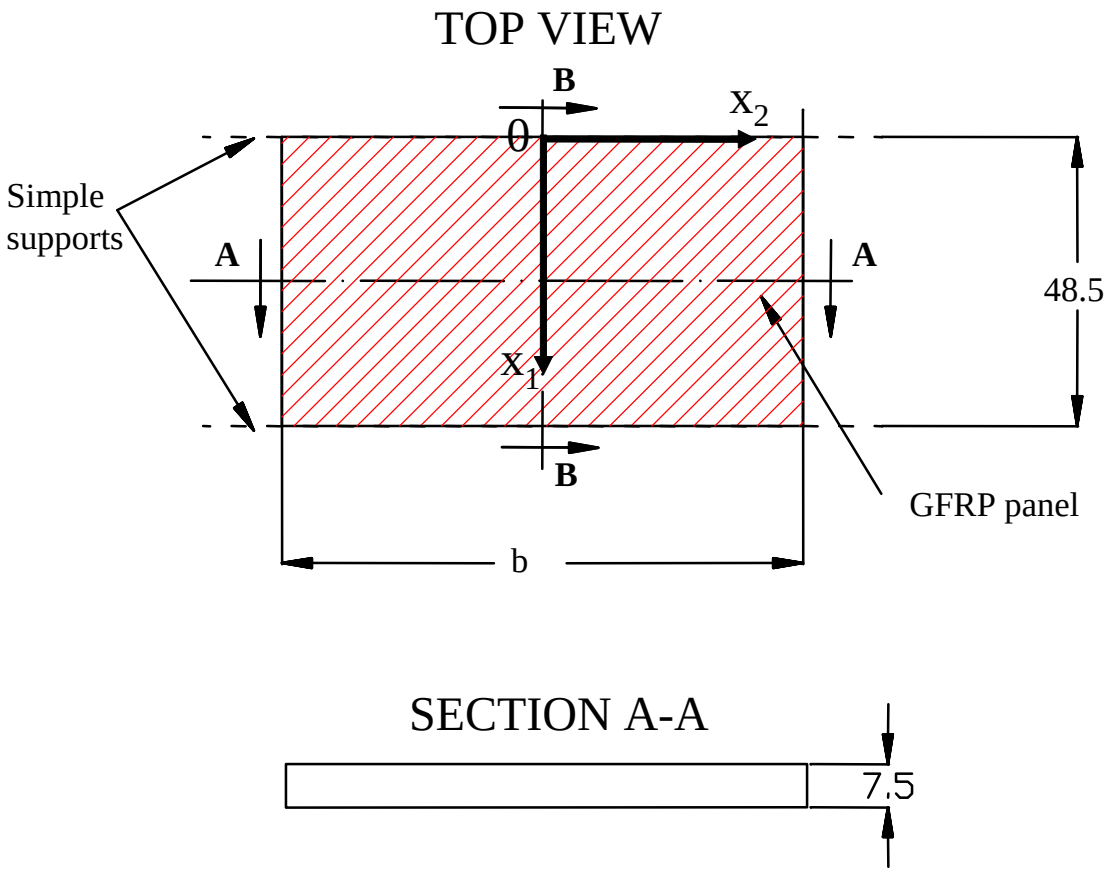

Figure 8-1 Dimensions of the panel model used in the analysis

8.2 Kirchhoff-Love Plate Theory

8.2.1 Differential Equation for Plate Deflection

The Kirchhoff-Love plate theory is based on the following assumptions and conditions (Szilard 1974):

1. The material of the plate is elastic and homogeneous.
2. The plate is initially flat.
3. The slopes of the deflected middle surface are small compared to unity.
4. The deflection of the plate is represented by the displacement of the middle surface normal to its plane.
5. The stresses normal to the middle surface are negligible.

6. The deflection is small compared to the plate thickness. The maximum deflection is less than one fiftieth of the smaller span length.
7. The thickness of the plate is small compared to the other dimensions. The smaller lateral dimension of the plate is at least ten times larger than its thickness.
8. During loading, plane sections remain plane; the deformation due to transverse shear is neglected.

The first six assumptions are valid for the panel studied here. However, the ratio of the smaller lateral dimension to the thickness is only 6.5, and, hence, condition 7 does not apply here. As a consequence, the shear deformation cannot be neglected, and, therefore, assumption 8 is not valid. In spite of this, the Kirchhoff-Love plate theory is used here for the sake of simplicity and with an intention of checking its accuracy for the thick panel considered here using a finite element model. It can be used to develop a better understanding of the behavior of the panel and the influence of the orthotropy introduced by the honeycomb construction.

To set up the orthotropic plate equation based on the Kirchhoff-Love theory, it is necessary to follow these steps:

1. Consider the equilibrium of the external and internal forces acting on the plate.
2. Use an orthotropic elastic material law to link strains to stresses.
3. Express the strains and stresses as functions of the displacement.
4. Express the internal forces as functions of the displacement.

1. Equilibrium

By using the Cartesian coordinate system shown in Figure 8-2 and assuming that the plate is subjected only to lateral forces, it is possible to write the following equilibrium equations:

$$\sum M_{x1} = 0 \quad \sum M_{x2} = 0 \quad \sum F_{x3} = 0 \tag{8.1}$$

The behavior of a plate is analogous to that of a two-dimensional gridwork of beams. Thus, the external load P_{x3} is carried by V_{x1} and V_{x2}, transverse shear forces, and by M_{x1} and M_{x2}, bending moments. Furthermore, plates are characterized by the presence of the twisting moments M_{x1x2} and M_{x2x1}. It is customary in plate theory to use internal forces and internal moments per unit length of a plate, i.e., m_{x1}, m_{x2}, m_{x1x2}, m_{x2x1}, v_{x1} and v_{x2}, as shown in Figure 8-2.

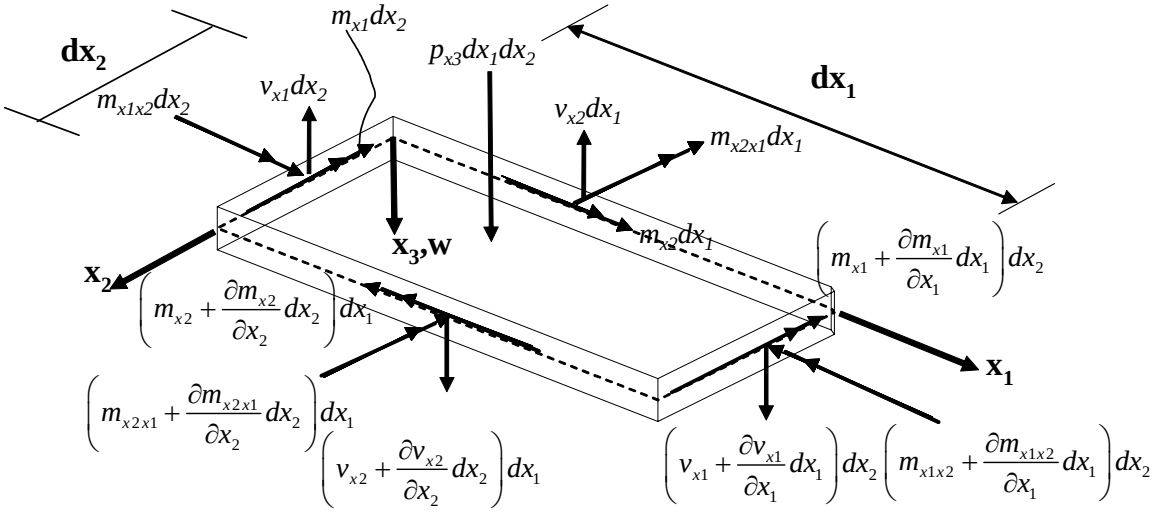

Figure 8-2 Internal moments and forces acting on a plate element

After some simplifications, the equilibrium of internal and external forces acting on a plate element leads to the following equations:

$$\frac{\partial m_{x1}}{\partial x_1} + \frac{\partial m_{x1x2}}{\partial x_2} = v_{x1} \quad \textit{from the sum of moments around the } x_2 \textit{ axis} \tag{8.2}$$

$$\frac{\partial m_{x2}}{\partial x_2} + \frac{\partial m_{x1x2}}{\partial x1} = v_{x2} \quad \textit{from the sum of moments around the } x_1 \textit{ axis} \tag{8.3}$$

$$\frac{\partial v_{x1}}{\partial x_1} + \frac{\partial v_{x2}}{\partial x_2} = -p_{x3} \quad \textit{from the sum of all forces in the } x_3 \textit{ direction} \tag{8.4}$$

Substituting equations (8.2) and (8.3) into (8.4) and noting that $m_{x1x2}=m_{x2x1}$ leads to the following differential equation:

$$\frac{\partial^2 m_{x1}}{\partial x_1^{\,2}} + 2\frac{\partial^2 m_{x1x2}}{\partial x_1 \partial x_2} + \frac{\partial^2 m_{x2}}{\partial x_2^{\,2}} = -p_{x3}(x_1, x_2) \tag{8.5}$$

2. Orthotropic stress-strain Law

In the case of plane stress, five elastic constants are necessary for the description of the orthotropic stress-strain relations:

$$\varepsilon_{11} = \frac{\sigma_{11}}{E_{11}} - \upsilon_{21}\frac{\sigma_{22}}{E_{22}} \tag{8.6}$$

$$\varepsilon_{22} = \frac{\sigma_{22}}{E_{22}} - \upsilon_{12}\frac{\sigma_{11}}{E_{11}}$$

$$\gamma_{12} = \frac{\tau_{12}}{G_{12}}$$

Inverting equation (8.6), we can express the stresses in term of strains:

$$\sigma_{11} = \frac{E_{11}}{1-\upsilon_{12}\upsilon_{21}}(\varepsilon_{11} + \upsilon_{21}\varepsilon_{22}) \tag{8.7}$$

$$\sigma_{11} = \frac{E_{22}}{1-\upsilon_{12}\upsilon_{21}}(\varepsilon_{22} + \upsilon_{12}\varepsilon_{11})$$

$$\tau_{12} = G_{12}\gamma_{12}$$

3. Relation between strains and displacement

By using the compatibility condition, it is possible to express the strains in terms of the displacement:

$$\varepsilon_{11} = -x_3\frac{\partial^2 w}{\partial x_1^2} = x_3\kappa_{x1} \tag{8.8}$$

$$\varepsilon_{22} = -x_3\frac{\partial^2 w}{\partial x_2^2} = x_3\kappa_{x2}$$

$$\gamma_{12} = -2x_3\frac{\partial^2 w}{\partial x_1 \partial x_2} = 2x_3\chi$$

where w is the displacement in the x_3 direction as defined in Figure 8-2, the κ'*s* are the curvatures, and χ is the warping of the plate.

4. Internal force-displacement relations

By integrating the stress components along the plate thickness *H*, the bending and twisting moments are given by:

$$m_{x1} = \int_{-H/2}^{H/2} \sigma_{11} x_3 dx_3 \tag{8.9}$$

$$m_{x2} = \int_{-H/2}^{H/2} \sigma_{22} x_3 dx_3$$

$$m_{x1x2} = m_{x2x1} = \int_{-H/2}^{H/2} \tau_{12} x_3 dx_3$$

Substituting equations (8.7) and (8.8) into (8.9), the moments can be expressed in terms of displacement, *w*:

$$m_{x1} = -D_{11}\left(\frac{\partial^2 w}{\partial x_1^{\,2}} + \upsilon_{21}\frac{\partial^2 w}{\partial x_2^{\,2}}\right) \tag{8.10}$$

$$m_{x2} = -D_{22}\left(\frac{\partial^2 w}{\partial x_2^{\,2}} + \upsilon_{12}\frac{\partial^2 w}{\partial x_1^{\,2}}\right)$$

$$m_{x1x2} = -2D_t\frac{\partial^2 w}{\partial x_1 \partial x_2}$$

where D_{11} and D_{22} are the flexural rigidities of an orthotropic plate, and $2D_t = (1-\upsilon_{12})D_{12}$ represents the torsional rigidity. For a plate with a uniform thickness,

$$D_{11} = \frac{E_{11}H^3}{12(1-\nu_{12}^{\,2})} \tag{8.11}$$

$$D_{22} = \frac{E_{22}H^3}{12(1-\nu_{21}^{\,2})} \tag{8.12}$$

$$D_t = G_{12}\frac{H^3}{12} \tag{8.13}$$

Finally, the substitution of equation (8.10) into (8.5) yields the governing differential equation for orthotropic plates:

$$D_{11}\frac{\partial^4 w}{\partial x_1^{\,4}} + 2B\frac{\partial^4 w}{\partial x_1^{\,2}\partial x_2^{\,2}} + D_{22}\frac{\partial^4 w}{\partial x_2^{\,4}} = p_{x_3}(x_1, x_2) \tag{8.14}$$

where B is the effective torsional rigidity:

$$B = \frac{1}{2}\left(\upsilon_{21}D_{11} + \upsilon_{12}D_{22} + 4D_t\right) \tag{8.15}$$

An exact solution of the governing differential equation, equation (8.14), must satisfy the plate boundary conditions. For rectangular plates subjected to lateral loads, the Levi's

and Navier's methods are most commonly used to solve equation (8.14).

8.2.2 Levi's Method

Levi developed a method to solve equation (8.14) for linear elastic plates. This section presents the solution for isotropic plates and the extended solution for orthotropic plates. Figure 8-3 shows the boundary conditions assumed in the solution.

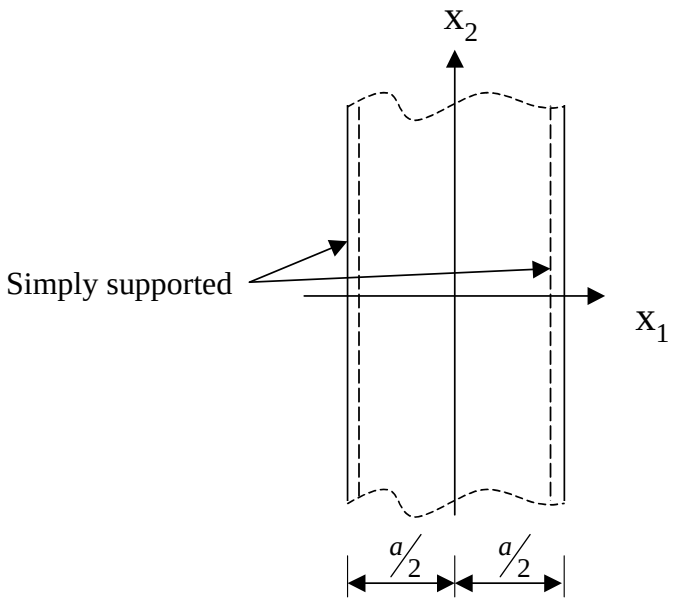

Figure 8-3 Coordinate system and boundary conditions

Levi first solved the homogeneous biharmonic differential equation, which represents the governing differential equation for an unloaded plate:

$$D_{11}\frac{\partial^4 w}{\partial x_1^{\,4}} + 2B\frac{\partial^4 w}{\partial x_1^{\,2}\partial x_2^{\,2}} + D_{22}\frac{\partial^4 w}{\partial x_2^{\,4}} = 0 \tag{8.16}$$

A solution of equation (8.16) can be found to have the following form:

$$w_H(x_1, x_2) = X_1(x_1) \bullet X_2(x_2) \tag{8.17}$$

By using a single Fourier series, a solution that satisfies the boundary conditions and equation (8.16) is:

$$w_H(x_1, x_2) = \sum_{m=1}^{\infty} X_{2m}(x_2) \sin \frac{m\pi x_1}{a} \tag{8.18}$$

Substituting (8.18) into (8.16), we have

$$D_{11} \frac{m^4 \pi^4}{a^4} X_{2m} - 2B \frac{m^2 \pi^2}{a^2} X^{II}_{2m} + D_{22} X^{IV}_{2m} = 0 \tag{8.19}$$

In equation (8.19), X^{II} and X^{IV} are the second derivative and fourth derivative of the function *X*, respectively. The solution of equation (8.19) is of the form:

$$X_{2m} = Ge^{rx_2} \tag{8.20}$$

where *G* is a constant and *r* are the four roots of the corresponding characteristic equation:

$$r_{1,2,3,4} = \pm \frac{m\pi}{a} \sqrt{\frac{B}{D_{22}} \pm \sqrt{\frac{B^2}{D_{22}^2} - \frac{D_{11}}{D_{22}}}} \tag{8.21}$$

By defining (Timoshenko and Woinowsky-Krieger 1974)

$$\mu = \frac{B}{\sqrt{D_{11} D_{22}}} \tag{8.22}$$

we obtain three different cases for the solution of equation (8.16):

1. Two double real roots if $\mu = 1$, i.e., $B = \sqrt{D_{11} D_{22}}$ (8.23)
2. Four complex roots if $\mu < 1$, i.e., $B < \sqrt{D_{11} D_{22}}$
3. Four real roots if $\mu > 1$, i.e., $B > \sqrt{D_{11} D_{22}}$

It should be noticed that the first case represents an isotropic case.

In this study, to compare an isotropic plate with an orthotropic plate, both cases 1 and 2 are considered. The orthotropic solution uses the material properties given in Table 8-1. The values in Table 8-1 are obtained by modeling a 7.5-in. honeycomb sandwich panel as a three layer laminate and using the classical lamination theory (Daniel and Ishai 1994) using the material properties shown in Table 3-2. The isotropic solution is based

on the elastic modulus, E_{11}, as well as the shear modulus, G_{12}, and Poisson Ratio, υ_{12}, shown in Table 8-1.

Table 8-1 Equivalent stiffness properties of GFRP honeycomb sandwich panel

Elastic Moduli (ksi)			Poisson Ratio
E_{11}	E_{22}	G_{12}	ν_{12}
827	503	148	0.302

Substituting the values given in Table 8-1 in equations (8.11) and (8.12), we have μ = 0.66. Thus, the solution for the orthotropic sandwich panel considered here is represented by case 2.

Case1: Isotropic plates

In this case, $D_{11}=D_{22}=D$ and $\mu=1$. Hence, equation (8.19) can be simplified as:

$$X_{2m}^{IV}+2\frac{m^2\pi^2}{a^2}X_{2m}^{II}+\frac{m^4\pi^4}{a^4}X_{2m}=0 \tag{8.24}$$

The solution of equation (8.24) has the following form:

$$X_{2m}=A_m e^{\frac{m\pi x_2}{a}}+B_m\frac{m\pi x_2}{a}e^{\frac{m\pi x_2}{a}}+C_m e^{\frac{-m\pi x_2}{a}}+D_m\frac{m\pi x_2}{a}e^{\frac{-m\pi x_2}{a}} \tag{8.25}$$

Observing that the deflection and its derivatives approach zero at a large distance from the x_1 axis, we have $A_m=B_m=0$. Therefore, the solution of equation (8.16) can be represented by the following sine series:

$$w_H(x_1,x_2)=\sum_{m=1}^{\infty}(C_m+D_m\frac{m\pi x_2}{a})e^{\frac{-m\pi x_2}{a}}\sin\frac{m\pi x_1}{a} \tag{8.26}$$

Exploiting the condition of symmetry, i.e., $\left(\frac{\partial w}{dx_2}\right)_{x_2=0}=0$, we have $C_m=D_m$. Therefore, we can write equation (8.26) in the following form:

$$w_H(x_1,x_2)=\sum_{m=1}^{\infty}C_m(1+\frac{m\pi x_2}{a})e^{\frac{-m\pi x_2}{a}}\sin\frac{m\pi x_1}{a} \tag{8.27}$$

The above equation can be used to calculate the deflection of a plate at a point outside the loading area. Consider the case of a uniformly distributed line load of intensity p_0 over a length c along the x_1 axis as shown in Figure 8-4. The load distribution can be represented by a trigonometric series and the constants of the Fourier expansion of the load are given as:

$$p_m = \frac{2p_0}{a}\int_{\xi_1 - c/2}^{\xi_1 + c/2} \sin\frac{m\pi x_1}{a}\,dx_1 = \frac{4p_0}{m\pi}\sin\frac{m\pi\xi_1}{a}\sin\frac{m\pi c}{2a} \tag{8.28}$$

The load can then be expressed in form of a sine series as:

$$p = \frac{4p_0}{\pi}\sum_{m=1}^{\infty}\frac{1}{m}\sin\frac{m\pi\xi_1}{a}\sin\frac{m\pi c}{2a}\sin\frac{m\pi x_1}{a} \tag{8.29}$$

Since the load is equally divided between the two halves of the plate, it follows that

$$\begin{aligned}(v_{x_2})_{x_2=0} &= -D\frac{\partial}{\partial x_2}\left(\frac{\partial^2 w}{\partial {x_1}^2} + \frac{\partial^2 w}{\partial {x_2}^2}\right)_{x_2=0} \\ &= -\frac{2p_0}{\pi}\sum_{m=1}^{\infty}\frac{1}{m}\sin\frac{m\pi\xi_1}{a}\sin\frac{m\pi c}{2a}\sin\frac{m\pi x_1}{a}\end{aligned} \tag{8.30}$$

The substitution of equation (8.27) for w in equation (8.30) gives:

$$\frac{2D\pi^3}{a^3}\sum_{m=1}^{\infty}C_m m^3\frac{m\pi x_1}{a} = \frac{2p_0}{\pi}\sum_{m=1}^{\infty}\frac{1}{m}\sin\frac{m\pi\xi_1}{a}\sin\frac{m\pi c}{2a}\sin\frac{m\pi x_1}{a} \tag{8.31}$$

Therefore, C_m is obtained as

$$C_m = \frac{p_0 a^3}{Dm^4\pi^4}\sin\frac{m\pi\xi_1}{a}\sin\frac{m\pi c}{2a} \tag{8.32}$$

The deflection of the plate outside the loading area is obtained by substituting C_m into equation (8.27):

$$w = \frac{p_0 a^3}{D\pi^4}\sum_{m=1}^{\infty}\frac{1}{m^4}\sin\frac{m\pi\xi_1}{a}\sin\frac{m\pi c}{2a}\left(1+\frac{m\pi x_2}{a}\right)e^{\frac{-m\pi x_2}{a}}\sin\frac{m\pi x_1}{a} \tag{8.33}$$

The previous solution can be used to obtain the deflection of a long plate under a uniform load of intensity p_0 distributed over a rectangular area with sides equal to c and d as shown in Figure 8-5.

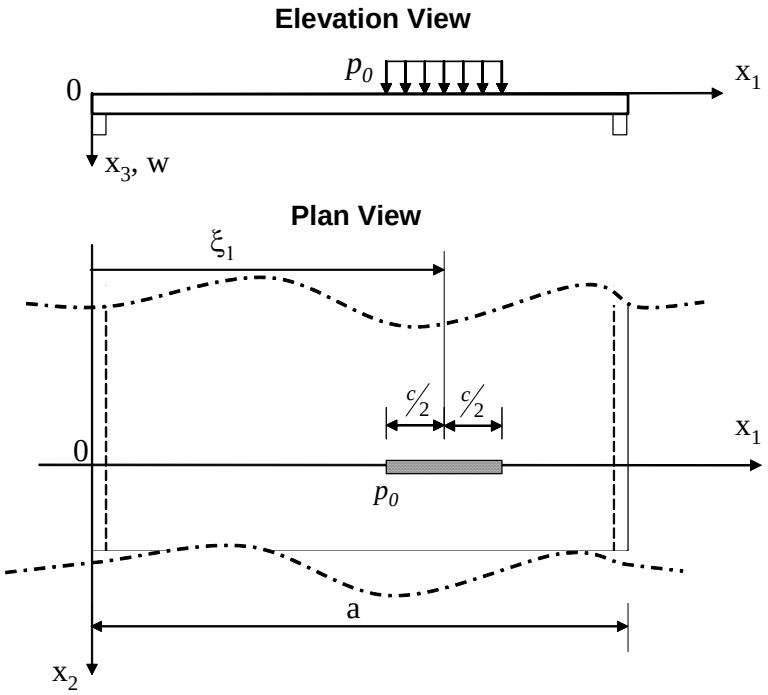

Figure 8-4 Uniform line load condition

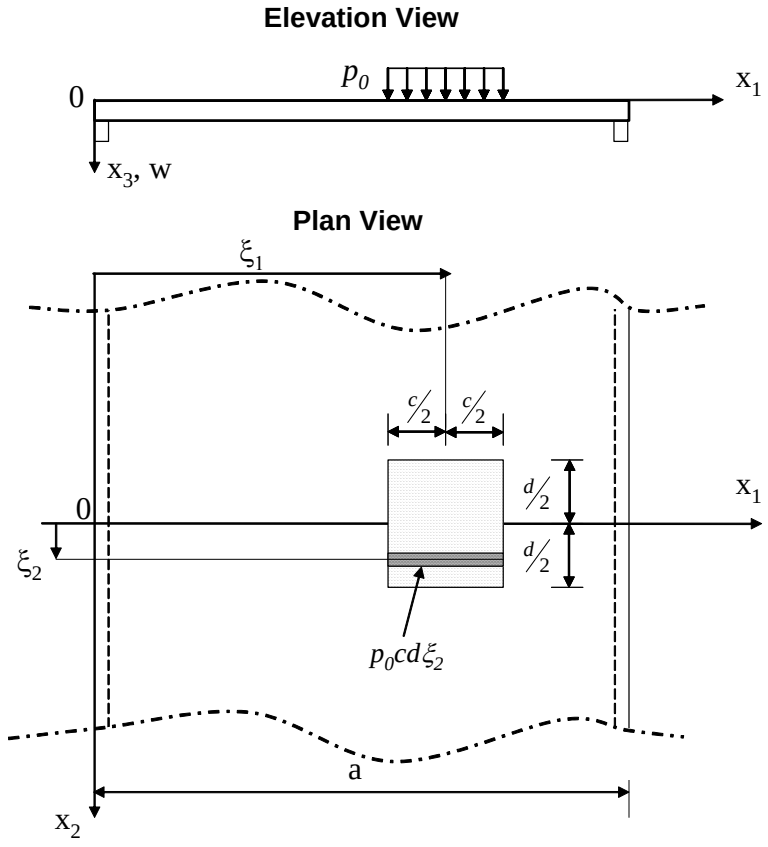

Figure 8-5 Uniform rectangular load

To this end, consider a load of magnitude $p_0 c d\xi_2$ over an infinitesimal area (see Figure 8-5) at a distance ξ_2 from the x_1 axis. The infinitesimal load can be expressed in form of a sine series as:

$$p_0 d\xi_2 = \frac{4p_0}{\pi} d\xi_2 \sum_{m=1}^{\infty} \frac{1}{m} \sin\frac{m\pi\xi_1}{a} \sin\frac{m\pi c}{2a} \sin\frac{m\pi x_1}{a} \tag{8.34}$$

The deflection produced by the infinitesimal load $p_0 d\xi_2$ at points outside the loading area is obtained by substituting $p_0 d\xi_2$ for p_0 and x_2-ξ_2 for x_2 in equation (8.33). The deflection produced by the entire load over the rectangular area is obtained by integrating the resulting equation with respect to ξ_2 from $-d/2$ to $+d/2$:

$$w = \frac{p_0 a^3}{D\pi^4} \sum_{m=1}^{\infty} \frac{1}{m^4} \sin\frac{m\pi\xi_1}{a} \sin\frac{m\pi c}{2a} \sin\frac{m\pi x_1}{a} \times \left[\left(\frac{2a}{m\pi} + x_2 - \frac{d}{2} \right) e^{\frac{-m\pi(2x_2 - d)}{2a}} - \left(\frac{2a}{m\pi} + x_2 + \frac{d}{2} \right) e^{\frac{-m\pi(2x_2 + d)}{2a}} \right] \tag{8.35}$$

The above equation is applicable to plate deflection outside the loading area.

Case 2: Orthotropic plates

The solution for an orthotropic plate can be found with a similar procedure used for the isotropic case. By defining the following parameters (Timoshenko and Woiwonowksi-Krieger 1974):

$$\lambda = \sqrt[4]{\frac{D_{22}}{D_{11}}} \qquad \alpha = \frac{a\lambda}{\pi} \sqrt{\mu + \sqrt{\mu^2 - 1}} \qquad \beta = \frac{a\lambda}{\pi} \sqrt{\mu - \sqrt{\mu^2 - 1}} \tag{8.36}$$

the solution of equation (8.19) has the following form:

$$X_{2m} = A_m e^{\frac{mx_2}{\alpha}} + B_m e^{\frac{mx_2}{\beta}} + C_m e^{\frac{-mx_2}{\alpha}} + D_m e^{\frac{-mx_2}{\beta}} \tag{8.37}$$

By observing that the deflection and its derivatives approach zero at a large distance from the x_1 axis, we have A_m=B_m=*0* and equation (8.37) can be simplified as

$$X_{2m} = C_m e^{\frac{-mx_2}{\alpha}} + D_m e^{\frac{-mx_2}{\beta}} \tag{8.38}$$

Equation (8.18) becomes:

$$w_H(x_1,x_2)=\sum_m^{\infty}\left(C_m e^{\frac{-mx_2}{\alpha}}+D_m e^{\frac{-mx_2}{\beta}}\right)\sin\frac{m\pi x_1}{a} \tag{8.39}$$

From symmetry, it can be concluded that along the x_1 axis, $\left(\frac{\partial w}{dx_2}\right)_{x_2=0}=0$. Hence, $D_m=-\frac{\beta}{\alpha}C_m$ and we can write equation (8.39) in the form:

$$w_H(x_1,x_2)=\sum_m^{\infty}C_m\left(e^{\frac{-mx_2}{\alpha}}-\frac{\beta}{\alpha}e^{\frac{-mx_2}{\beta}}\right)\sin\frac{m\pi x_1}{a} \tag{8.40}$$

Consider the case of a uniformly distributed line load of intensity p_0 over a length c along the x_1 axis as shown in Figure 8-4. The load distribution can be represented by a trigonometric series and the constants of the Fourier expansion of the load are given as:

$$p_m=\frac{2p_0}{a}\int_{\xi_1-c/2}^{\xi_1+c/2}\sin\frac{m\pi x_1}{a}dx_1=\frac{4p_0}{m\pi}\sin\frac{m\pi\xi_1}{a}\sin\frac{m\pi c}{2a} \tag{8.41}$$

The load can then be expressed in form of a sine series as:

$$p=\frac{4p_0}{\pi}\sum_{m=1}^{\infty}\frac{1}{m}\sin\frac{m\pi\xi_1}{a}\sin\frac{m\pi c}{2a}\sin\frac{m\pi x_1}{a} \tag{8.42}$$

Since the load is equally divided between the two halves of the plate, it follows that

$$\begin{aligned}(v_{x_2})_{x_2=0}&=-\frac{\partial}{\partial x_2}\left(D_{22}\frac{\partial^2 w}{\partial x_2^{\,2}}+B\frac{\partial^2 w}{\partial x_1^{\,2}}\right)_{x_2=0}\\&=-\frac{2p_0}{\pi}\sum_{m=1}^{\infty}\frac{1}{m}\sin\frac{m\pi\xi_1}{a}\sin\frac{m\pi c}{2a}\sin\frac{m\pi x_1}{a}\end{aligned} \tag{8.43}$$

The constant C_m can be found by substituting equation (8.40) into (8.43)

$$C_m=\frac{\alpha p_0 a^4}{2\pi^4 m^3 D_{11}\left(\alpha^2-\beta^2\right)} \tag{8.44}$$

Therefore, equation (8.40) becomes

$$w_H(x_1,x_2)=\sum_m^{\infty}\frac{\alpha p_0 a^4}{2\pi^4 m^3 D_{11}\left(\alpha^2-\beta^2\right)}\left(e^{\frac{-mx_2}{\alpha}}-\frac{\beta}{\alpha}e^{\frac{-mx_2}{\beta}}\right)\sin\frac{m\pi x_1}{a} \tag{8.45}$$

The above equation can be extended to find the deflection of a plate due to a load uniformly distributed over a rectangular area as shown in Figure 8-5. The deflection produced by the infinitesimal load $p_0 d\xi_2$ at points outside the loading area is obtained by substituting $p_0 d\xi_2$ for p_0 and x_2-ξ_2 for x_2 in equation (8.45). The deflection produced by the entire load over the rectangular area is obtained by integrating the resulting equation with respect to ξ_2 from $-d/2$ to $+d/2$:

$$w = \frac{p_0 a^2}{\pi^3 \sqrt{D_{11} D_{22}}} \sum_{m=1}^{\infty} \frac{1}{m^4} \sin\frac{m\pi\xi_1}{a} \sin\frac{m\pi c}{2a} \times \left[\left(\alpha_0 \sin\frac{mx_2}{\alpha_0} + \beta_0 \cos\frac{mx_2}{\beta_0} \right) e^{\frac{-mx_1}{\beta_0}} \right] \sin\frac{m\pi x_1}{a} \tag{8.46}$$

where α_0 and β_0 are defined as:

$$\alpha_0 = \frac{a\lambda}{\pi}\sqrt{\frac{2}{1-\mu}} \qquad \beta_0 = \frac{a\lambda}{\pi}\sqrt{\frac{2}{1+\mu}} \tag{8.47}$$

The above equation is applicable to plate deflection outside the loading area.

8.2.3 Navier's Solution

Navier obtained the solution for the governing differential equation, equation (8.14), for a plate with four simply supported edges and subjected to a transverse loading by expanding the displacement and the lateral load into double sine series:

$$w(x_1, x_2) = \sum_{m=1}^{\infty}\sum_{n=1}^{\infty} W_{mn} \sin\frac{m\pi x_1}{a} \sin\frac{n\pi x_2}{b} \tag{8.48}$$

$$p_{x3}(x_1, x_2) = \sum_{m=1}^{\infty}\sum_{n=1}^{\infty} P_{mn} \sin\frac{m\pi x_1}{a} \sin\frac{n\pi x_2}{b} \tag{8.49}$$

where a and b are the dimensions of the plate in the x_1 and x_2 directions, as shown in Figure 8-6.

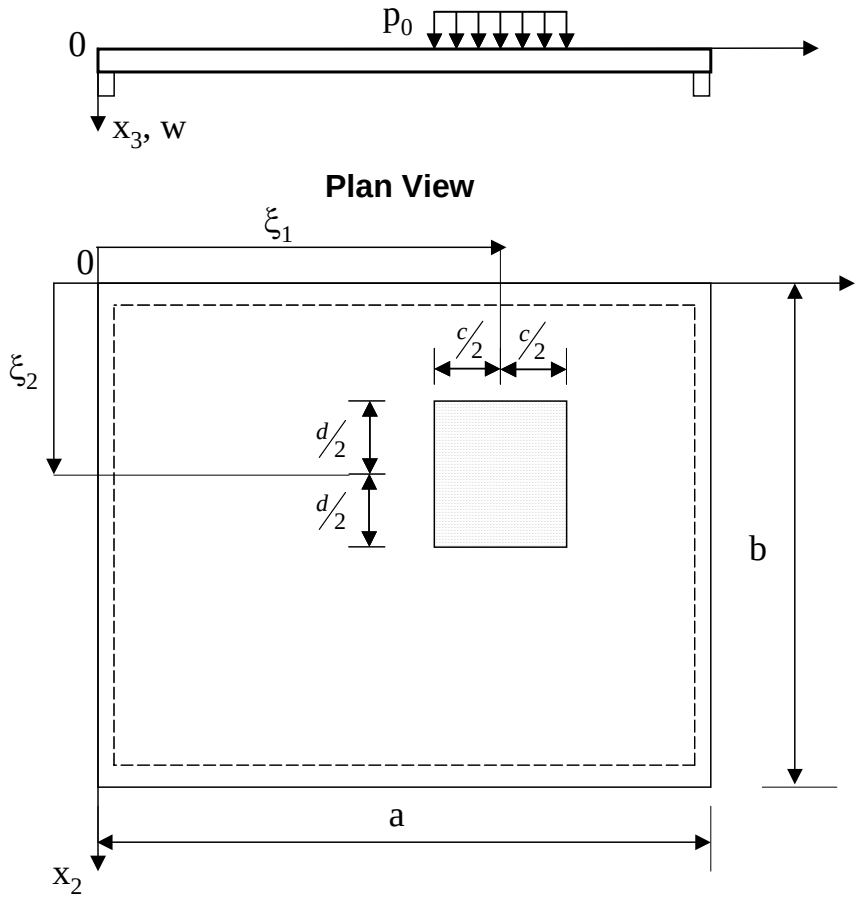

Figure 8-6 Coordinate system and boundary conditions for Navier's method

It should be noted that equations (8.48) and (8.49) satisfy the boundary conditions of the problem. The unknown W_{mn} can be calculated by substituting equations (8.48) and (8.49) into (8.14) and then solving for W_{mn}:

$$W_{mn} = \frac{P_{mn}}{\pi^4\left(D_{11}\frac{m^4}{a^4} + 2B\frac{m^2n^2}{a^2b^2} + D_{22}\frac{n^4}{b^4}\right)} \tag{8.50}$$

By substituting (8.50) into (8.48), an analytical solution for the deflection of an orthotropic plate is obtained as follows:

$$w(x_1, x_2) = \frac{1}{\pi^4}\sum_{m=1}^{\infty}\sum_{n=1}^{\infty}\frac{P_{mn}}{\left(D_{11}\frac{m^4}{a^4} + 2B\frac{m^2n^2}{a^2b^2} + D_{22}\frac{n^4}{b^4}\right)}\sin\frac{m\pi x_1}{a}\sin\frac{n\pi x_2}{b} \tag{8.51}$$

The coefficients P_{mn} for the rectangular load shown in Figure 8-6 are obtained from:

$$P_{mn} = \frac{4p_0}{ab}\int_{\xi_2+d/2}^{\xi_2+d/2}\int_{\xi_1+c/2}^{\xi_1+c/2}\sin\frac{m\pi x_1}{a}\sin\frac{n\pi x_2}{b}dx_1dx_2 \tag{8.52}$$

The displacement $w(x_1,x_2)$ is found by evaluating equation (8.52) and substituting the obtained P_{mn} into equation (8.51). The expressions for the moments are obtained by substituting $w(x_1,x_2)$ into equation (8.10).

The solution for the deflection of an isotropic plate can be found from equation (8.51) by having $D_{11} = D_{22} = D$.

8.3 Analytical Results

Version 4 of the program Mathematica is used to evaluate the Levi's and Navier's solutions for the deflection and internal forces in a honeycomb panel that has the same cross section as the test panel. The coordinates and boundary conditions used in the Levi's solution are shown in Figure 8-5 and those for the Navier's solution are shown in Figure 8-6. The boundary conditions are not exactly the same as those in the test panel for the sake of simplicity. To evaluate the effect of the material orthotropy, the solutions for orthotropic and isotropic plates are compared. The orthotropic solution uses the material properties given in Table 8-1, and the isotropic solution uses only the elastic modulus in the direction x_1 given in Table 8-1.

8.3.1 Results from Levi's solution

For this analysis, the dimensions of the loading area are assumed to be 12x12 in. The span is 48.5 in. The maximum displacement at the center of the panel (i.e. at x_1=24.25 in. and x_2=0 in. in Figure 8-5) due to a load of 26 kips is obtained with equation (8.46) for the orthotropic plate and with equation (8.35) for the isotropic plate. Strictly speaking, equations (8.46) and (8.35) are only applicable to plate deflection outside the loading area. However, the dimensions of the loading area are small compared to the overall plate dimensions. For this reason, this limitation is ignored here. The Levi's solution converges extremely rapidly. The difference in displacement by using five terms

and ten terms of the series is only 0.008%. For most practical purposes, a few terms of the series are sufficient to obtain an accurate solution.

Figure 8-7 shows the displacement along section A-A (Figure 8-1). As expected, the orthotropic panel is softer than the isotropic panel, because the orthotropic panel is weaker in bending about the x_1 axis. The maximum displacement for the orthotropic plate is 26% larger than that for the isotropic plate. Figure 8-7 shows that the displacement along section A-A (Figure 8-1) approaches zero rapidly with increasing distance from the loading plate. This trend is more pronounced for the orthotropic plate. This implies that the load is distributed over a smaller width in the orthotropic plate than in an isotropic plate. For a panel subjected to a 26-kip load, the displacement at 43.75 in. from the center of the load in the direction x_2 is 7.5 times smaller than the maximum displacement. At 90 in. from the center of the load, the displacement is negligible. Figure 8-8 shows the displacement along section B-B (Figure 8-1). The plot again shows the softer behavior of the orthotropic plate.

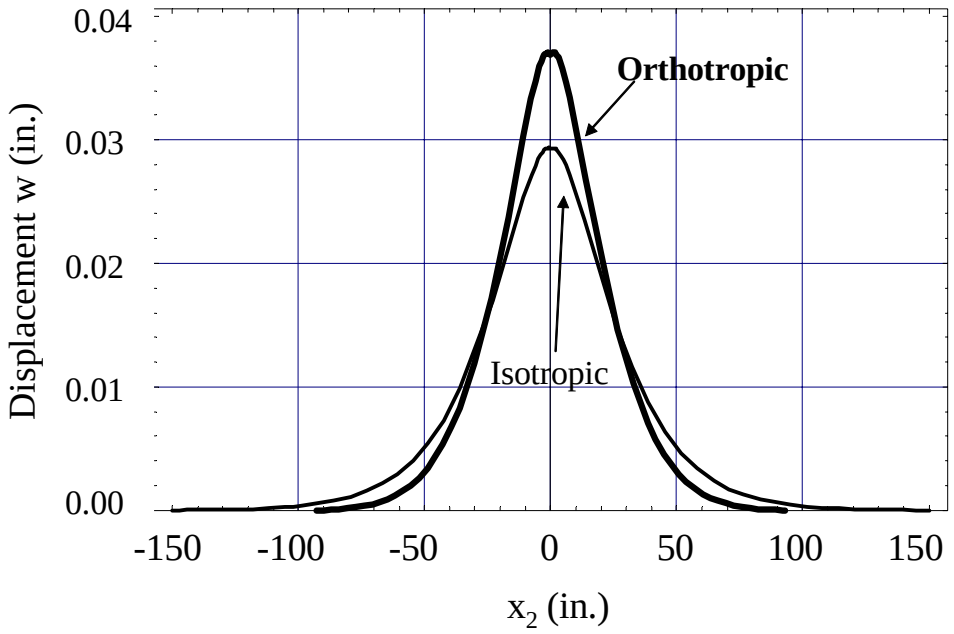

Figure 8-7 Displacement along section A-A at 26 kips

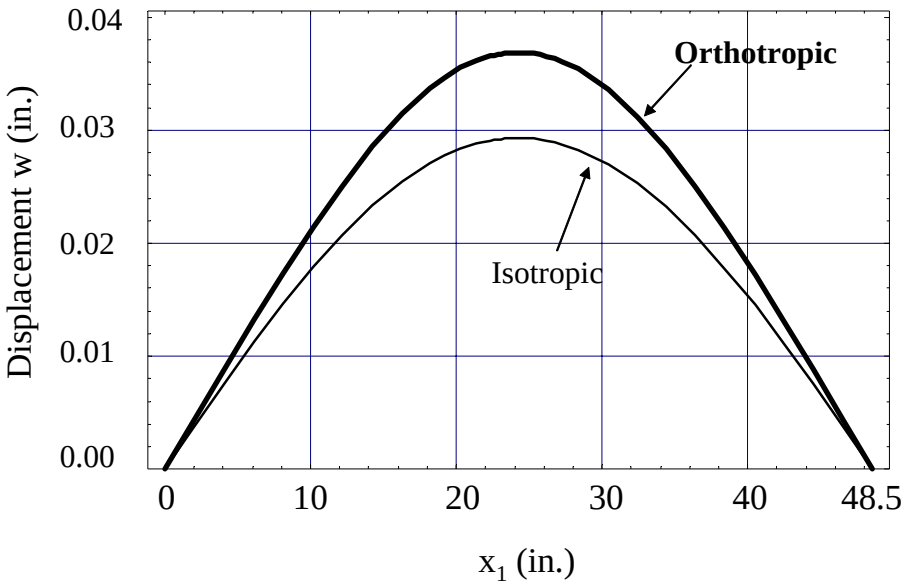

Figure 8-8 Displacement along section B-B at 26 kips

Although the Levi's solution converges extremely fast, it requires very involved mathematical manipulation. This is especially true for the case of orthotropic plates. In addition, the calculation of the derivative of the displacement, which are required to find the internal moments and forces, exhibits convergence problems in vicinity of the center of the load. This is probably due to the fact that equations (8.46) and (8.35) are not valid in the loading area. The Navier's solution is less general and converges less rapidly than the Levi's solution. However, the Navier's method involves simpler mathematical manipulation and the solution found can be used for calculating the plate internal forces in the loaded region. For this reason, the Navier's solution is used to calculate the internal forces and the results are presented in the next section.

8.3.2 Results from Navier's solution

The panel is assumed to be simply supported along four edges. Szilard (1974) claims that the convergence of this solution is relatively fast provided that the ratios *a/c* and *d/b (*where *a, b, c* and *d* are shown in Figure 8-6) are small. Here, *a* is 48.5 in., *d* and *c* are assumed to be 12 in. and *b* is assumed to be 10 times *a*. Further increase of *b* does not lead to a noticeable change of the results. The aim is to simulate a finitely long panel

as provided by the Levi's solution.

Figure 8-9 compares the displacement at 26-kip load along section A-A obtained with the Navier's and Levi's solutions for the orthotropic plate. The Levi's solution is obtained using 5 terms of the series in equation (8.46), whereas the Navier's solution is obtained using 12 terms of the series in equation (8.51). In Figure 8-9, it is not possible to distinguish the two curves because they almost exactly superimpose on each other. The maximum displacements obtained with the Levi's and Navier's solutions at a 26-kip load are 0.037816 and 0.037903 in., respectively. The difference is only 0.64%. Figure 8-10 shows the displacements along section B-B (Figure 8-1) under a 26-kip load from the two solutions. The difference between the two solutions is also negligible along this section.

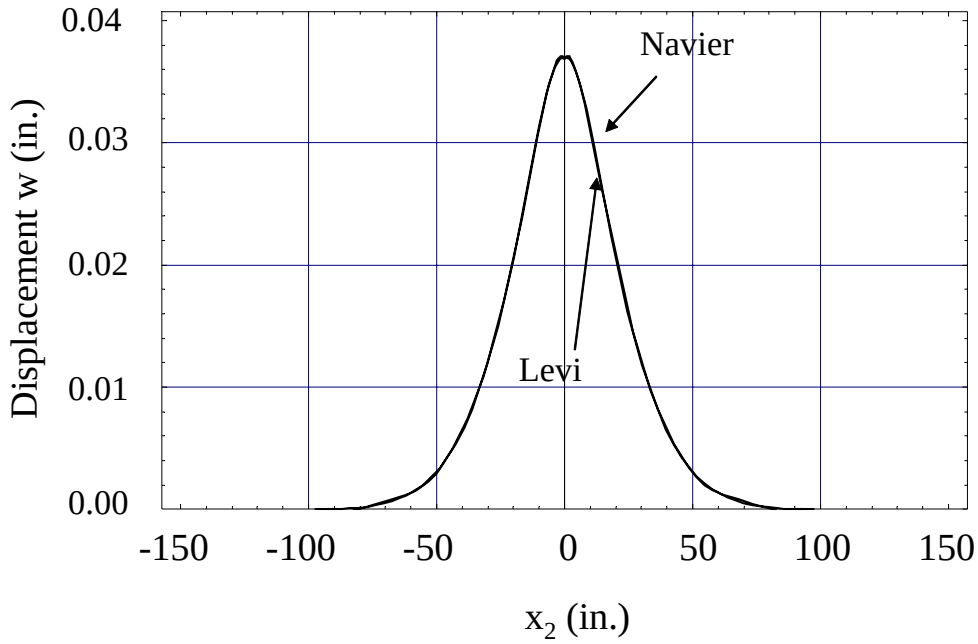

Figure 8-9 Displacement along section A-A at 26 kips

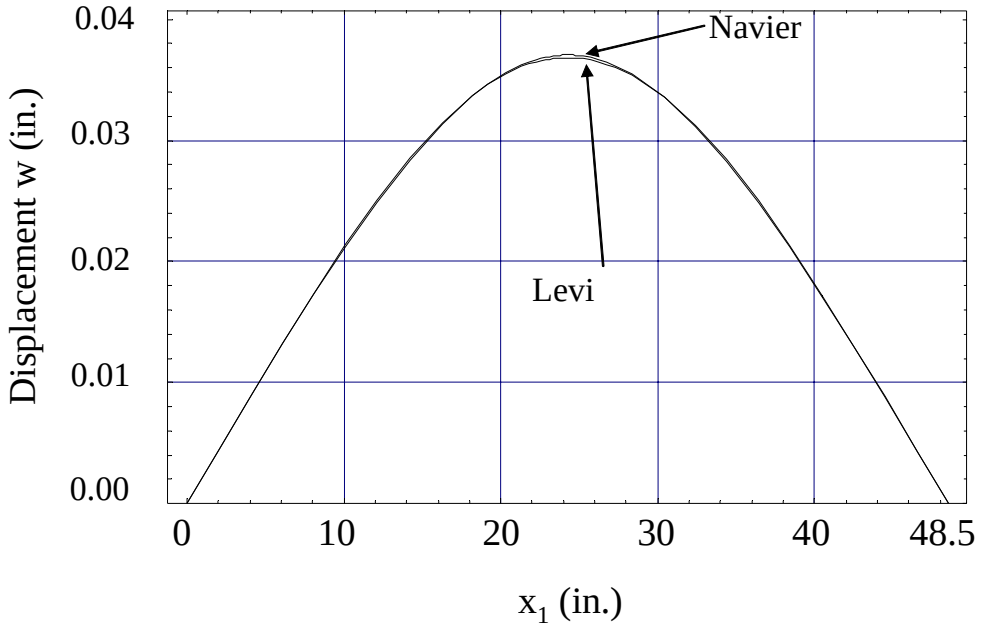

Figure 8-10 Displacement along section B-B at 26 kips

The three dimensional plot shown in Figure 8-11 obtained with the Navier's solution emphasizes the fact that the displacement for the orthotropic plate decreases to zero very rapidly with increasing distance from the center of the load. Figure 8-12 and Figure 8-13 show the displacements obtained with the Navier's solution along section A-A and section B-B (Figure 8-1) of a panel subjected to a load of 26 kips. The maximum displacements under a load of 26 kips are 0.0379 in. and 0.0303 in. for the orthotropic plate and the isotropic plate, respectively.

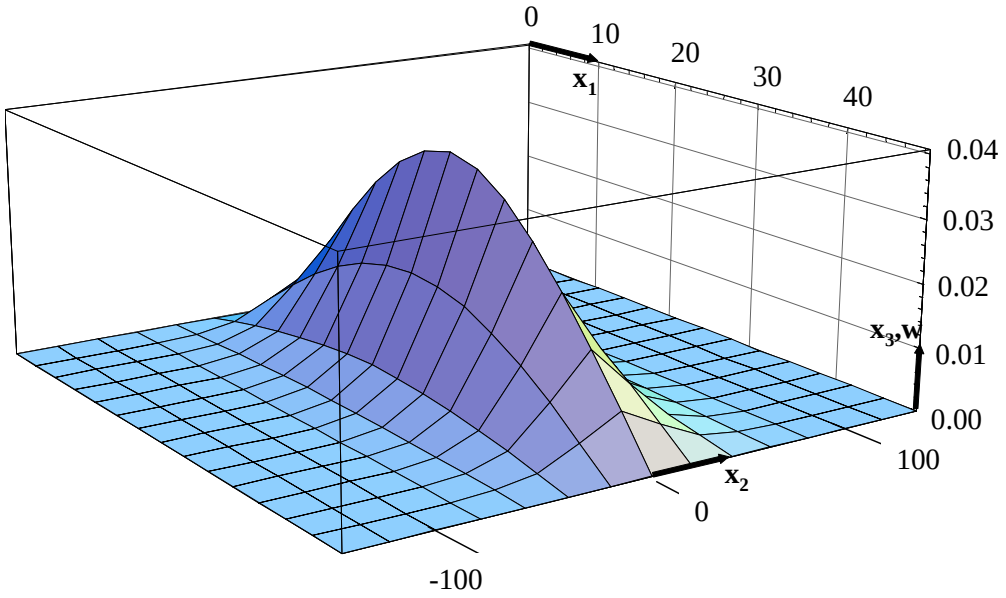

Figure 8-11 3D plot of the displacement at 26 kips

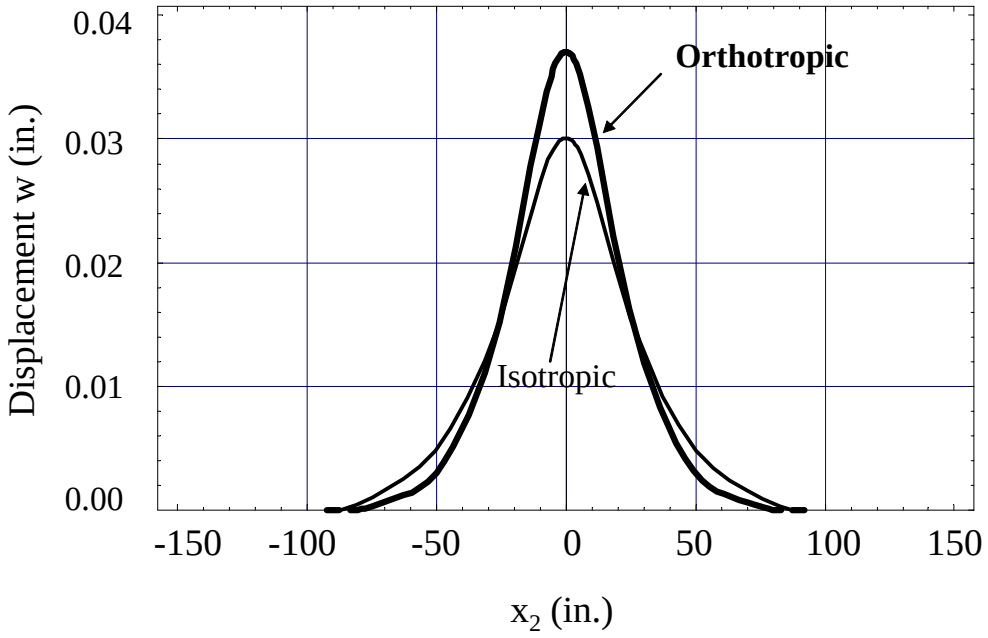

Figure 8-12 Displacement along section A-A at 26 kips

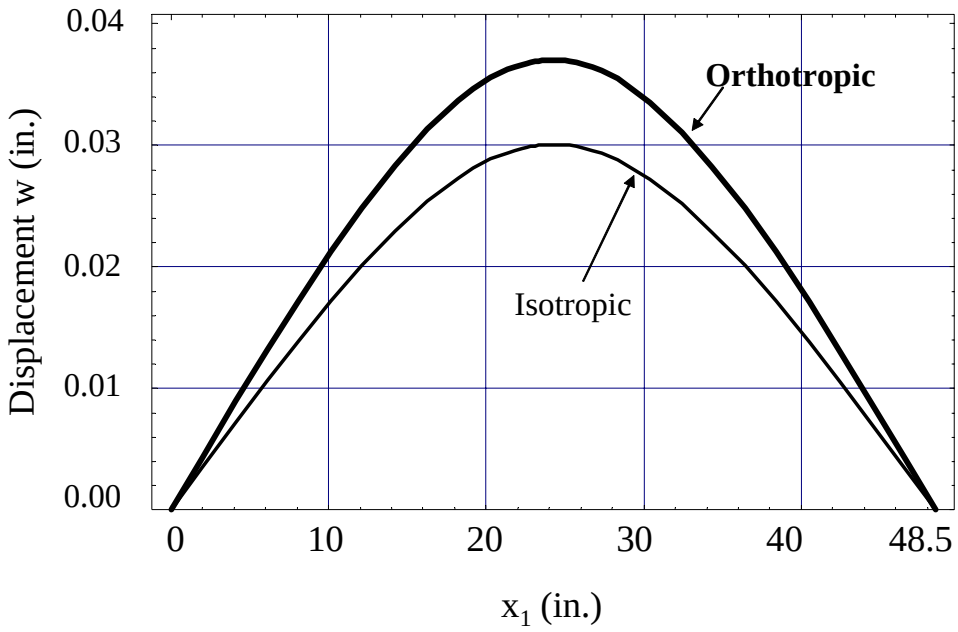

Figure 8-13 Displacement along section B-B at 26 kips

For calculating the bending moments, 50 terms are needed in the Fourier series. The panel bending moment, m_{x1}, along section A-A (Figure 8-1) is shown in Figure 8-14. The maximum moment per unit width is 7.35 kip-ft. for the orthotropic panel and 6.13 kip-ft. for the isotropic panel. Figure 8-15 indicates that the moment m_{x2} is smaller than m_{x1} and approaches zero faster than m_{x1} with increasing distance x_2 from the center of the load. Moreover, the moment m_{x2} is larger in the isotropic case than in the orthotropic case because the isotropic plate is stiffer in the x_2 direction.

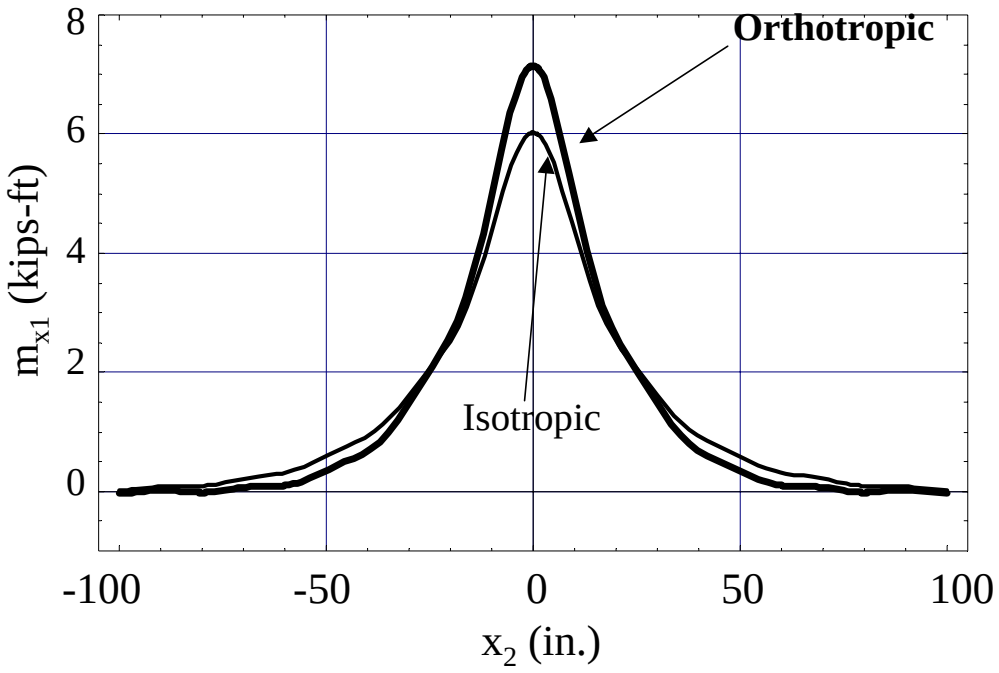

Figure 8-14 Moment m_{x1} along section A-A at 26 kips

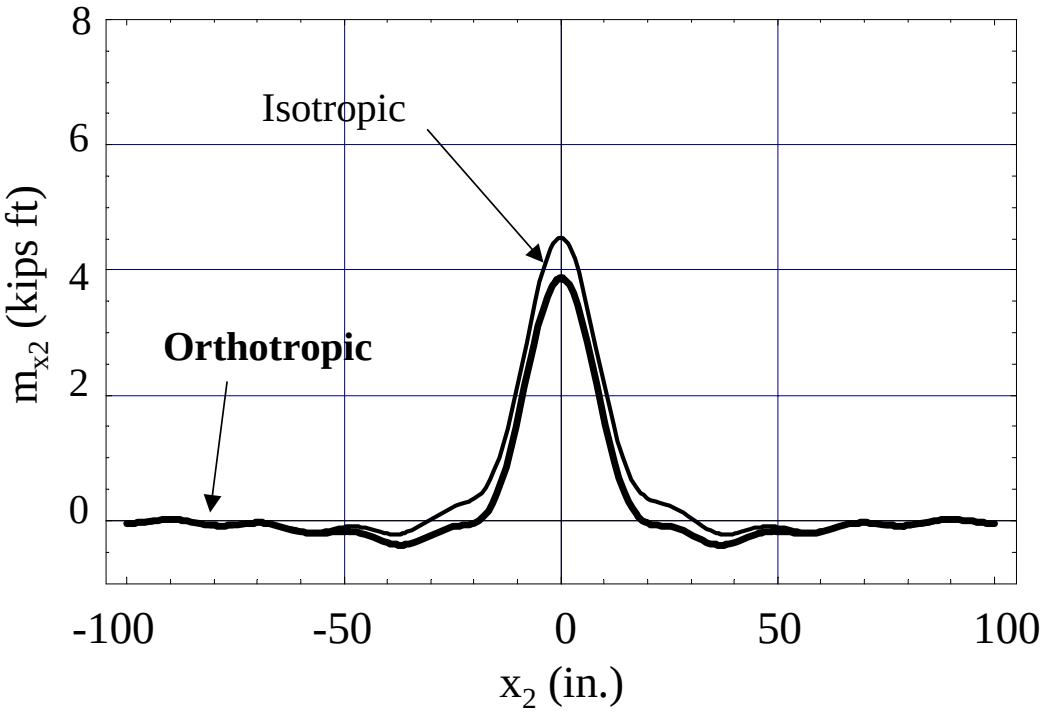

Figure 8-15 Moment m_{x2} along section A-A at 26 kips

The next section presents a parametric study performed using the Navier's method to determine the effective bending width for the GFRP sandwich panel considered here.

8.4 Effective Bending Width

8.4.1 Introduction

In this section, the Navier's solution is used for a parametric study to determine the effective bending width for several GFRP panels with different geometries.

The effective bending width used here is defined by Szilard (1974). According to this definition, the effective width *b'* for the bending of a plate is obtained by equating the actual moment area for m_{x1} with that of a fictitious rectangular moment diagram that has the same maximum moment as m_{x1} as shown in Figure 8-16.

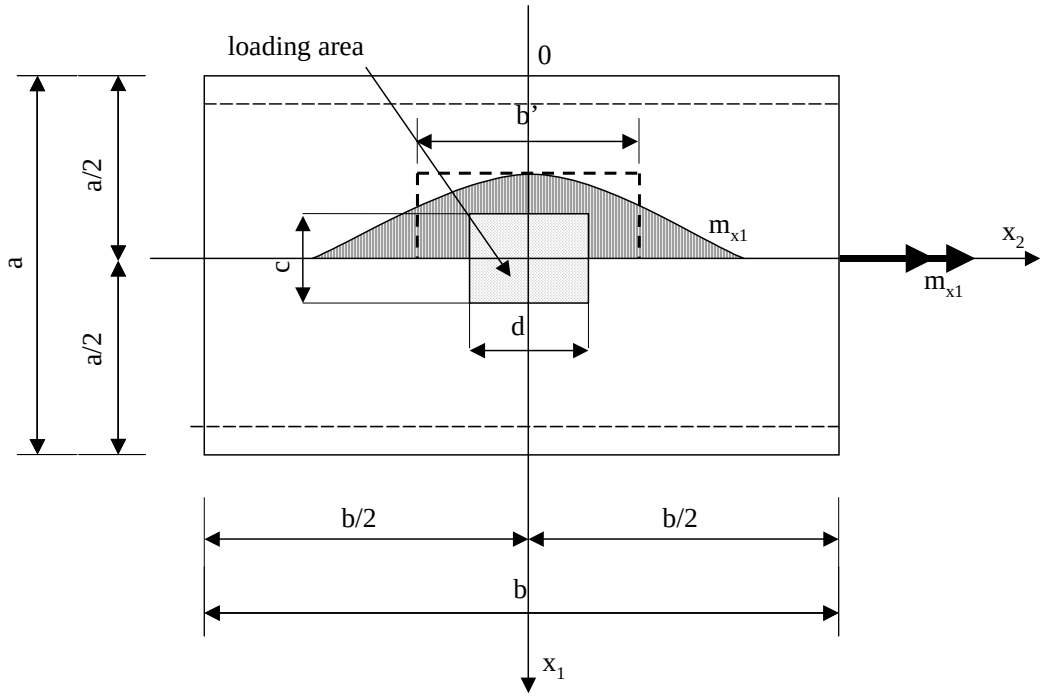

Figure 8-16 Effective bending width

Using the above definition, the effective bending width *b'* is given by the following formula:

$$b' = \frac{\int_{-b/2}^{b/2} m_{x1} dx_2}{m_{x1,\max}} \tag{8.53}$$

8.4.2 Test Panel

First the effective width of a honeycomb panel that has the same cross section as the test panel is considered. To this end, the moments calculated with the Navier's solution in Section 8.3.2 is used. With these moments, equation (8.53) yields *b'*=38.5 in. (3.21 ft.) for an orthotropic panel and *b'*=45.1 in. (3.76 ft.) for the isotropic panel. Hence, the condition of orthotropy reduces the effective bending width.

8.4.3 Parametric study

In this section, a parametric study is performed to calculate the effective bending widths using the Navier's solution for different panel and loading area dimensions, while the cross-sectional properties of the panel are fixed. With respect to the dimensions defined in Figure 8-16, *b* is assumed to be 10 times *a*. The results are given in Table 8-2. In the table, *(i)* stands for an isotropic panel and *(o)* for an orthotropic panel. It can be seen that the effective bending widths for the orthotropic panels are on the average 13.4% smaller than the effective bending widths for the isotropic panels.

Table 8-2 Effective bending width calculated with Navier's solution

d/a	*0.05*	*0.10*	*0.20*	*0.30*	*0.40*	*0.50*	*0.60*	*0.70*	*0.80*	*0.90*	*1.00*
b'/a *(o)*	0.65	0.69	0.76	0.84	0.91	0.99	1.05	1.12	1.18	1.24	1.30
b'/a *(i)*	0.75	0.79	0.89	0.98	1.07	1.15	1.22	1.29	1.36	1.42	1.48

If we ignore the different support conditions, the above results can be used to estimate the effective bending widths for the test panel which had a 12x12 in. loading area and for the actual bridge deck subjected to an HS25 truck. For the former, d/a = 0.25, and for the latter, d/a = 0.41.

9 FINITE ELEMENT ANALYSES OF TEST PANEL

9.1 Introduction

As mentioned in Section 8.1, the Kirchhoff-Love theory gives accurate results only if the ratio of the smallest lateral dimension of the plate to its thickness is at least ten. To obtain a more accurate assessment of the behavior of the test panel and to account for the actual boundary conditions used in the test, the panel is analyzed with the finite element method (FEM) in this chapter. The finite element analysis (FEA) considers the loading conditions of the initial static test, i.e., with the two spans of the panel loaded simultaneously. To exploit the symmetry condition of the two-span test panel, only one span is considered and the panel is assumed to be fixed along one edge, simply supported along the opposite edge, and free along the other two edges in the FEA.

9.2 Model Description

Finite element analyses are performed with a 3D mesh using Version 6-3.1 of the program ABAQUS. Two types of 3D models are developed for this purpose. The panel model has a span of 48.5 in. (center-to-center distance of the risers in the original test panel) and a width of 100 in.

The first model, Model A, uses 8-node quadratic thick-shell elements. The boundary conditions and mesh discretization are shown in Figure 9-1. Except for the shear moduli, the whole panel is modeled with the equivalent orthotropic material properties of a homogenized sandwich panel as presented in Table 8-1. The thick shell element implemented in ABAQUS accounts for the shear deformation. The shear moduli, G_{13} and G_{23}, are assumed to be the core shear moduli shown in Table 3-2. Model A is very simple and computationally very efficient. Consequentially, it is useful for parametric studies to determine the effective bending widths of a panel under different geometric and boundary conditions. Nevertheless, it is not capable of calculating the interface shear stresses between the face and the core of a panel. These stresses can cause debonding

failure, and are, therefore, important to evaluate.

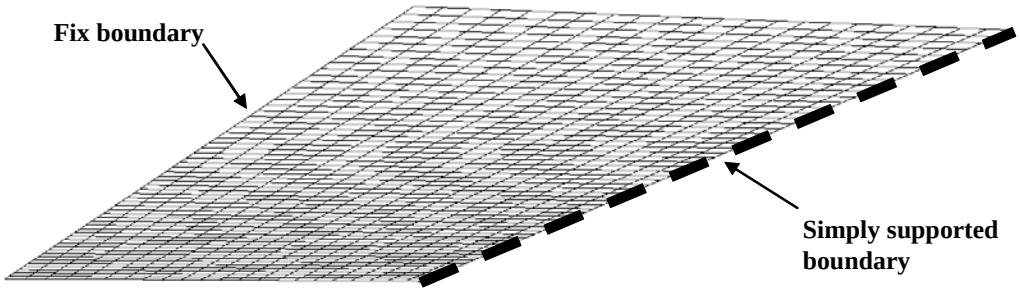

Figure 9-1 Boundary conditions and mesh discretization for Model A

For the above reason, a second model, Model B, is also considered. The boundary conditions and mesh discretization are shown in Figure 9-2. This model distinguishes the three distinct layers of a panel, i.e. the two faces and the core. The material properties for each layer are given in Table 3-2. The core is modeled using four layers of 20-node quadratic brick elements. The faces are modeled with 8-node quadratic shell elements. The shell elements are connected to the brick elements using the tie option of the program.

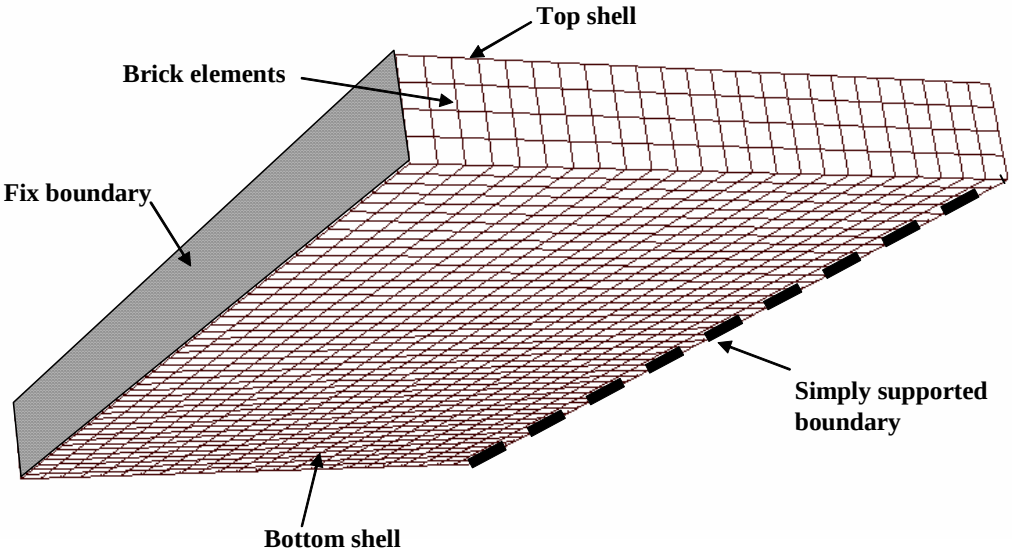

Figure 9-2 Boundary conditions and mesh discretization for Model B

For both models, the load exerted by each loading plate in the test is considered as a uniform traction.

9.3 Comparison of Numerical and Experimental Results

In this section, the data collected in the initial static test are compared to the results obtained with the FEA. All the values from the FEA are given at the nodal points. The displacement along section A-A (see Figure 8-1) under a 20-kip load is shown in Figure 9-3. It can be seen that Model A is slightly softer than Model B, because in Model A, the cross-sectional area of the faces is neglected for shear, whereas in Model B, the shear moduli of the faces, G_{f13} and G_{f23}, are assumed to be 237 ksi.

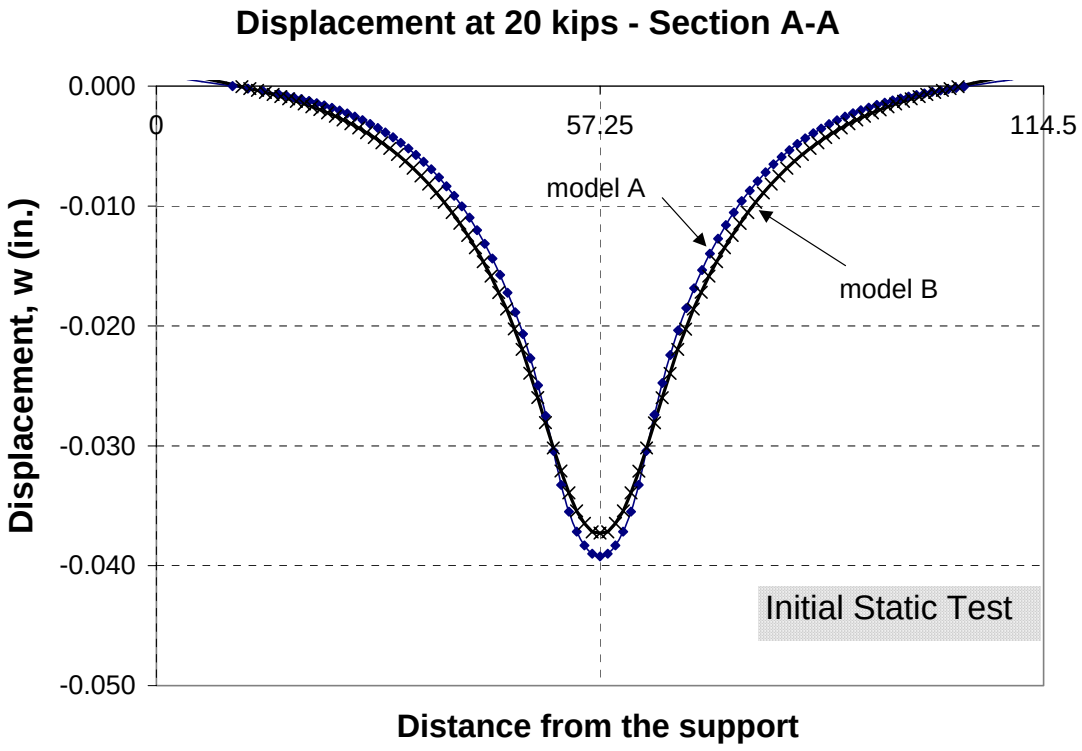

Figure 9-3 Displacement along section A-A (Figure 8-1) at 20 kips

As shown in Figure 9-4, the load-displacement curve obtained with Model B agrees well with the experimental result. The displacements from the experiment are the adjusted displacements that do not include the panel settlements at the supports. A 3D

representation of the displacement, *w*, of Model B is shown in Figure 9-5. The localized bending phenomenon is well shown and closely simulates the local bending exhibited by the test panel. This is due to the soft core. Figure 9-3 shows that Model A has a slightly more pronounced localized bending behavior than Model B.

The load-strain curves from the strain gages glued on Span 1 of the test panel are compared to the numerical results in Figure 9-6 through Figure 9-10. The gage numbers are identified in Figure 7-6. It can be seen that the numerical and experimental results show a good correlation. The strains in the x_2 direction obtained with the two finite element models appear to be smaller than those from the experiment as shown in Figure 9-11. This is probably due to a localized effect introduced by the loading plate that cannot be exactly captured with the FE models.

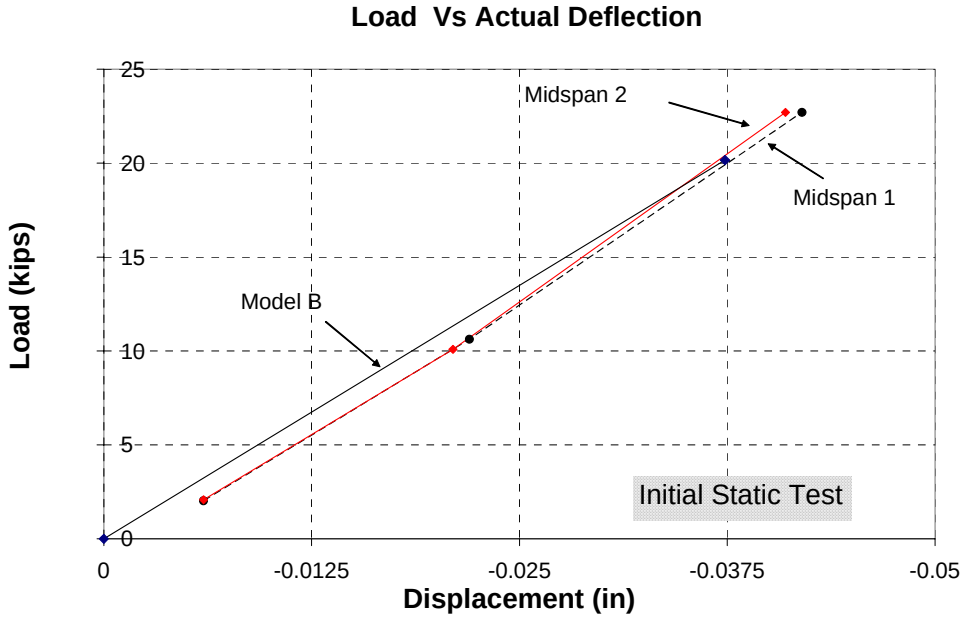

Figure 9-4 Comparison of numerical result to experimental load-deflection curves

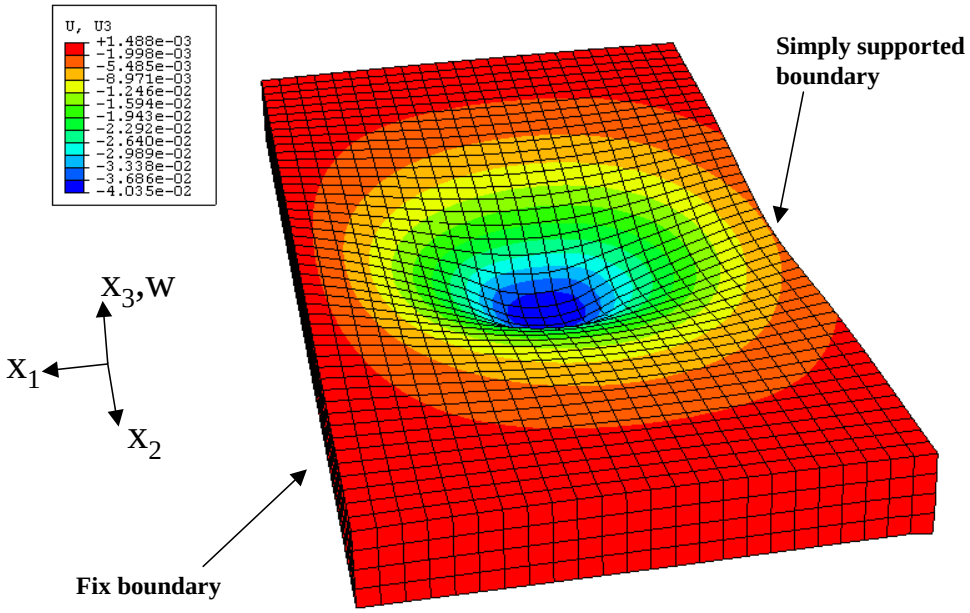

Figure 9-5 3D plot of the displacement at 20 kips (Model B)

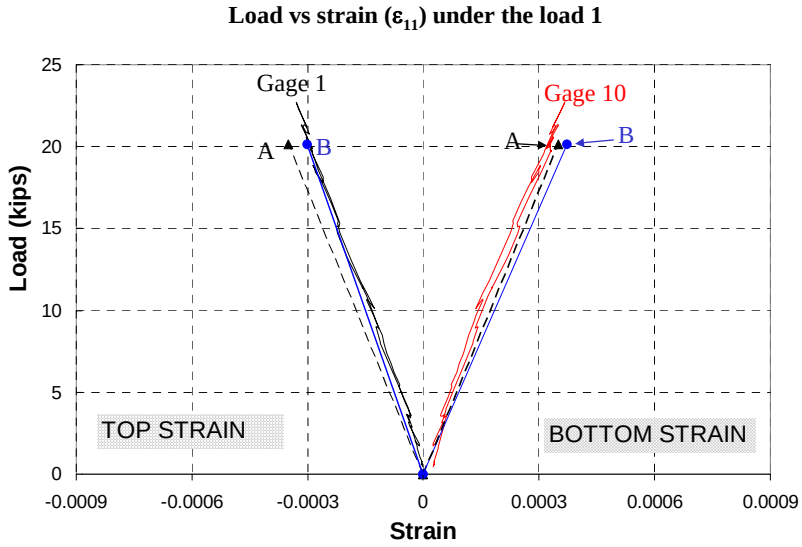

Figure 9-6 Load-strain (ε_{11}) curves of the gages under load 1

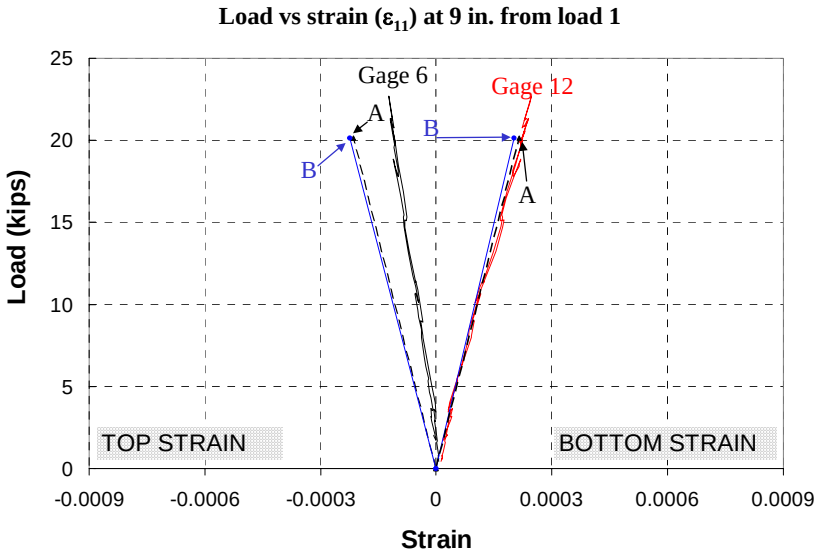

Figure 9-7 Load-strain (ε_{11}) curves at 9 in. from load 1

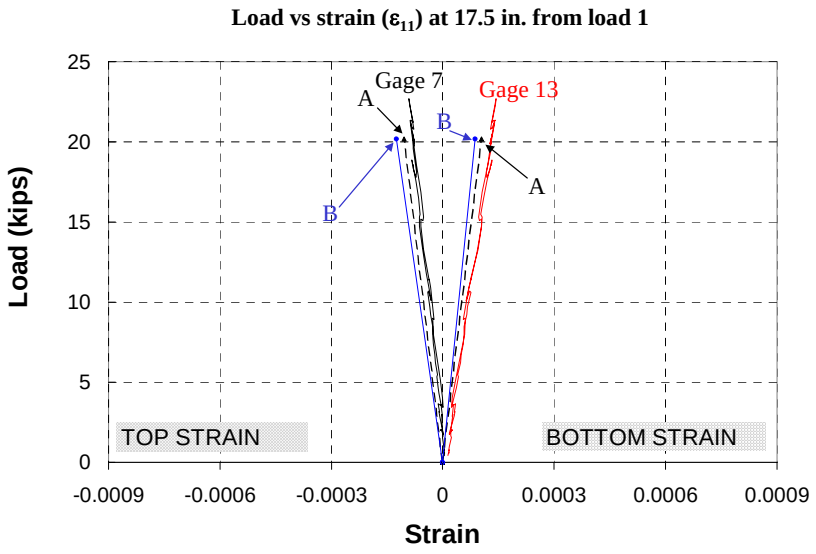

Figure 9-8 Load-strain (ε_{11}) curves at 17.5 in. from load 1

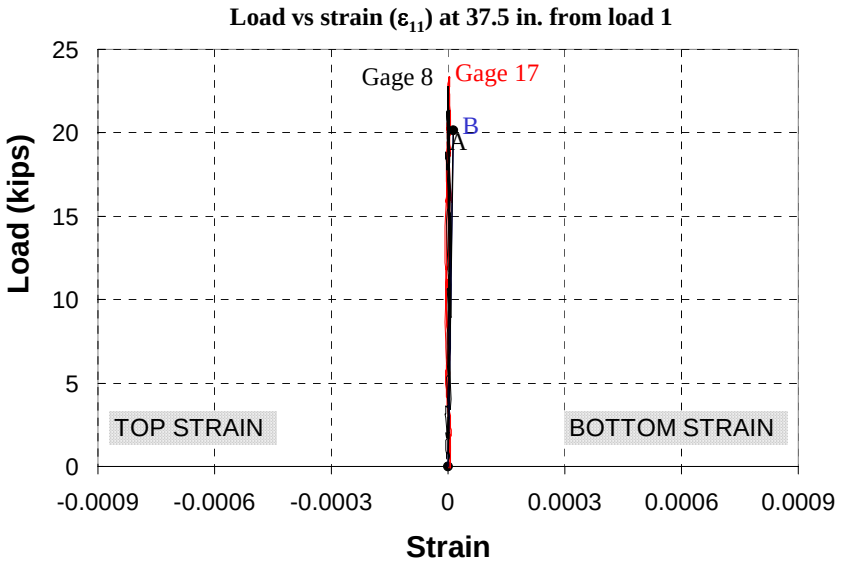

Figure 9-9 Load-strain (ε_{11}) curves at 37.5 in. from load 1

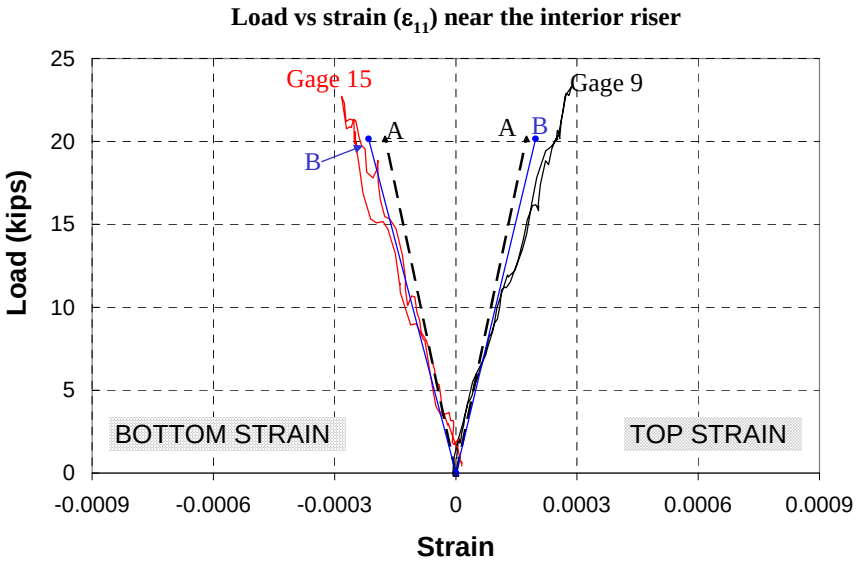

Figure 9-10 Load-strain curves (ε_{11}) near the interior riser of Span 1

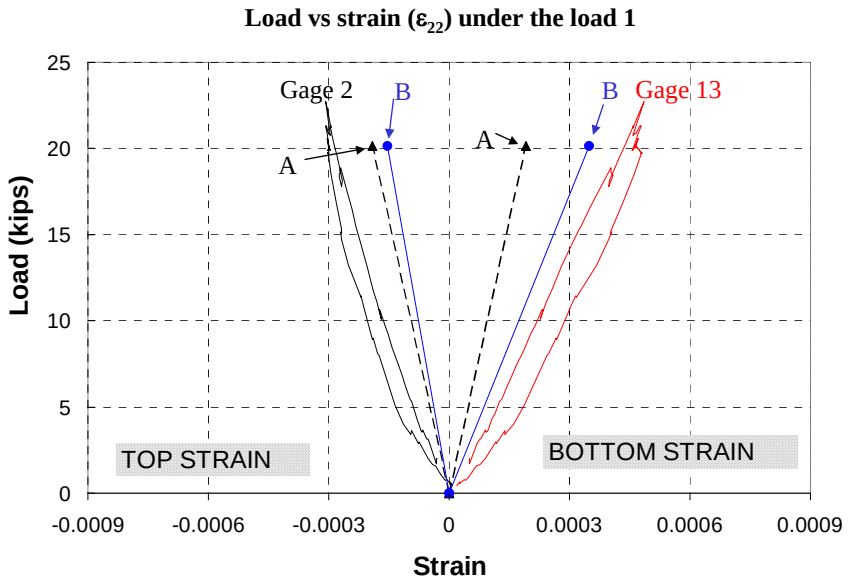

Figure 9-11 Load-strain (ε_{22}) curves of the gages under load 1

Figure 9-12 and Figure 9-13 show the shear stresses obtained from Model B at the top face-core interface under a load of 20 kips. It can be seen that the shear stress is highly concentrated near the loading plate.

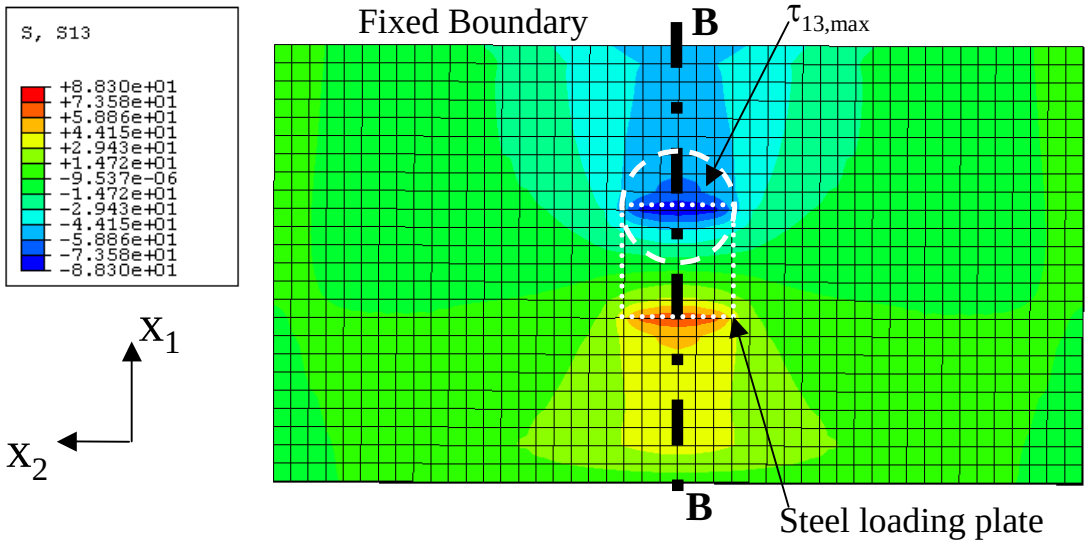

Figure 9-12 Shear stress τ_{13} at the top of the core

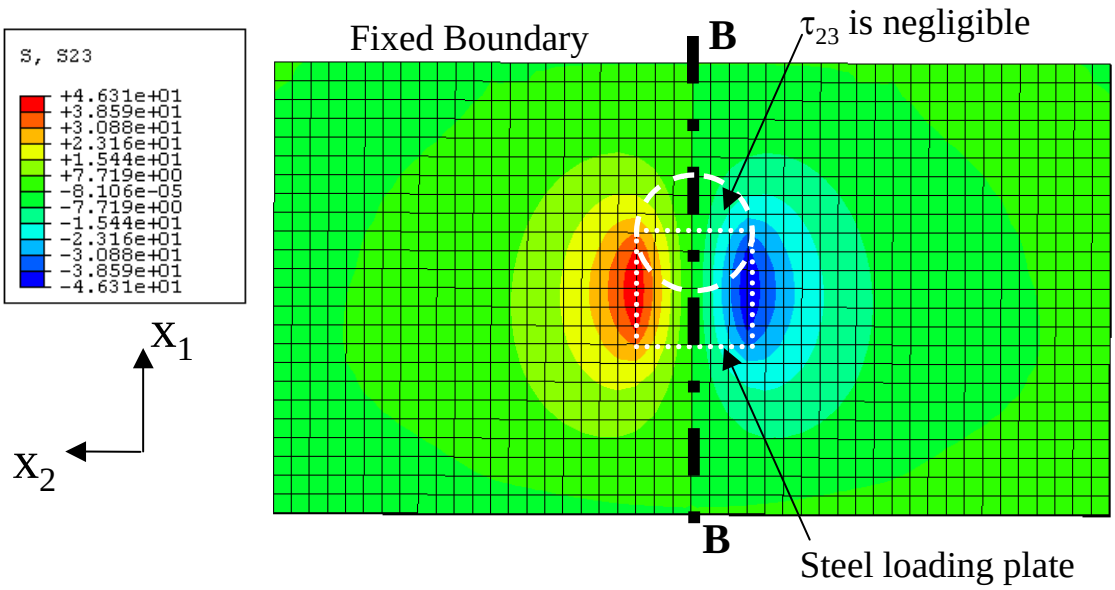

Figure 9-13 Shear stress τ_{23} at the top of the core

Similar to the FE analyses of the beams as presented in Chapter 6, the shear stress, τ_{13}, shows a peak at the edge of the steel loading plate as shown in Figure 9-14. As explained before, this peak is caused by the localized bending of the panel. Outside the loading plate, the shear stress is nearly constant. The maximum shear stress, τ_{13}, is 88.3 psi and the average shear stress in the constant stress zone is 53 psi. It is noted that the shear stress is not symmetric in the graph because of the asymmetric support conditions.

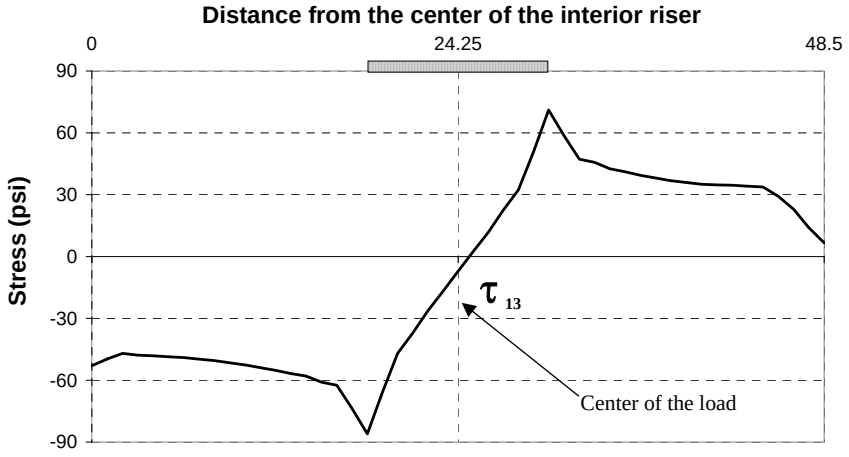

Figure 9-14 Shear stress τ_{13} at 20 kips along section B-B

9.3.1 Distribution of Interface Shear

The shear stress at the interface between a face and the core triggers the delamination failure and, consequentially, its distribution is important to examine. Model B can be used to calculate the interface shear stress between the core and a face. The boundary conditions and dimensions of the panel considered here are the same as those of the test panel. Figure 9-15 shows the shear stress τ_{13} from the FEA at the top face-core interface under a load of 20 kips. The figure indicates that the shear stress decreases very quickly away from the load. At about 25 in. from the center of the load, the shear stress τ_{13} is 11% of $\tau_{13,max}$, and it goes to zero at about 43 in. from the center of the load.

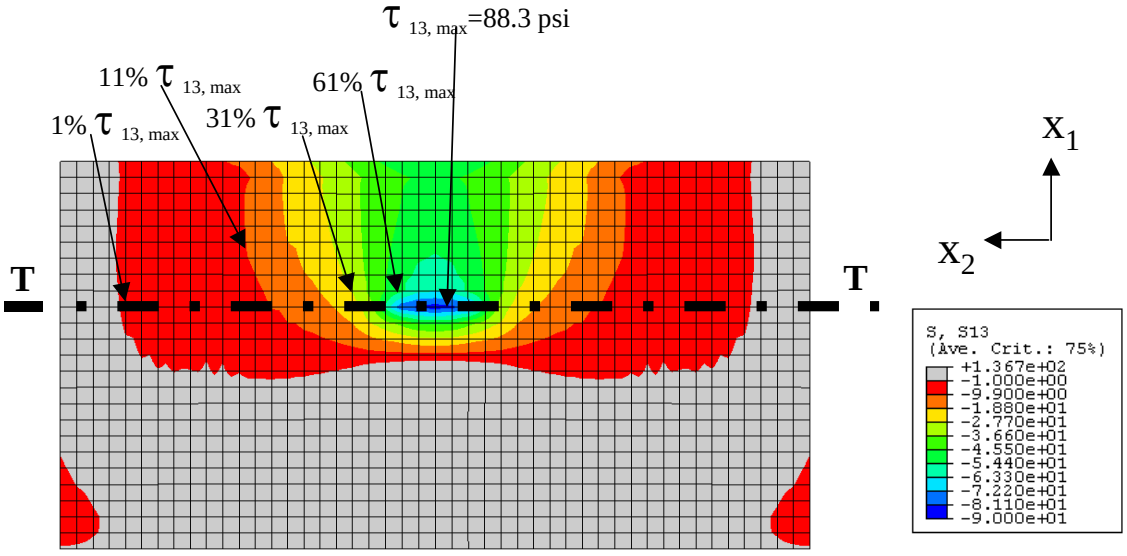

Figure 9-15 Shear stress τ_{13} at the top of the core

9.4 Comparison of the Shear Strengths of the Test Beams and Test Panel

Similar to the beam tests reported in Chapter 5, the panel test shows that the governing failure mode of the panel is the delamination of the face from the core. The interface shear strengths of the beams estimated from the test results using different methods are shown in Table 6-1. As shown in Table 6.1, the average interface shear

stresses at failure in the constant shear zone estimated with the FEA were 380 psi for Test 1, 310 psi for Test 2, 190 psi for Test 3, and 550 psi for Test 4. Thus, the average shear strength of all four beams was 357 psi. At a load of 20 kips, the average interface shear stress in the constant shear zone of the panel obtained from the FEA is 53 psi, which is 15% of the average shear stress of the beams at failure.

In phase 1 of the fatigue test (from 0 to 15,000 cycles), the panel was loaded to a maximum load of 40 kips. At 40 kips, the interface shear stress in the shear span is estimated to be 106 psi according to the above FEA, which is 30% of the average shear strength of the beams. This is a very low value and it is not expected to induce debonding under the limited number of fatigue load cycles. Therefore, the premature delamination of the test panel in Span 2 during the initial fatigue load cycles was most likely caused by defects introduced in the fabrication process. This is confirmed by the fact that no delamination occurred in Span 1 during these cycles.

After 1.5 million load cycles, Span 1 delaminated at a static load of 62 kips as shown in Figure 7-28. Under a load of 62 kips, the interface shear stress in the constant shear zone of Span 1 is estimated to be 164 psi according to the FEA.

It is well known that GFRP has a lower fatigue resistance than Carbon and Aramid FRP. ACI 440 (2000) suggests that stresses in GFRP materials be limited to 20% of the ultimate strength under service load conditions. Nevertheless, no information is available with regard to the fatigue endurance of the face-core interface.

9.5 Effective Bending Width

9.5.1 Introduction

The analytical results from the plate theory show that the effective bending width of an orthotropic panel is 13.4% smaller than that of an isotropic panel. However, the analytical solution only considers simple boundary conditions and does not consider the shear deformation of the soft core. This section presents a study performed with finite

element analysis to determine how the panel boundary conditions and the shear deformation affect the effective bending width. The numerical result is used to determine the effective bending width and compare with that obtained from the test data and that used in the preliminary design evaluation in Chapter 4.

Model A is used here because it is very simple and computationally efficient, and, consequentially, more suitable for parametric studies. The material properties of the panel are given in Table 8-1. The shear deformation of the panel is taken into account by using the shear moduli of the core given in Table 3-2.

9.5.2 Test Panel

Figure 9-16 shows the moment m_{x1} at nodal points along section A-A (as identified in Figure 8-1) for a panel subjected to a load of 20 kips.

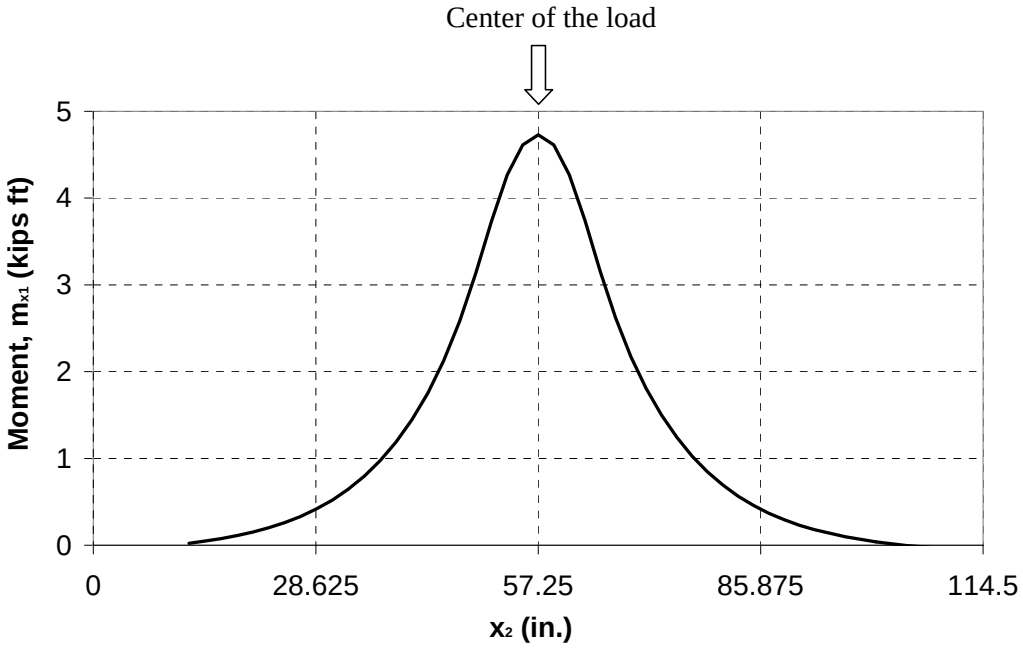

Figure 9-16 Moment m_{x1} along section A-A

The maximum moment per unit width, m_{x1}, calculated with the finite element model is 4.73 kips-ft. Using calculated moments along section A-A, equation (8.53) gives an effective bending width, *b'*, of 27.9 in. (2.33 ft.). In order to compare the

theoretical effective bending width with the experimental value, the plane section remaining plane assumption is used to calculate the bending moment from the experimental strain measurements. Accordingly, the substitution of equation (8.7) into (8.9) leads to

$$m_{x1} = \int_{-H/2}^{H/2} \frac{E_{11}}{1-\upsilon_{12}\upsilon_{21}} (\varepsilon_{11} + \upsilon_{21}\varepsilon_{22}) x_3 dx_3 \tag{9.1}$$

$$\upsilon_{21} = \upsilon_{12} \frac{E_{11}}{E_{22}} \tag{9.2}$$

At a load of 20 kips, the maximum strains ε_{11} and ε_{22} at the bottom of Span 1 of the test panel were 0.000302 and 0.000439, respectively. By assuming a linear strain distribution along the depth of the panel and using the material properties in Table 8-1, it is possible to integrate equation (9.1) and evaluate the maximum moment:

$$m_{x1,\max} = \frac{1273000}{1-0.301\times 0.189} \int_{-3.75}^{3.75} \left(\frac{0.000302}{3.75} x_3 + 0.189 \frac{0.000439}{3.75} x_3\right) x_3 dx_3 \tag{9.3}$$

Therefore, the experimental maximum moment per unit width, m_{x1}, is 4.87 kips-ft., which is only 3% higher than the numerical result.

Equation (9.1) shows that the strains in both directions contribute to the moment m_{x1}, and, therefore, affect the effective bending width. Substituting equation (9.1) into equation (8.53), we have:

$$b'_{\varepsilon} = \frac{\int_{-b/2}^{b/2} \int_{-H/2}^{H/2} (\varepsilon_{11}(x_2, x_3) + \upsilon_{21}\varepsilon_{22}(x_2, x_3)) x_3 dx_3 dx_2}{\max_{along\ x_2} \left(\int_{-H/2}^{H/2} (\varepsilon_{11}(x_2, x_3) + \upsilon_{21}\varepsilon_{22}(x_2, x_3)) x_3 dx_3 \right)} \tag{9.4}$$

Equation (9.4) expresses the effective bending width as a function of the strains and Poisson's ratio. The contribution of the strain in direction x_2 is very small for two reasons. First, in equation (9.1), ε_{22} is multiplied by the Poisson's Ratio υ_{21} and, therefore, its effect is decreased by 81%. Secondly, the FE analysis shows that the distribution of ε_{22} is different from that of ε_{11}. ε_{22} approaches zero extremely quickly and

becomes negative at about 12 in. from the center of the load as shown in Figure 9-17. Therefore, the contribution of ε_{22} is neglected here.

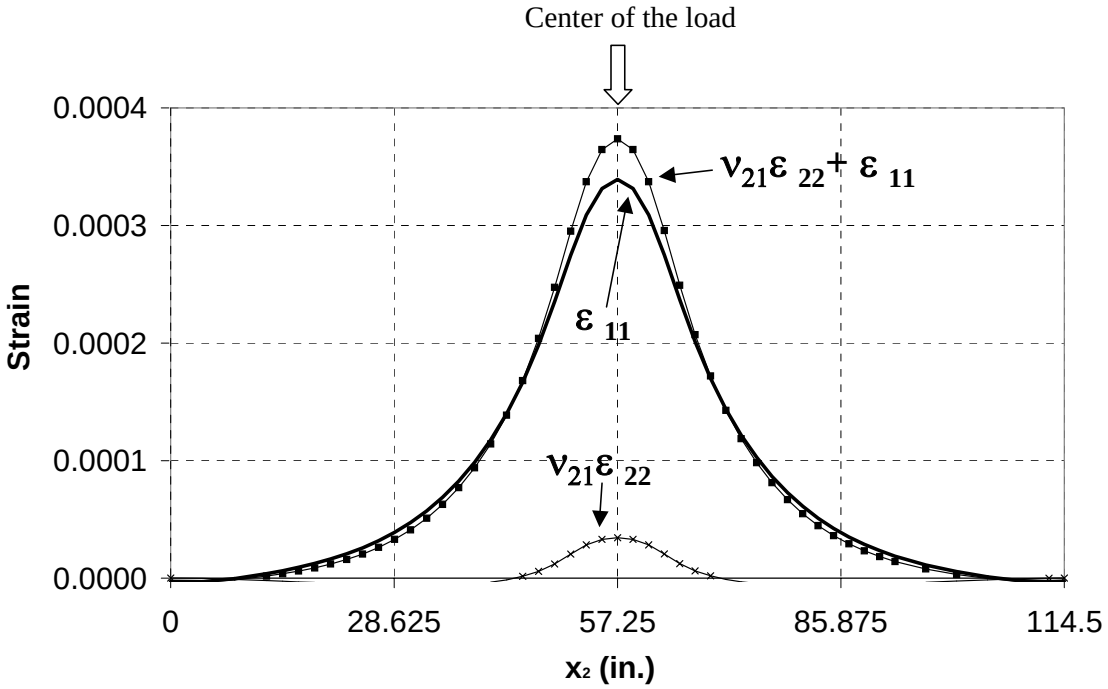

Figure 9-17 Strains ε_{11} and ε_{22} along section A-A (Figure 8-1)

Assuming a linear variation of $\varepsilon_{11}(x_2,x_3)$ along the depth of the panel, the function that defines the variation of $\varepsilon_{11}(x_2,x_3)$ along the depth of the panel is given as:

$$\varepsilon_{11}(x_2,x_3)=\frac{\varepsilon_{11}^{top}(x_2)-\varepsilon_{11}^{bot}(x_2)}{H}x_3 \quad \text{for} \quad -\frac{H}{2}<x_3<\frac{H}{2} \tag{9.5}$$

where $\varepsilon_{11}^{top}(x_2)$ is the strain at the top of the panel and $\varepsilon_{11}^{bot}(x_2)$ is the strain at the bottom of the panel. In equation (9.5), the compressive strain is considered as negative. Substituting equation (9.5) into (9.4) and integrating with respect to x_3 from -H/2 to H/2, we obtain the following expression for the effective bending width, which is based on the strain values at the top and bottom of a panel:

$$b'_{\varepsilon}=\frac{\int_{-b/2}^{b/2}\left[\varepsilon_{11}^{top}(x_2)-\varepsilon_{11}^{bot}(x_2)\right]dx_2}{\max_{along\ x_2}\left[\varepsilon_{11}^{top}(x_2)-\varepsilon_{11}^{bot}(x_2)\right]} \tag{9.6}$$

Using ε_{11} obtained with the FEA in the above equation, we have b'_{ε} equal to 29.4 in.

(2.45 ft.), which is 8% higher than the width *b'* evaluated directly from the bending moments.

The strain variations at the top and bottom of the panel along section A-A (as identified in Figure 8-1) of Span 1 are shown in Figure 9-18 and Figure 9-19. With the experimental strain values, equation (9.6) leads to an effective bending width, b'_{ε}, of 28.6 in. (2.38 ft.).

Table 9-1 summarizes the numerical and experimental results on the effective bending width. The numerical results agree very well with the experimental results. In Table 9-1, *b'* is the effective bending width calculated with the m_{x1} obtained from the FEA and b'_{ε} is the effective bending width calculated with ε_{11}.

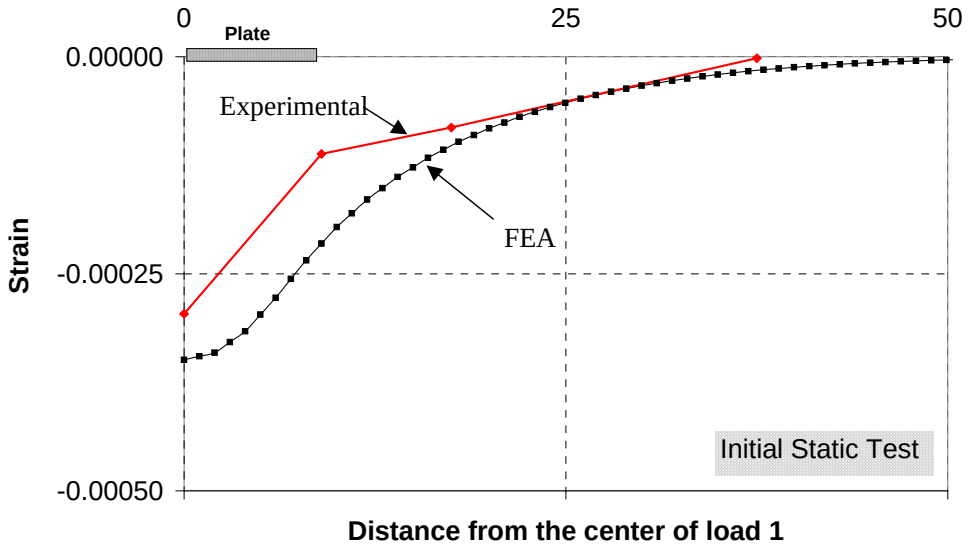

Figure 9-18 Strains ε_{11} on the top of the panel along section A-A of Span 1

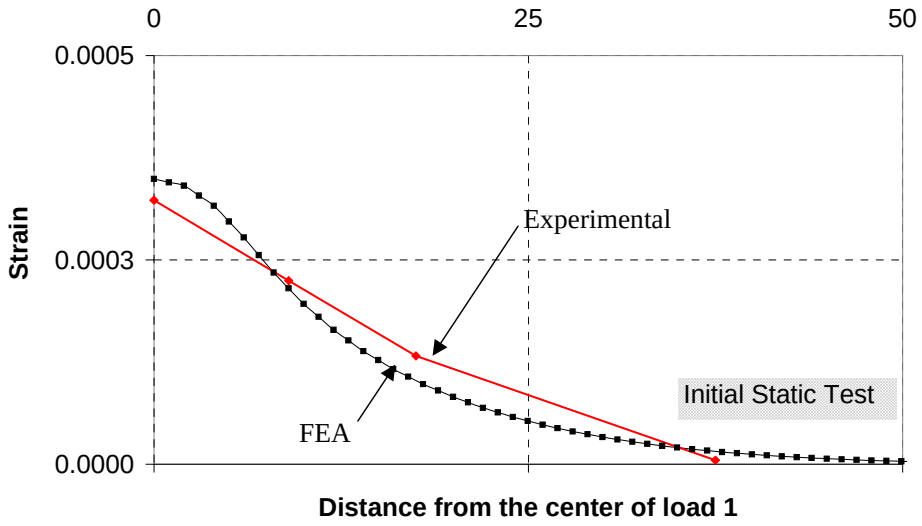

Figure 9-19 Strains ε_{11} on the bottom of the panel along section A-A (Figure 8-1) of Span 1

Table 9-1 FE and experimental effective bending widths

	b' (ft.)	*b'$_\varepsilon$ (ft.)*
FEA	2.33	2.45
Experimental		2.38

9.5.3 Parametric Study

This section examines the influence of the panel boundary conditions and the shear deformation in the soft core on the effective bending width. Instead of using the dimensions of the loading plates used in the panel test, the actual foot print of a HS25 truck is considered in the analyses. Hence, results of this study can be used as a guidance for actual design. In the AASHTO LFRD Specifications (1998), the foot print of a wheel load is assumed to be a rectangle with a width of 20 in. and length l given by:

$$l = 2.28\gamma\left(1+\frac{IM}{100}\right)P \tag{9.7}$$

where γ is the load factor, IM is the dynamic-load allowance, and P is the wheel load. For the type of truck load and deck considered here, γ is 1.75, IM =30, and P=20 kips. Therefore, the contact area for the wheel load is 20x19 in. Hence, with respect to Figure

8-16, c=20 in. and d=19 in. Furthermore, considering the dimensions of the actual deck, a is assumed to be 48.5 in. and b is assumed to be 525 in.

Effect of the Shear Deformation

To examine the effect of the shear deformation due to the soft core, we consider a panel with two opposite edges simply supported and the other two edges free. First, the panel is analyzed as a thin plate with Model A. The maximum moment per unit width, m_{x1}, under a load of 20 kips is 4.18 kip-ft. and effective bending width calculated is 3.72 ft. Second, the panel is analyzed as a thick plate. The maximum moment per unit width, m_{x1}, under a load of 20 kips is 4.81 kip-ft. and the effective bending width calculated is 3.25 ft. The above results show that the effective bending width based on the thick plate theory is 87% of that based on a thin plate.

To check the results obtained with the Kirchhoff-Love theory in Chapter 8, the results obtained with the finite element model based on the thin plate assumption are considered. The maximum moment per unit width, m_{x1}, under a load of 20 kips is 4.18 kip-ft. according to the finite element model and 4.16 kips-ft. according to the Navier's solution. The effective bending width calculated with the finite element model is 3.72 ft. and with the Navier's method is 3.86 ft. The results show good agreement.

Effect of Boundary Conditions

To examine the influence of the panel boundary conditions, a panel with one edge fixed, the opposite edge simply supported and the other two edges free is analyzed with Model A using the thick plate assumption. The maximum moment per unit width, m_{x1}, under a load of 20 kips is 3.67 kip-ft. and the calculated effective bending width is 2.86 ft. Hence, compared to the previous results of a simply supported panel, fixing one edge reduces the effective bending width by 11%.

Furthermore, a panel with two opposite edges fixed and the other two free is loaded

with a load of 20 kips. The maximum moment per unit width, m_{x1}, is 2.24 kip-ft. and the effective bending width is 2.69 ft. In this case, the effective bending width is 17% smaller than that of a simply supported panel.

9.5.4 Evaluation of Design Assumptions on Effective Widths

Effective Bending Width

The effective bending width assumed in the design evaluation in Chapter 4 is 4 ft., while that obtained from the finite element analysis is 2.86 ft. (Section 9.5.3). However, the design is still conservative because the evaluation was based on a point load at midspan, whereas, in reality, the panel is loaded with a truck wheel of finite dimensions. Furthermore, the design evaluation was based on simply supported boundary conditions, whereas the FEA considers one side fixed and the other simply supported.

For a simply supported panel subjected to the design wheel load of 26 kips, assuming a point load and an effective bending width, *b'*, of 4 ft. leads to a design moment of 6.6 kip-ft. Based on the finite element analysis, for a panel fixed on one side and simply supported on the other three, the maximum bending moment per unit width is 4.8 kip-ft. Therefore, the design of the panel is conservative.

Effective Width for Shear

The effective shear width, w_s, was assumed to be 7 ft. in the design evaluation in Chapter 4. The shear stress at the interface between the face and the core for a 7-ft.-wide strip can be calculated with equation (4.20) by assuming $b=w_s$. For a beam subjected to a load of 26 kips, equation (4.20) gives an interface shear τ_{13}^{int} of 22 psi. The shear stress has been calculated with finite element analysis using Model B for a load of 26 kips and a loading area equal to the foot print of an HS25 truck. In the constant shear zone, the interface shear stress obtained is 49 ksi, which is 2.2 times the shear stress assumed in the design evaluation. Hence, the effective shear width should be 3.1 ft., with which

equation (4.20) will lead to an interface shear τ_{13}^{int} of 49 psi.

In spite of the above observation, the shear strength assumed initially is very conservative. The shear strengthening detail introduced by Kansas Structural Composites, Inc. (KSCI) has increased the interface shear strength significantly. The shear strength of the weakest beam tested was 160 psi as shown in Table 6-2, while the shear strength assumed in the design evaluation is 80 psi. Using a shear strength of 160 psi and an effective width of 3.1 ft., equation (4.21) leads to an Ultimate Shear Load Capacity, P_s, of 133 kips. This satisfies the design requirement in that 45% of P_s is higher than the maximum factored load of 56.5 kips. Considering a service wheel load of 26 kips, the factor of safety against delamination failure is about 5.

Furthermore, the panel test results indicate that the panel continued to carry additional load after delamination had first occurred. This is because of the redistribution of the shear stress in the panel.

Design Considerations

The finite element analyses indicate that the deflection and bending stress requirements can be easily met by the GFRP panel. However, past research as well as results of this study shows that the load carrying capacity of GFRP sandwich panels is governed by the interface shear strength between the core and the faces. Even if the bending stress is low compared to the tensile strength of the material, the panel might be unsafe because the level of the interface shear stress could be too high compared to the interface shear strength.

Currently, the design of this type of panels does not explicitly account for the interface shear strength and, in particular, the fatigue endurance of the interface bond. Hence, improved design provisions that account for the interface shear should be developed. Nevertheless, little information is available with respect to the fatigue endurance at the face-core interface. In view of this, it is suggested that the interface

shear stress be limited to 20% of the interface shear strength under service loads, as suggested by ACI 440 (2000) to prevent the creep rupture or fatigue failure of GFRP bars in general. Furthermore, to ensure a consistent shear strength, good quality control should be exercised in the manufacturing process.

10 SUMMARY AND CONCLUSIONS

10.1 Summary

In this report, the design and load-carrying capacity of the glass fiber reinforced polymer (GFRP) deck on the O'Fallon Park bridge have been evaluated. The deck panels were manufactured and installed by Kansas Structural Composites, Inc. (KSCI). The studies conducted here include the laboratory evaluation of the strengths and stiffness of four GFRP beams, the crushing capacities of panel specimens, and the strength, stiffness, and fatigue endurance of a full-size two-span continuous deck specimen. Furthermore, the test results obtained are used to validate analytical and finite element models, which have been developed to yield general design recommendations.

The deck design was based on the 16th Edition of the AASHTO Specifications (1996), the AASHTO LFRD Specifications (1998), past research data, and the special provisions stipulated in the contractual document of the City and County of Denver (2002).

Four beams were tested to evaluate the influence of the face thickness on the load resisting behavior of a beam. The beams had a sandwich construction with top and bottom faces and a 6.5-in.-high honeycomb core. Three of them were 13-in. wide and one 12-in. wide. The latter was due to manufacturing irregularity. Two had a face thickness of 0.375 in. and two had 0.500-in. faces. The beams were loaded to failure under a 3-point bending configuration to evaluate the stiffness and load-carrying capacity.

Four approximately 13x12-in. panel specimens were subjected to compressive loads to find the ultimate crushing capacity. Manufactured together with the beam specimens, two crushing-test specimens had a face thickness of 0.375 in. and two had 0.500-in. faces.

Analyses were conducted using the Timoshento beam theory and finite element

models to study the flexural behavior and failure mode of the beams. An interface finite element model based on nonlinear fracture mechanics was employed to study the delamination between the faces and the core of a beam at the ultimate load. Based on the test and analysis results, a panel section was selected by KSCI for the O'Fallon Park bridge deck.

A full-size, two-span continuous deck panel that was 114.5-in. long, 120-in.wide, and 7.5-in. thick with 0.375-in. faces was tested under static loads and fatigue load cycles. The deck specimen had the same design as the O'Fallon Park bridge deck. The panel was supported on three reinforced concrete risers and anchored to the supports using mechanical anchor bolts. The aim of the test was to study the load-carrying capacity and fatigue endurance of the GFRP panel and mechanical anchors. Prior to the fatigue test, a static test was performed to evaluate the load-resisting behavior of an undamaged panel. In the fatigue test, the panel was subjected to 1.5 million load cycles till delamination occurred in both spans. Once the fatigue test was completed, the panel was loaded each span at a time to failure.

The deck panel has been analyzed using the Kirchhoff-Love plate theory and finite element models, which have validated with the test results. These analyses are to investigate the load distribution and determine the effective bending widths of a panel subjected to the wheel load of an HS 25 truck. The influence of the material orthotropy, shear deformation, and boundary conditions on the effective width has also been investigated.

Based on the results of the aforementioned tests and analyses, design recommendations are provided.

10.2 Conclusions

The following major conclusions can be drawn from the studies conducted here:

1. The beam tests have demonstrated that the deflection limit stipulated in the design provisions of the City and County of Denver (2002) is satisfied.

2. The governing failure mode of all four beams was the delamination of the upper face from the core. The beams in Tests 1, 2, and 4 failed in a very brittle manner and that in Test 3 in a ductile-like manner. The ductile-like behavior was due to premature progressive delamination caused by the poor bonding between the upper face and the core.

3. The beam tests have shown a very large scatter in the ultimate load capacities. This high variability is due to the workmanship and it underscores the importance of quality control in the manufacturing process.

4. In spite of the scatter of the results, the new shear strengthening method introduced by the manufacturer did significantly improve the load-carrying capacities of the beams.

5. Both the finite element analyses and Timoshenko beam theory agree well with the beam test results. It has been found that for the given depth-to-span ratios of the beams, shear deformation plays a significant role.

6. The nonlinear finite element analysis has shown that the shear stress at the interface between the soft core and the upper face of a beam triggers the delamination failure. The indentation of the soft core increases the interface shear stress at the edge of the loading plate. The peak shear stress near the loading plate decreases with the increase of the thickness of the upper face.

7. The initial static test on the deck model has indicated that the midspan deflection of the panel satisfies the deflection requirement in the design provisions of the City and County of Denver.

8. In the initial static test, the strain readings from the top gages of the test panel have indicated a significant strain gradient near the edge of a loading plate. Like the beam tests, this is due to the indentation of the soft core and it causes a localized increase of the interface shear stress.

9. The initial static test has indicated that the mechanical anchor that attached the GFRP panel to the concrete supports did not work very well. Some of the anchor bolts on an external support slipped when each of the two spans was subjected to a load up to 22 kips. Because of this observation, the anchor bolts have been switched to epoxy anchor for the O'Fallon Park Bridge.

10. The fatigue test has shown that Span 2 had earlier delamination (around 14,000 load cycles) than Span 1. Span 2 had delamination after 1.5 million load cycles – 15,200 cycles with a peak load of 40 kips, 355,000 cycles with a peak load of 22 kips, and 1,129,800 cycles with a peak load of 31 kips.

11. The final static test has shown that the failure of the deck panel is ductile-like. In spite of the delamination induced by the fatigue load cycles, both spans continued to carry increased loads up to about 100 kips. The ultimate failure of both spans involved progressive delamination and the fracture of the upper face near the edge of the loading plates.

12. The analytical solution based on the Kirchhoff-Love plate theory has shown that the effective bending width of an orthotropic panel is on the average 13.4% smaller than that of an isotropic panel. Furthermore, finite element analyses have indicated that the shear deformation of the soft core can further decrease the effective bending width by 13%, and that the effective bending width is also affected by the support conditions of a panel.

13. Finite element analyses have shown that the effective bending width of the test panel is 2.33 ft., which agrees very well with the experimental value of

2.38 ft. The test panel was loaded with 12x12-in. plates. Using the same model, it has been shown that the effective bending width under the wheel load of an HS 25 truck is 3.2 ft. The calculated effective width for shear stress distribution is also close to this value. Based on these results and the minimum interface shear strength estimated from the beam tests, it can be concluded that the test panel satisfied the strength requirements in the design provisions of the City and County of Denver.

14. At present, the design of this type of GFRP panels is based on the flexural criterion, whereas this study and past research have indicated that the governing failure mode is the delamination of a face from the core. The interface shear stress is the key factor that triggers the delamination failure. Hence, this should be a major consideration in design. From the fatigue endurance standpoint, it is recommended that the maximum interface shear be no more than 20% of the shear strength under service loads. In the absence of test data, this recommendation is based on the general recommendation to prevent the creep rupture or fatigue failure of GFRP materials.

REFERENCES

1. AASHTO (1998). *Standard Specifications for Highway Bridges - LRFD.* 2nd Ed., American Association of State Highway and Transportation Officials, Washington, D.C.

2. AASHTO (1996). *Standard Specifications for Highway Bridges.* 16th Ed., American Association of State Highway and Transportation Officials, Washington, D.C.

3. ASTM C393-94 (1994). *Standard Test Method for Flexural Properties of Sandwich Construction*. American Society of Testing and Materials, West Conshohocken, PA.

4. ACI 440 (2000). "Guide for the Design and Construction of Concrete Reinforced with FRP Bars." *Draft Report by ACI Committee 440,* American Concrete Institute, Farmington Hills, MI.

5. Busel, J. and Lindsay, K. (1997). "On the Road With John Busel: A Look at the World's Bridges", *CDA/Composites Design & Application,* Jan./Feb., 14-23.

6. Carol, I., Bazant, Z.P., and Prat, P.C. (1992). "Microplane Type Constitutive Models for Distributed Damage and Localized Cracking in Concrete Structures." *Proc. Fracture Mechanics of Concrete Structures,* Elsevier, 299-304.

7. Cervenka, J., Kishen, C., and Saouma, V. (1998). "Mixed Mode Fracture of Cementitious Bimaterial Interfaces, Part II: Numerical Simulation." *Engineering Fracture Mechanics,* 60(1), 95-107.

8. City and County of Denver (2002). "Federal Aid Project No. BRO-C110-015, Subaccount No. 13850, City of Denver Contract No. CE10590, O'Fallon Park Bridge over Beaver Creek." *Bid Form and Submittal Package,* Department of Public Works, City and County of Denver.

9. Daniel, I.M. and Ishai, O. (1994). *Engineering Mechanics of Composite Materials*. Oxford University Press.

10. Davalos, J.F., Qiao, P., Xu, X.F., Robinson, J., and Barth, K.E. (2001). "Modeling and Characterization of Fiber-Reinforced Plastic Honeycomb Sandwich Panels for Highway Bridge Applications." *Journal of Composite Structures*, 52, 441-452.

11. Hillerborg, A., Modeer, M., and Petersson, P. (1976). "Analysis of Crack Formation and Crack Growth in Concrete by Means of Fracture Mechanics and Finite Element." *Cement and Concrete Research*, 6(6), 773-781.

12. Lee, S.M. and Tsotsis, T.K. (2000). "Indentation Failure Behavior of Honeycomb Sandwich Panels." *Journal of Composites Science and Technology*, 60, 1147-1159.

13. Lopez, M. (2001). "Laboratory Testing of FRP Beams." *Research Report for Project C-01-49*, Clarkson University, New York.

14. *MERLIN II User's Manual* (2002). Department of Civil, Environmental and Architectural Engineering, University of Colorado, Boulder, CO.

15. *MERLIN II Theory Manual* (2002). Department of Civil, Environmental and Architectural Engineering, University of Colorado, Boulder.

16. Plunkett, J.D. (1997). "Fiber-Reinforcement Polymer Honeycomb Short Span Bridge for Rapid Installation." *IDEA Project Report*, Kansas Structural Composites, Inc.

17. Polyakov, V. (2000). "Stress Concentration in Bending of Sandwich Orthotropic Panels under Point Forces." *Journal of Composite Structures*, 48, 177-181.

18. Smith, S.A. (2001). "Vacuum Assisted Resin Transfer Molding of Foam Cored Sandwich Structures: Material Processing, Evaluation, Fracture-Toughness Testing and Analysis." *Ph.D. Thesis*, North Carolina Agricultural and Technical State University, Greensboro, North Carolina.

19. Stallings, J.M., et al. (2000). “Field Performance of FRP Bridge Repairs,” *Journal of Bridge Engineering*, ASCE, 5(2), May, 107-113.

20. Stone, D., Nanni, A., and Myers, J. (2001). “Field and Laboratory Performance of FRP Bridge Panels,” *Proceedings of Composites in Construction*, Porto, Portugal, 701-706.

21. Szilard, R. (1974). *Theory and Analysis of Plates - Classical and Numerical Methods*. Prentice Hall.

22. Thomsen, O.T. and Frostig, Y. (1997). “Localized Bending Effects in Sandwich Panels: Photoelastic Investigation Versus High-Order Sandwich Theory Results.” *Journal of Composite Structures*, 37, 97-108.

23. Timoshenko, S.P. and Woinowsky-Krieger, S. (1959). *Theory of Plates and Shells*. 2nd Ed., McGraw-Hill.